<u>İSTANBUL TECHNICAL UNIVERSITY ★ INSTITUTE OF SCIENCE AND TECHNOLOGY</u>

GROUND MOTION AROUND ISTANBUL, TURKEY MEASURED BY SATELLITE RADAR INTERFEROMETRY

Ph.D. Thesis by

Samuray ELİTAŞ AKARVARDAR, M.Sc.

Department : Geodesy and Photogrammetry Engineering

Programme: Geodesy and Photogrammetry

NOVEMBER 2007

İSTANBUL TECHNICAL UNIVERSITY ★ INSTITUTE OF SCIENCE AND TECHNOLOGY

GROUND MOTION AROUND ISTANBUL, TURKEY MEASURED BY SATELLITE RADAR INTERFEROMETRY

Ph.D. Thesis by

Samuray ELİTAŞ AKARVARDAR, M.Sc.

Date of submission : 19 September 2007
Date of defense examination : 23 November 2007

Supervisor (Chairman) :	**Prof. Dr. Cankut ÖRMECİ**
Co-Supervisor :	**Prof. Dr. Kurt FEIGL (UW-Madison, USA)**
Members of the Examining Committee	**Prof. Dr. Muhammed ŞAHİN (İTÜ)**
	Prof. Dr. Nebiye MUSAOĞLU (İTÜ)
	Prof. Dr. Okan TÜYSÜZ (İTÜ)
	Prof. Dr. Christophe DELACOURT (UBO, FR)
	Dr. Wayne THATCHER (USGS, USA)
	Assoc. Prof. Dr. Cengizhan İPBÜKER (İTÜ)
	Prof. Dr. Michel RABINOWICZ (OMP, FR)

NOVEMBER 2007

<u>**İSTANBUL TEKNİK ÜNİVERSİTESİ ★ FEN BİLİMLERİ ENSTİTÜSÜ**</u>

İSTANBUL CİVARINDA YER HAREKETİNİN UYDU RADAR İNTERFEROMETRİSİYLE ÖLÇÜLMESİ

DOKTORA TEZİ

Y. Müh. Samuray ELİTAŞ AKARVARDAR
501972602

Tezin Enstitüye Verildiği Tarih : 19 Eylül 2007
Tezin Savunulduğu Tarih : 23 Kasım 2007

Tez Danışmanı : **Prof. Dr. Cankut ÖRMECİ**

Ek Tez Danışmanı : **Prof. Dr. Kurt FEIGL (UW-Madison, ABD)**

Diğer Jüri Üyeleri **Prof. Dr. Muhammed ŞAHİN (İTÜ)**

Prof. Dr. Nebiye MUSAOĞLU (İTÜ)

Prof. Dr. Okan TÜYSÜZ (İTÜ)

Prof. Dr. Christophe DELACOURT (UBO, FR)

Dr. Wayne THATCHER (USGS, ABD)

Doç. Dr. Cengizhan İPBÜKER (İTÜ)

Prof. Dr. Michel RABINOWICZ (OMP, FR)

KASIM 2007

PREFACE

This study has been supported by grants from the European Union (FORESIGHT 511139) and the French government “Agence National de Recherche” (HYDRO-SEISMO) since March 2005. All SAR data were provided by the European Space Agency, which holds the copyright to them under the terms and conditions of a Category-I project (number 3245). Most of the work has been carried out at the DTP (“Dynamique Terrestre et Planétaire”) laboratory of OMP (Observatoire Midi-Pyrénées) in France and partly, at the Geology and Geophysical Institute of University of Wisconsin-Madison in USA. I would like to thank Dr. Kurt Feigl from University of Wisconsin-Madison for supervising me and providing all these facilities. I am also thankful to Prof. Dr. Cankut Örmeci from İstanbul Technical University who made me enjoy remote sensing and to Assoc. Prof. Dr. Semih Ergintav from TÜBİTAK MRC who encouraged me to study earth sciences. Next, I wish to thank the complete thesis defense committee, respectively, Prof. Okan Tüysüz, Prof. Dr. Nebiye Musaoğlu, Dr. Wayne Thatcher, Prof. Dr. Michel Rabinowicz, Prof. Dr. Christophe Delacourt, Prof. Dr. Muhammed Şahin, and Assoc. Prof. Cengizhan İpbüker. Their insights helped me improve the discussion part of Chapter 3.

Alexis Rigo, the director of DTP laboratory, Anne-Marie Cousin, Nathalie Dalla-Riva, Pierre Pastor, Loic Jahan, Michel Rabinowicz, David Baratoux, Marie Calvet, Annie Souriau and my office mates Audrey Tocheport and Carmen Castaneda are greatly acknowledged for their help and hospitability which allowed me to work comfortably during my stay at OMP.

Finally, I cannot forget my husband, Kerem Akarvardar who was also a PhD student during the course of this study. I wish to thank him for being my model with his hard work, concentration, and dedication. My thanks are also due to Elitaş and Akarvardar families who provided endless support.

Samuray ELİTAŞ AKARVARDAR

CONTENTS

GLOSSARY

1-GP	: Mono-Gyro Mode
AMI	: Active Microwave Instrument
ASAR	: Advanced Synthetic Aperture Radar
BPT	: Becker Penetration Test
CNES	: French Space Agency
CPT	: Cone Penetration Test
DEM	: Digital Elevation Model
DIAPASON	: Differential Interferometric Automated Process Applied to Survey of Nature
DTOOLS	: DIAPASON tools
EBM	: Extra Back-up Mode
ENVISAT	: Earth Observation Environmental Satellite
ERS	: Earth Resources Satellite
ESA	: European Space Agency
GIPhT	: General Inversion for Phase Technique
GPS	: Global Positioning System
InSAR	: SAR interferometry
LOS	: Line of sight
NAF	: The North Anatolian Fault
PS	: Persistent Scatterer
RADAR	: Radio Detection and Ranging
SAR	: Synthetic Aperture Radar
SLC	: Single Look Complex
SNR	: Signal to Noise Ratio
SPT	: Standard Penetration Test
YCM	: Yaw Control Mode
YCM-R	: Yaw Control Mode Regional Operations
ZGM	: Zero Gyro Mode
SPT	: Standard Penetration Test

LIST OF TABLES

LIST OF FIGURES

LIST OF SYMBOLS

a_{ij}^{k}	: Calibrated amplitude value of the pixel ij in the kth scene
A_{ij}^{k}	: Amplitude value of the pixel ij in the kth scene
A	: Design matrix
A_1, A_2	: Amplitudes of two epochs
b	: Vector of observations
B	: Orbital separation (baseline)
B_c	: Critical orbital baseline
B_R	: Range bandwidth
$B_{\parallel}$	: Parallel component of orbital separation
$B_{\perp}$	: Perpendicular component of orbital separation
C	: Cost Function
d	: Scalar displacement
D_A	: Amplitude dispersion
E	: Vector of residuals
f_0	: Carrie frequency
g	:Complex reflectivity
h_a	: Altitude of ambiguity
h_{sat}	: Height of satellite
h_P, $h_{P'}$	: Height of point P and P'
i	: Interferogram number
k	: Pixel number
m_A	: Mean of amplitudes
n	: Phase ambiguity
n_n	: Complex noise
N	: Number of interferograms
n_R, n_I	: Real and imaginary components of noise
r_0	: Proximal distance (near range)
P, P'	: Points on the ground
R	: Range
R_1, R_2	: Range of first and second epoch
R_{slave}	: Range from slave orbit
Δr	: Shift in the near range
s	: Scattering amplitude
$\hat{s}$	: Unit vector pointing from ground to the satellite
s_1, s_2	: Two complex pixels
t_0	: The start time of the radar acquisition
t	: Time
t_1, t_2	: The first and the second epoch
t_i, t_j	: ith master and slave epoch
Δt_{12}	: Time difference between two epochs
Δt	: Shift in the start time of the radar acquisition
$\vec{u}$	: Displacement field

$\mathbf{u_e}$	: Easting component of the displacement vector
$\mathbf{u_n}$	: Northing component of the displacement vector
$\mathbf{u_u}$	: Up component of the displacement vector
$\mathbf{x}$	: Vector of unknown parameters
$\mathbf{x_u}$	: Position
$\mathbf{x, y}$	: Pixel position
$\mathbf{X^k}$	: Mean of the k^{th} amplitude image
$\mathbf{X_{stack}}$	: Mean of the amplitude stack
$\mathbf{V}$	: Covariance matrix
$\Delta\mathbf{V}$	: Volume change
σ_A	: Standard deviation of amplitude
σ_n	: Standard deviation of noise
σ_v	: Standard deviation of phase
Φ_1, Φ_2	: Absolute phase at the first and the second epoch
$\Delta\Phi_{12}$ or Φ	: Absolute phase difference between the first and the second epoch
Φ_1, Φ_2	: Phase measurement at the first and second epoch
Φ_{12} or Φ	: Interferometric phase (wrapped)
Φ_o	: Constant phase offset
Φ_{pix}	: Pixel contribution to interferometric phase
Φ_{topo}	: Topographic contribution to interferometric phase
Φ_{atm}	: Atmospheric contribution to interferometric phase
Φ_{orb}	: Orbital contribution to the interferometric phase
Φ_{disp}	: Phase Contribution due to displacement
Φ_d	: Displacement in line of sight of the satellite
η	: Local incidence angle
θ	: Radar look angle
θ_{master}	: Look angle for the master image
α	: Local slope
α_B	: Orientation of $B_\perp$ from horizontal plane
α_h	: Azimuth of the satellite heading
γ	: Coherence
γ_R and γ_I	: Real and imaginary components of coherence

SUMMARY

This thesis seeks to monitor surface deformation in an urban environment using satellite radar interferometry. The questions addressed in this thesis come from the convergence of three recent events: (a) The 1999 İzmit Earthquake that increased the probability of a future earthquake near Istanbul metropolitan city as well as the effort required to manage the associated risk, (b) new technical developments in interferometric synthetic aperture radar (InSAR) that permit a quantitative analysis of the 15-year-long ERS data set as a time series rather than a set of image, and (c) a ground motion map based on InSAR techniques prepared by Terrafirma, an initiative coordinated by the European Space Agency.

The main research objectives of the thesis are to: (a) master new techniques in mapping deformation by InSAR, (b) establish a strategy for measuring slow and long-term surface deformation, (c) measure ground motion in İstanbul metropolitan area, (d) describe physical models of ground motion, and (e) evaluate the contribution of displacement maps to managing seismic risk.

Avcilar county of Istanbul is selected for long-term ground deformation analysis. Avcilar town was severely affected from the 1999 Izmit Earthquake although the town was located 125 km away from the epicenter of the earthquake. The situation has increased the vulnerability of the town in a future earthquake, compounding the concern about landslides, that have been occurring for many years. Terrafirma showed the deformation in the vicinity as ground motion with a constant rate of more than 5 mm/yr.

In this thesis, radar images acquired by the ERS-1 and ERS-2 satellites between 1992 and 2002 are analyzed. Raw SAR data is processed using the PRISME/DIAPASON software developed at the French space agency (CNES) based on the standard procedure for two-pass interferometry. The General Inversion for Phase Technique (GIPhT) developed by Feigl and Thurber is used to model a set of 24 interferometric pairs of radar images (interferograms). Interferograms are reduced to a reliable subset of phase observations using the techniques since 2000.

Analysis of 14 synthetic aperture radar images acquired by the ERS-1 and ERS-2 satellites between 1992 and 1999 by interferometry (INSAR) reveals downward displacement around the Avcılar area of İstanbul. Using the General Inversion for Phase Technique, (GIPhT), we analyze a set of 24 interferometric pairs. The interferometric fringe patterns show a crescent shape. We interpret them as purely vertical displacement at a secular rate. The maximum displacement rate of 7 mm/yr occurs at a point located at latitude 40.98ºN and longitude 28.71ºE. A simple 4-parameter elastic Mogi model consisting of three infinitesimal spherical sinks at a depth of 2300 ± 1300 m deflating at 78 ± 34 thousand cubic meters per year describes ground motion signal to first order. The model also accounts for tropospheric effects by estimating one vertical phase gradient for each image acquisition epoch. The model fits the data with a cost of 0.21 cycles per datum for the 9288 phase measurements included in the inversion. For the complete data set, including 29,241 unmasked pixels in the 24 pairs, the cost is 0.19 cycles per datum. Both these fits are significantly better than the null hypothesis and the prior model with 95% confidence for 18 free parameters.

The spatial distribution of the negative displacement rates suggests that most of the ground motion occurs on the slopes (of Harami stream valley). Çukurçeşme ve Gürpınar sediments on these slopes are porous, permeable, partially saturated are susceptible to landslides. So, it seems likely that the ground motion around Avcılar interpreted as purely vertical and appearing as subsidence is related to the landslides. Accordingly, steady downward ground motion suggests that the material once displaced on the slopes after a series of landslides during the wet season have been gradually sliding and settling down. The slopes with high displacement rates might be susceptible soil liquefaction during an earthquake as well.

ÖZET

Bu tez, kentsel bir ortamda oluşan yüzeysel haraketin uydu radar interferometrisiyle izlenmesi konusunda bir araştırmadır. Bu tezin gerçekleştirilmesinde, yakın zamanda olan üç olay etkili olmuştur:

a) 1999 İzmit Depremi. Bu deprem, İstanbul metropolü yakınında deprem olasılığını artırmıştır. Dolayısıyla, deprem risk yönetimi konusundaki çalışmalar önem kazanmıştır.

b) Yapay açıklıklı radar interferometrisinde (InSAR) olan yeni gelişmeler. Bu gelişmeler, 15 yıllık ERS uydu görüntü arşivini, bir veri kümesi olarak değil bir zaman serisi olarak analiz etmemize olanak sağlamıştır.

c) Avrupa Uzay Ajansi ESA tarafından koordine edilen Terrafirma girişiminin, Avrupa'nın çeşitli metropolleri ve İstanbul için hazırladığı çökme haritaları.

Bu tezde; a) INSAR'la yüzey deformasyonun haritalanması konusunda önerilen güncel tekniklerde uzmanlaşmak; b) yavaş ve uzun zamanda oluşan yüzey hareketinin belirlenmesi için bir yaklaşımın geliştirilmesi; c) İstanbul metropolu çevresinde yerdeğiştime miktarının belirlenmesi; ve d) yerdeğiştime haritalarının afet yönetimi çerçevesinde ele alınması hedeflenmiştir.

Uzun süreli deformasyonun belirlenmesi çalışmaları için İstanbul'un Avcılar ilçesi seçilmiştir. Avcılar, 1999 İzmit depremi merkez üssünden 125 km uzakta olmasına rağmen, depremden çok ağır bir şekilde etkilenmiştir. Bölgede yıllardır var olan toprak kaymaları da göz önüne alındığında; 1999 İzmit Depreminin, Avcılar'in "zarar görebilirliğini" ("vulnerability") artırdığı düşünülmektedir. Terrafirma ise bölgenin, yılda 5 mm'den fazla sabit bir hızla çöktüğünü göstermiştir.

Bu tezde, ERS-1 ve ERS-2 uydularından 1992 ve 2002 yılları arasında elde edilen radar görüntüleri analiz edilmiştir. Ham SAR verileri, Fransa Uzay Ajansı (CNES) tarafından geliştirilen, standard iki-geçişli interferometri presibine dayanan PRIME/DIAPASON yazılımıyla işlenmiştir. Radar görüntü çiftleri, Feigl and Thurber tarafından 2007'de geliştirilen "Faz Tekniği İçin Genel Dönüşüm" ("General Inversion for Phase Technique" (GIPhT)) yaklaşımı kullanılarak modellenmiştir. Interferogramlardaki (iki radar görüntüsünün faz farkından oluşan görüntü) veri yoğunluğu, 2000'lerin başından beri geliştirilen yöntemlerle azaltılmıştır.

ERS-1 ve ERS-2 uyduları tarafından 1992 ve 1999 yılları arasında elde edilen 14 SAR görüntüsü, Avcılar çevresinde negatif yönde dikey yerdeğiştirme göstermiştir. GIPhT teknigi kullanılarak 24 interferometrik görüntü çifti analiz edilmiştir. Ortalama interferometrik faz döngüsünün ("phase cycle" ya da "fringe") dağılımı, belirli bir bölgenin radar yönü doğrultusundan sabit bir hızla uzaklaştığını göstermektedir. Haraketin salt dikeyde olduğu varsayılırsa, maksimum hızı, 40.98° enlemi 28.71° boylamında 7 mm/yıl olmaktadır. Yerdeğiştirmelerin modellenmesinde, 4-parametrelik elastik basit bir Mogi modeli kullanılmıstır. Dikey değişme sinyali, 2300 ± 1300 m derinde yılda 78 ± 34 bin m^3 ile sönen üç ayrı küresel Mogi kaynağı ile birinci dereceden tanımlanmıştır. Bu model ayrıca; troposferin her görüntü tarihinde faz ölçmelerini topoğrafik yüksekliğe bağlı olarak etkilediğini göz önüne almıştır. Modelin veriye yakınlığını ölçmek için maliyet analizi ("cost analysis") yapılmıştır. Modelin veriye yakınlığı, 9288 faz ölçmesi için ölçü başına 0.21 faz döngüsüdür ("pixel/cycles"). 24 interferogramdaki 29,241 faz ölçmesini kapsayan veri kümesinin maliyeti ise ölçü başına 0.19 faz döngüsüdür. Model ve veri arasındaki bu iki yakınlık değerlendirmesi, 18 serbest parametre için %95 güvenirlilik sınırları icinde kalmıştır.

Yerdeğiştirmelerin uzaysal dağılımı, hareketin büyük bir kısmının eğimli topraklarda (özellikle, Harami Deresi yamaçlarında) olduğunu göstermektedir. Kısmen doygun ve gözenekli Çukurçeşme ve Gürpınar formasyonundan oluşan bu topraklarda çok uzun zamadır toprak kaymaları gözlenmektedir. Bu bağlamda, yamaçlarda sabit hızda "çökme" şeklinde ortaya çıkan toprak haraketlerinin, yağışlı mevsimde süreksiz bir şekilde oluşan toprak kaymalarının bir devamı olduğu, bu bölgelerde toprağın bütün sene boyunca kaymaya ve oturmaya devam ettiği sonucuna varılmaktadır. Yüksek yerdeğiştirmelerin ölçüldüğü bu yamaçların, büyük bir depremden sonra sıvılaşmaya da dayanıksız olabileceği sonucu ortaya çıkmaktadır.

1. INTRODUCTION

Radar interferometry has become more than a new alternative method for measuring ground deformation since its first demonstration by Gabriel (1989) and validation for geophysical applications by Massonnet et al. (1993). Ferretti et al. (2000) proposed a relatively new technique that addressed the decorrelation and atmospheric problems of conventional radar interferometry. The new technique uses “point target scatterers” to measure long term ground deformation.

The main objective of this thesis is to measure slow, long-term ground motion in one of the counties of İstanbul city by using point target analysis in radar interferometry. Since the radar interferometry is sensitive to measure vertical ground motion, the technique is very efficient to measure “land subsidence” phenomenon. If interferometric measurements around İstanbul city indicate “land subsidence”, the current subsidence map can be used to anticipate areas susceptible to “soil liquefaction” during an earthquake. In İstanbul metropolis, this is a very important issue since the 1999 Izmit Earthquake shifted the seismic gap on North Anatolian Fault towards the city.

This introductory chapter gives a brief description of “land subsidence” and “soil liquefaction”. Tectonic setting around İstanbul metropolis is summarized to emphasize the earthquake hazard risk in the region. This chapter also contains an introduction to radar interferometry and a list of important land subsidence studies using radar interferometry.

1.1. Land subsidence

The term “land subsidence”, in a broad sense, includes both gentle downwarping (or sinking) and the collapse of discrete segments of ground surface (Allen, 1984). It is actually a surficial symptom that results from a variety of subsurface mechanisms. The displacement field involves mostly vertical downward movement of the land surface, although associated small horizontal movements may also be present. The term does not include landslides which have large horizontal displacements. Subsidence processes may take a long time to reach the Earth’s surface. Furthermore, the source driving the subsidence may not lie directly below it.

Extent of the subsided area may vary depending on the cause of the subsidence. On a small scale, tree roots can suck water from soil during a dry summer and cause the corner of a house to subside (Waltham, 2002). On a larger scale, extraction of groundwater can cause a whole city to subside, as in Houston–Galveston, Texas where the total of the subsiding area reaches 12 000 km^2 (Gabrysch, 1984). Subsidence also varies in time. The famous Pisa Tower leans more than 5 m to one side as a result of having subsided at a vertical rate of 1.5 mm/yr for more than 800 years (Burland et al., 2002). On the other hand, 1999 Izmit Earthquake (M= 7.4) lasted only 37 s but caused hundreds of buildings in Adapazari to subside as much as 1.5 m (e.g., USGS, 2000).

Land subsidence can be caused by natural or anthropogenic sources. The consequences of anthropogenic subsidence from fluid extraction can be dramatic and hazardous. Today, tens of metropolitan areas face severe socio-economical and environmental damage caused by fluid extraction, for example; Venice (Italy), New Orleans (USA) and Mexico City (Mexico) suffer from groundwater extraction; Los Angeles (USA) from oil withdrawal and Groningen (The Netherlands) from gas extraction.

Allen (1984) distinguishes six basic causes of land subsidence:

(1) Dissolution evaporates and carbonates reduce rock volume. The development of subsidence depends on their solubility and mechanical properties. The carbonate rocks, limestone and dolomite are widespread and thus cause many cases of subsidence. The incidence of collapse and sinkhole development overlying the carbonate rocks may be greatly increased by engineering activities that alter the ground water levels.

(2) When moving water gains an access to rock or soil, it erodes the material and transports it as grains of silt and sand. As water creates and enlarges tunnels by its flow, it reduces the substrate's ability to support surface loads. Consequently, the ground surface collapses to produce the sinkholes typical of karstic terrains. This phenomenon is called "mechanical erosion" by Allen (1984).

(3) Common earth materials susceptible to plastic flow, such as salt gypsum, clay and clay shale, may undergo a lateral flow under natural geological conditions and/or under anthropogenic loading.

(4) A common cause of ground-surface subsidence is a reduction in the volume of low-density sedimentary deposits that accompanies the process of compaction, in which particles become more closely packed and the amount of pore space is

reduced (Allen, 1984). Compaction occurs by both natural and anthropogenic processes.

(5) Subsidence caused by extraction of solids manifests itself as gradual sagging or downwarping of the overburden into mine cavities (Carbognin, 2003). The time needed for sinkholes and cracks to reach the surface appear to be random. Consequently, very few observations of this kind of process have been recorded.

(6) Deformation associated with active volcanoes and earthquake generating faults are classified as tectonic subsidence.

For some sites more than one of the causes may produce subsidence. In addition, anthropogenic activities may accelerate natural subsidence processes, for example drilling an oil well into a salt dome (Aryal et al., 2004). Compaction (4) will be discussed in detail in the next section.

1.1.1. Compaction as a cause of subsidence

Poland (1984) defines "compaction" as the decrease in the thickness of sediments, as a result of an increase in vertical compressive stress. The term compaction is applied both to the process and to the measured change in thickness. Allen (1984) distinguishes several processes that can cause compaction:

(a) In its natural equilibrium state, underground fluids support some of the weight of the overlying sediments. When fluids are depressurized or removed, where the materials are very compressible and pore pressures can be high, compaction may occur. Most noticeable compaction incidents are caused by anthropogenic fluid withdrawal. This includes the extraction of (1) oil, gas, and associated water, (2) hot water or steam for geothermal power, and (3) ground water (Poland, 1984). All these types of extraction processes produce subsidence signals of the same order of magnitude and their consequences on the environment can be observed using same techniques.

When water is extracted from unconsolidated sediments, they compact like a sponge. An aquifer system is a heterogeneous body of interbedded aquifers and aquitards that control the flow of groundwater movements. Aquifers consist of extensive layers of saturated permeable material such as unconsolidated alluvial deposits of sand, gravel or porous sandstones. On the other hand, aquitards consist of relatively impermeable layers such as silt and clay, that impede ground-water movement. Depending on the storage and compressibility characteristics of the groundwater reservoir, compaction may be permanent (inelastic) or recoverable (elastic). In the latter case, compaction is followed by expansion of the subsurface deposits and the subsidence is followed by uplift of the land surface.

Today, land subsidence caused by fluid extraction (especially groundwater) is a global problem. Permanent subsidence and related ground failures are of environmental and socio-economical concern. Gambolati et al. (2005) suggest that to be major concern, subsurface fluid withdrawal should satisfy two criteria. First, the subsidence should occur in a densely populated and highly developed areas located close to the sea or a lagoon or a delta. Second, it should occur in unconsolidated geological basins of alluvial, lacustrine or shallow marine origin, formed typically during the Quaternary period.

(b) Mechanical loading of the ground by the weight of man-made structures can also cause subsidence. Natural loading is also possible, for example by glaciers.

(c) In low-elevation areas, lowering of the water table by artificial drainage networks stimulates the compaction of sediments accompanying subsidence of surface.

(d) Vibration such as continuous truck traffic, underground excavations (e.g., for tunnel construction), pile driving and blasting may cause settlement of the unconsolidated material underlying the buildings. Earthquakes can also contribute to compaction by shaking during the passage of seismic waves. Although the vibrations last only a few minutes, the subsequent compaction and subsidence can continue for longer times. Accordingly, this type of subsidence can be difficult to distinguish from permanent co-seismic subsidence caused by earthquakes.

(e) Certain materials in areas of low rain fall undergo significant compaction after they become wetted. The process, termed hydro-compaction produces rapid and irregular subsidence of the ground surface.

1.1.2. Measuring and monitoring land subsidence

We can observe the temporal and the spatial pattern of land subsidence by measuring the displacement as a function of space and time. These quantities are called the displacement field, and denoted mathematically as $u(x_u,t)$ where x_u is position and t is time. Further hydro-geological and soil analysis allow us to understand the complexity and the interaction of the subsidence mechanisms in the sub-surface. Specifically, monitoring land subsidence contributes to

- evaluate the present damage to the urban environment (e.g., private buildings, historical sites, lifelines, engineering structures, factories),
- land-use management and urban planning,

- assess the effects on environmental degradation,
- manage the water resources (e.g., monitoring the withdrawal and recharge of ground water),
- determine its role in future hazardous activities (e.g., floods, earthquakes),
- understand the nature of tectonic processes (e.g., earthquake mechanism, volcanic activity),

For measuring vertical displacements on the ground surface, there have been two traditional methods: ground-based spirit leveling and Global Positioning System (GPS) surveying. The accuracy of spirit leveling can be quite good (~10 mm over 100 km) despite its simplicity. The GPS networks can operate in two modes (Feigl, 2003). The continuous operation of permanently installed, widely spaced antennas (CGPS) provide good temporal resolution (1 measurement/30 s) but poor spatial resolution (>100 km between stations). The continuous mode is convenient for measuring tectonic deformation because other types of land subsidence, especially the anthropogenic types, occur in relatively small areas. Alternatively, GPS surveys can operate in “campaign” mode with intermittent occupation. This mode offers good spatial resolution (5-10 km between stations) by sacrificing temporal resolution (~1/yr). A compromise “hybrid” strategy (Feigl, 2003) may be a more appropriate for monitoring time dependent subsidence e.g., seasonal cycles related to heavy water withdrawal for agricultural practices during summer months. In practice, however, the cost of moving the GPS instruments has pushed most networks to the continuous mode of surveying.

The accuracy of the ground-based methods depends on a proper network design of benchmarks and survey planning. Under optimum conditions, a subsidence rate accuracy of < 5 mm/yr should be attainable (Gambolati, 2005). Furthermore, a stable benchmark located outside the subsiding area should be used as a reference.

In-situ measurements are necessary to monitor the withdrawal and recharge balance in underground reservoirs. For large volumes of ground water withdrawal, borehole extensometers and for gas/oil reservoirs, radioactive tracers can be injected to measure compaction and expansion. Borehole extensometers are often coupled to piezometers which record the hydraulic head variations.

Radar interferometry has become more than a alternative method for measuring ground deformation since its first demonstration by Gabriel (1989) and validation for geophysical applications by Massonnet et al. (1993). Many land subsidence studies have been carried out; Table 1.1 gives a list of major anthropogenic land subsidence events studied using radar Interferometry.

Table 1.1 : Some of the major anthropogenic subsidence events studied by radar interferometry.

Groundwater Change	
Mojave Desert, CA (USA)	Galloway et al., 1998
Las Vegas, NV (USA)	Amelung et al., 1999
Los Angeles, CA (USA)	Bawden et al., 2001
Las Vegas Valley, Nevada (USA)	Hoffmann et al., 2001
Santa Clara Valley, CA. (USA)	Schmidt et al., 2003
Oil/Gas Extraction	
The Lost Hills, Belridge, CA (USA)	Fielding et al., 1998
Los Angeles Basin, CA (USA)	Colesanti et al., 2003
Ouargla, Sahara Desert (Algeria)	Aryal et al., 2004
Geothermal Fields	
East Mesa, CA. (USA)	Massonnet et al., 1997
Vatnajökull (Iceland)	Jonsson et al., 1998
Cerro Prieto, Baja California (Mexico)	Carnec & Fabriol, 1999
Coso, CA. (USA)	Fialko & Simons, 2000
Solid Extraction	
Gardenne, (France)	Carnec et al., 1996.
Ruhrgebiet (Germany)	Wegmuller et al., 2000

1.1.3. Radar interferometry

As a geodetic technique, interferometry calculates the interference pattern caused by the difference in phase radar images data acquired at distinct times. The resulting interferogram is a contour map of the change in distance between the ground and the radar instrument. These maps provide an unsurpassed spatial sampling density (~100 pixels/km^2), a competitive precision (~10 mm) and a useful observation cadence (1 pass/month) (Feigl, 2003). Furthermore, inaccessible parts of the earth that cannot be observed by any other technique can be observed by radar interferometry since the technique requires no equipment on the ground.

Irregularities in the satellite orbits, atmospheric disturbances and temporal decorrelation are the major limiting factors in radar interferometry. Although the problem of orbits and atmosphere can be overcome by using alternative data pairs, the revisit time of the satellite (typically 1 pass/month) may still be a limiting factor. Temporal decorrelation can severely affect the applicability of radar Interferometry. On the other hand, the technique is able to measure only 1-D scalar displacement along the radar line of sight. It requires intensive data processing.

The phenomenon of temporal decorrelation occurs when the scattering characteristics of the ground surface changes between the two radar acquisitions. In the beginning of 2000's a new approach to interferometry, called "permanent scatterers" (Ferretti et al., 2000), emerged to overcome the temporal decorrelation problem. Since then, the technique has been widely applied. The same technique is sometimes referred to as "persistent scatterers" (PS) (e.g., Hooper, 2006). The PS technique performs interferometry on those individual scatterers that are identified as coherent over time.

Radar interferometry, recently together with the PS technique, has been proved to be the most efficient technique to measure anthropogenic land subsidence in urban areas. There are several reasons for its efficiency:

- The technique works well in urban areas because of the strong corner reflector effect of man-made structures.

- The technique is applicable only if a "synthetic aperture radar" (SAR) data set includes more than 30 epochs. The Earth Resources Satellite (ERS) SAR archive spanning 15 years has been opened to scientific use by European Space Agency (ESA).

- The steep looking of ERS satellite ($\theta \approx 23^o$) is more appropriate to measure vertical motions. For the descending ERS orbit, the vertical component of a displacement vector Φ_d along the line of sight of the radar is 0.92 ($\cos 23^o$) (see section 2.2.4.5 for more details). With this model, the ground motion is assumed to be pure vertical. In this case, negative vertical displacements indicate subsidence.

- Subsidence data obtained by in-stu and ground monitoring techniques tend to be available for anthropogenic subsidence. Natural (unmonitored) subsidence is not as easily quantified.

1.2 Tectonic Setting Around Istanbul Metropolitan Area

The highly populated and industrialized metropolitan area of Istanbul is situated in the North Anatolian Fault (NAF) Zone. The North Marmara Sea fault segment lies 15 km away from the Prince Islands and continues westward parallel to Istanbul coast (including Bakırköy, Zeytinburnu and Avcılar) (Figure 1.1).

As a result of the northward motion of the Arabian Plate, the Anatolian block slips westward with respect to the Eurasian Plate. The boundary between the Anatolian block and the Eurasian plate forms the North Anatolian Fault Zone. The 1600 km long North Anatolian Fault extends from Karliova triple junction to the Gulf of Saros and continues beneath the North Agean Sea as far as mainland Greece. The NAF, as a seismically active right-lateral strike-slip fault, has been the focus of numerous studies since 1950's.

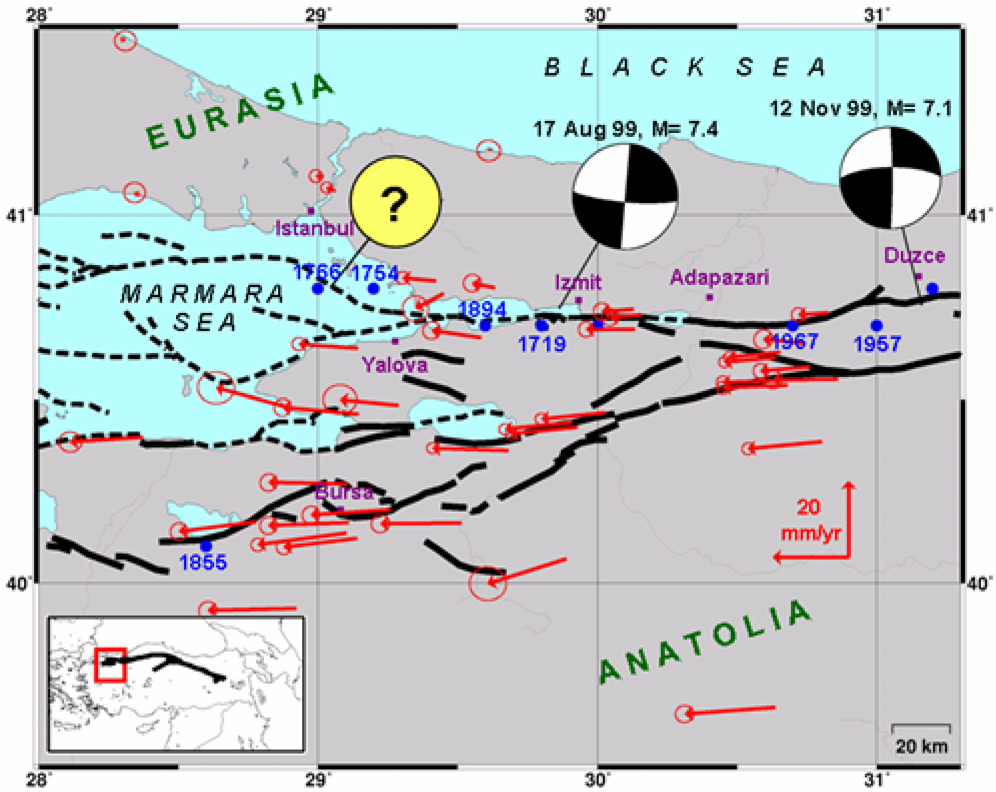

Figure 1.1 : Tectonic setting around İstanbul metropolitan area. The map shows the recent large damaging earthquakes (in blue numbers) (from Ambraseys, 2002), fault plane solutions of the 1999 earthquakes (from Bogazici University KOERI), GPS velocity vectors (in red) in mm/yr (from Reilinger et al., 2006), the probable location of the future earthquke (in yellow circle) (e.g., Parsons et al. 2000), the faults along the NAF zone (black lines) (from Barka & Kadinsky-Cade, 1988) and the uncertain faults in the Marmara Sea (black dashed lines).

Estimations on the age and the total fault offset of the North Anatolian Fault differ in geological observations. Barka & Kadinsky-Cade, 1988, Barka, 1992 and Hubert-Ferrari et al., 2002, agree that the age of the NAF is 13 Myr and the total offset of the fault varies from 30 to about 100 km. The long term slip rate along the fault also varies in geological observations and seismological data. Global Positioning System (GPS) measurements present more consistent estimate of the present-day slip rates (Reilinger et al., 1997, McClusky et al., 2000, Reilinger et al., 2006). The most recent estimate of the slip rate of the North Anatolian Fault is 24 ±1 mm/yr (Reilinger et al., 2006). This slip rate, based on the GPS measurements during the interval between 1988 and 2005, assumes a single constant slip rate for the Anatolian block relative to the Eurasia plate all along the North Anatolian Fault.

In the Marmara Sea Region, west of Longitude 31°, the North Anatolian Fault divides into three strands: the southern, the middle and the northern (Barka & Kadinsky-Cade, 1988). Each has a different earthquake history (e.g., Ambrassey 2002). The southern strand produced some large earthquakes in the 19th century. The middle strand is not known to have experienced any large earthquakes for 200 years. Most of the northern strand lies beneath the Marmara Sea. Besides the catastrophic 1999 İzmit and Düzce earthquakes, the northern strand has experienced six large damaging earthquakes (in 1912, 1935, 1963, 1943, 1957 and 1967) since the beginning of the 20th.

The August 17, 1999 Izmit and the November 12, 1999 Düzce earthquakes were the seventh and the eighth in a sequence of large earthquakes ($M_w > 7$) (e.g., Barka 1999, Parsons et al., 2000, Hubert-Ferrari et al., 2000, Barka, et al., 2002, Akyüz et al., 2002) migrating westward along the North Anatolian Fault starting from the 1939 Erzincan Earthquake (e.g., Barka, 1996, Armijo et al., 1999). Actually, the part of the North Anatolian Fault Zone where the 1999 earthquakes occurred had already been identified as seismic gap by Toksoz et al., (1979). Two studies pointed out that previous earthquakes had increased Coulomb failure stress on the NAF around Izmit. (e.g., Stein et al., 1997, Nalbant et al., 1998). Consequently, the earthquake sequence between 1939 and 1999 has caused a 1000 km rupture from Erzincan (Longitude ~40°) to an offshore location of 10-15 km western of Hersek Delta (Longitude ~29.3°). The time interval between these westward migrating earthquakes varied from 3 months to 32 years.

The 17 August 1999 Izmit Earthquake has been one of the most documented earthquakes. The magnitude 7.4 earthquake was located at the east of Izmit Bay at a depth of around 17 km (e.g., Barka, 1999). Besides the city of Izmit; Yalova, Bolu, Adapazari, Bursa, Eskişehir, Düzce were also severely affected by the shaking that lasted 45 seconds. The earthquake caused at least 15,000 deaths, 23,000 injuries and collapse or damage of about 86,000 buildings (SPO, 1999). The earthquake caused considerable damage even in İstanbul, in the district of Avcılar, in the western part of the city, approximately 70 km away from the epicenter.

The earthquake surface rupture has been observed at the field by various research groups (e.g., Barka et al., 2002, MTA, 2003). At the west end, the rupture zone propagated towards Hersek after a stepover close to the earthquake hypocenter and then continued offshore towards the north of Yalova. At the east end, the rupture extended to the south of Eften Lake. Most research groups suggest that the surface rupture had a total length of 110-125 km and might have exceeded as much as 130-150 km with another segment under the water. The earthquake was almost pure right-lateral E-W strike-slip and the fault plane was nearly vertical in most places. The rupture zone consisted of four segments onshore and one segment offshore. The maximum slip throughout the surface break was observed on the east of Sapanca and at the town of Gölcük where the fault offset reached 5.2 m (Barka et al., 2002). Along the normal faults, which connect the strike slip segments in the pull-apart areas, there was a maximum vertical offset of 2.4 m (Barka et al., 2002).

Besides the field studies of the earthquake surface rupture, many other studies have been carried out including space geodesy techniques, InSAR and GPS, (e.g., Reilinger et al., 2000, Wright, 2000, Çakır et al., 2001, Feigl et al., 2002). The multiple-fault solutions from InSAR find a smoothly varying slip distribution, with around 1.7 m of slip on the segment west of Hersek, increasing sharply to nearly 5 m north of Gölcük, and tailing off to the east (Wright, 2000). These solutions also suggest that the fault ruptured the whole seismogenic layer to a depth of 20-22 km (Wright, 2000). Also, a triggered slip in the adjacent fault segments (Mudurnu Valley and İznik Fault) was observed by the high spatial resolution and the large extend mapping capability of the InSAR technique (Wright et al., 2001, Feigl et al., 2002).

On November 12, 1999, 87 days after the devastating 17 August 1999 İzmit earthquake, the Düzce area was struck once more by a large earthquake (Çakir et al., 2003). The surface rupture of the 7.1 magnitude earthquake was 40 km long and the maximum right lateral offset was 5 m (Akyüz et al., 2002). Barka, 1999 had already defined the Düzce area as a potential seismic gap, noting that the Düzce Fault was the only unbroken segment of the North Anatolian Fault zone in the region. The earthquake caused at least 700 deaths and 2,600 injuries. At least 21,000 buildings collapsed in Düzce city during the two earthquakes.

Apparently, the 1999 events increased the Coulomb stress along the fault segment in the Marmara Sea (e.g., Parsons et al., 2000, Hubert-Ferrari et al., 2000, Cakir, 2003). Furthermore, due to the 1912 earthquake in the east and the 1999 earthquake in the west end of the Marmara Sea, a 150-160 km long segment remained unbroken beneath the Marmara Sea (Figure 1.2). Many researchers have considered this region to be a seismic gap that is capable of generating large earthquakes with potentially devastating effects on İstanbul. The gap shifted westward after the 1999 earthquakes. Hubert-Ferrari et al. (2000) suggested that

5.5 m slip had accumulated since the 1766 earthquake. If the earthquakes in the 20th century were repeating the rupture characteristics and time sequence of the 18th century earthquakes, a rupture along the fault segments beneath the Marmara Sea would complete the sequence in the next decades. Parsons et al. (2000) were more precise and suggested a 62 ±15% probability of a large earthquake (on the unbroken Marmara segment) during the next 30 years.

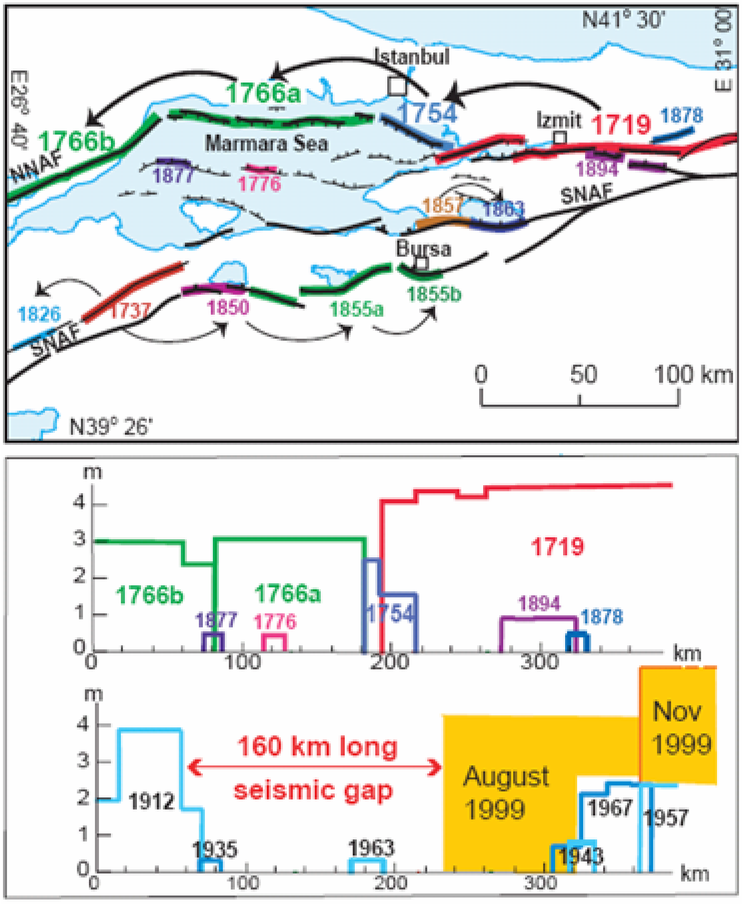

Figure 1.2 : Seismic gap in the Marmara Sea fault segments (from Hubert-Ferrari et al., 2000). a) Location of earthquakes between 1700 and1900, used by Hubert et al., 2000 to model 20th century earthquakes. b) In the 18th century, the whole Marmara region slipped (top) and by 1766 most of the accumulated slip would have been released. Since 1900, major events have released slip in the east and west of the Marmara Sea region (bottom). The slip due to the Izmit and Düzce events filled a gap to the east (See Figure 1.1 for the locations of the 20th century earthquakes).

1.3. Soil Liquefaction

Youd (1973) defines the liquefaction as the transformation of a granular material from a solid state into a liquefied state as a consequence of increased pore water pressures. For the saturated and unconsolidated soils, liquefaction occurs when the individual soil particles lose cohesion due to ground shaking. During this process, soil particles are rearranged and the contact forces between the particles decrease. The pore water pressures continue to increase until the soil particles can move independently from each other, or in other words, until the soil liquefies (Figure 1.3). As a result of liquefaction, the soil softens, weakens and may fail.

Although the soil liquefaction may occur during various seismic and environmental events, it causes the most damage to the built environment when it is triggered by earthquakes.

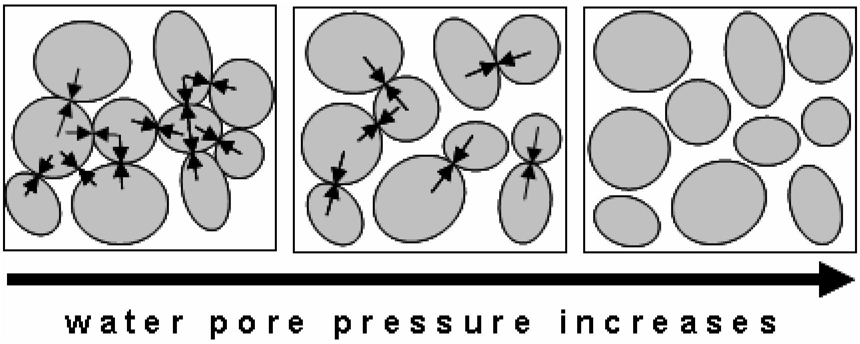

Figure 1.3 : Soil liquefaction. The contact forces between the soil particles decrease as the water pore pressures increases.

1.3.1. Deformation resulting from soil liquefaction

Youd (1984) suggests that displacement followed by liquefaction induced ground failure during the must be more than 10 cm to cause considerable damage to constructions. Perkins (2001) classifies soil liquefaction induced ground failure into five distinct types:

- Lateral spreads include the lateral displacement of surficial blocks of sediment as a result of liquefaction in a subsurface layer (Youd, 1984). They generally develop on nearly flat surfaces (slopes between 0.3° and 3°). They may be destructive to the subsurface structures (pipelines, bridges piers or building foundations). Fissures and scarps are indicators of this kind of ground failure.

- Flow failures are comprised of completely liquefied soil or blocks of intact material riding on a layer of liquefied soil (Tinsley et al., 1985). They develop on slopes of greater than 3°. To describe flow failures, the term landslide is sometimes used in the earthquake literature. Flow failure is the most catastrophic mode of ground failure induced by soil liquefaction. They can cause severe damage to constructions by shifting soil masses for long distances. Flow failures are common in coastal areas and may also occur under water.

- Ground oscillations occur either on flat terrain or on slopes that are too gentle to permit lateral displacement (Youd, 1984). Following the ground shaking, a nonliquefied layer oscillates various directions while the underlying soil layer liquefies. In spite of ground settlement and fissures, surface structures can resist to this kind of ground failure. In some cases, with the increase of water pressure under the solid layer of soil, water is ejected outside through the cracks or the weak parts of the soil. This interesting phenomenon is called “sand boils”. (Figure 1.4).

Figure 1.4 : Sand boils. The photo (from Canby, 1990) was taken after the 1989 San Francisco earthquake. One can observe from the photo how the liquefied sandy sediment found a crack to erupt through a nonliquefied soil layer. Note the extension and the volume of the ejected material. Bardet and Kapuksar (1993) explain the mechanism of the sand boils as the water, which may flow violently, usually transports considerable suspended sediments that settle and form a conical sand boil deposit around the vent. It is known that the eruption of sands start several minutes after the main shock can continue for almost an hour. Holzer et al. (2004) reported after the 2003 San Simeon Earthquake (CA, USA) that sand boils had started in 10 to 15 minutes and continued for 30 minutes. Many other sand boils varying in shape and size have been reported after known large earthquakes.

- Loss of bearing strength occurs when the liquefied layer of soil becomes weak to support overlying structures. Large deformations can occur allowing buildings to tilt, settle and sink. Buried structures (piles, tanks and utility pipelines) can float or rise buoyantly through the liquefied soil.

- Differential settlement occurs as some patches of the ground compacts and consolidates differentially after liquefaction. Ishihara & Yoshimine (1992) uses the term “post-liquefaction settlements of the ground”. They explain the term as the pore water pressure starts to dissipate mainly towards the ground surface, accompanied by some volume change (reduction) of the sand deposits, which is manifested on the ground surface as settlements. However, the settlements may not occur uniformly because of different conditions in the soil deposits. Differential settlements can cause major damage in the built environment. Ishihara & Yoshimine (1992) suggest that 30 to 70 cm ground settlements may occur after considerable liquefaction. Perkins (2001) considers differential settlements to be a common problem when the liquefaction occurs in artificial fills, particularly fills that have been emplaced during different times and using different techniques.

1.3.2. Liquefaction susceptibility

The liquefaction potential of a region is based on the liquefaction susceptibility of the deposits in the region and the likelihood of an earthquake strong enough to generate liquefaction. Liquefaction susceptibility can be mapped by delineating areas composed of saturated, cohesionless and granular sediments. Depending on the size and the location of a future earthquake, areas susceptible to soil liquefaction can be considered as having high liquefaction potential. Ground failures and associated damage should be anticipated in these areas during seismic shaking.

A number of methods for mapping liquefaction susceptibility have been proposed starting from the beginning of 1970's (e.g., Seed and Idriss, 1971, Youd and Perkins, 1978, Seed, 1979). Today, procedures to map liquefaction potential are relatively more standardized (e.g., USNHI, 1998) and public authorities of many metropolitan cities are more concerned about future seismic hazards (Tinsley et al., 1985 (Los Angeles, USA), Grant et al., 1992 (Seattle, USA), Knudsen et al., 2000 and Witter et al., 2006 (California, USA)), JICA & IMM, 2002 (İstanbul, Turkey).

Tinsley et al. (1985) who mapped the liquefaction potential in Los Angeles Basin (USA) explain the geological and hydrological factors that effect liquefaction susceptibility as: (1) the age and type of the sedimentary deposit, (2) the looseness of cohesionless sediment and (3) the depth to perched or other ground water. They summarize the criteria to map liquefaction susceptibility in Los Angeles Basin:

(1) They subdivided the late Quaternary deposits into three units as (a) the latest Holocene (during the past 1000 years), (b) the earlier Holocene (from 1000 about to 10.000 yr ago) and (c) the late and the middle Pleistocene deposits (during the past 0.5 m.y.). Then they determined the erosional and transport processes controlling grain-size, sorting, and bedding characteristics of sedimentary deposits. They named these processes as wind, beach and coastal terrace, coastal lagoon or marsh, river channel, levee, and flood basin, alluvial fan, debris flow. Finally, they classified the sedimentary deposits as (a) sand and silty sand, (b) gravelly sand or deposits containing less then 15% clay and (c) bouldary and cobbly gravels or deposits containing less then 15% clay. Later mapping susceptibility practices included artificial fills as young sedimentary deposits (e. g., Grant et al., 1992 and Witter et al., 2006).

(2) They analyzed standard penetration tests (SPT) from borehole logs to verify their qualitative estimates of liquefaction susceptibility based on the age of the generalized geological deposits. They used two earthquake conditions; either a nearby M 6.5 or a M 8.0 event. Their analysis showed that liquefaction susceptibility was strongly a function of the age and depth of the sediment and depth to the ground water.

(3) They classified the depth to ground water into four levels. The depths (a) less than ~3 m (b) from ~3 to ~9 m, (c) from ~9 to ~15 m and (d) more than ~15 m corresponded to high, moderate, low and very low susceptibility. But they also emphasized that the seasonal fluctuations in water levels affected their interpretation. In this context, USNHI (1998) suggests that the highest anticipated seasonal water elevation should be considered for initial screening and that at least 80 to 85 percent saturation is generally necessary condition for soil liquefaction.

Tinsley et al. (1985) compiled the susceptibility maps of Los Angeles Basin based on the criteria delineated above. Grant et al. (1992) and Witter et al. (2006) considered previous liquefaction events to evaluate the reoccurrence of soil liquefaction. Youd (1999) and the references therein highly recommend four field tests for evaluating soil liquefaction and compares them according to their advantages. These field tests are; (1) standard penetration test (SPT), (2) cone penetration test (CPT), (3) measurement of shear wave velocity and (4) becker penetration test (BPT).

1.3.3. Soil Liquefaction during the 1999 Izmit Earthquake

Soil liquefaction that caused damage to structures and lifelines was one of the devastating consequences of the 1999 Izmit Earthquake (e.g., Ansal et al., 1999, USGS, 2000, EDMRC, 2000). Field observations reported by JSCE, 2000 indicated that liquefaction was observed for a length of 120 km almost along the earthquake fault break within a band of about 10 km. During the earthquake, dramatic changes occurred along the southern coast of Izmit Bay by liquefaction induced coastal failures (Figure 1.6 and Figure 1.7). Adapazari had the most severe damage because of its location in the alluvial plains of Sakarya River (Figure 1.8). Locations of these incidents are shown in Figure 1.5.

Figure 1.6 (a) shows the southern shore of Sapanca Lake. The Sapance lake is situated in a pull-apart basin along NAF. During the earthquake, 50 m. of ground subsided into the lake. Cetin et al. (2002) recorded ground settlements of 20-50 cm and lateral spreads that reached a total of about 2m at the shore of the lake. Cetin et al. (2002) explained the geologic setting as lake deposits, as well as recent alluvium composed of alternating gravelly sand and silty clay layers deposited by the active river channel, underlying the Hotel Sapanca spit (the building complex in the photo).

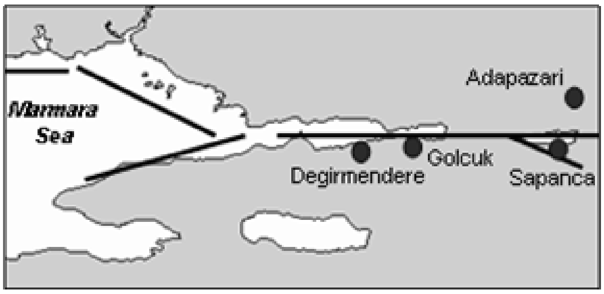

Figure 1.5 : The sites known to have experienced intense liquefaction (red dots) during the 1999 Izmit Earthquake. Blue line represents the main fault trace of NAF. The photos of the sites are given between Figure 1.6 and Figure 1.8.

As shown in Figure 1.6 (b), Degirmendere town was severely affected during the earthquake. According to the field investigations of Rathje et al., (2004); the inundated section of Degirmendere coastline had extended approximately 300 m along the coast and 75 m inland. They also observed that the seafloor slope inclination was reduced to about 5 degrees after the ground failure. Rathje et al. (2004) and Cetin et al. (2004) explained the cause of the slope failure as partial liquefaction of the underlying soil layers.

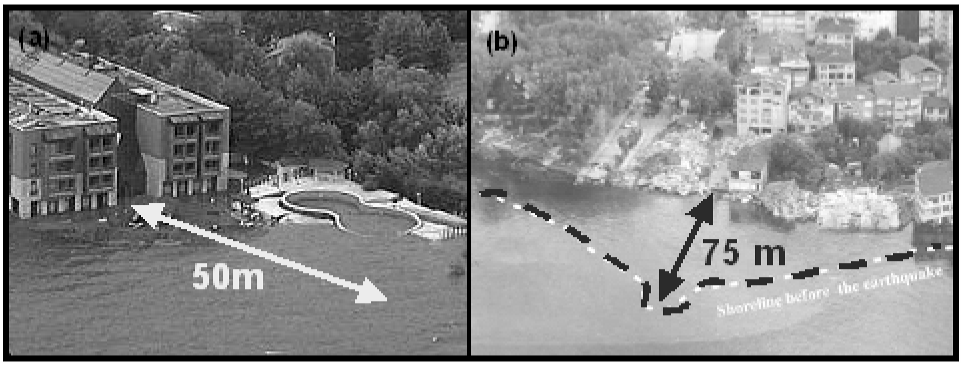

Figure 1.6 : Soil liquefaction during the 1999 Izmit Earthquake (1) (Photos from Ansal et al., 1999 and Cetin et al., 2004, respectively). (a) The southern shore of Sapanca Lake. (b) Degirmendere coast.

The damage at Golcuk downtown is presented in Figure 1.7 (a) and (b). The first photo was taken from a location known as Seymen. According to Rathje et al., (2004), the ground deformation in Seymen is a classical lateral spreading, but with only minor shoreline retreat and sea inundation. The cumulated lateral crack was estimated to be 2-4 m. At Golcuk downtown, the 300 m zone of intense sea inundation coincided with a steep Holocene delta fan of 15-10 degrees. Interpreted on this observation, Rathje et al., (2004) suggested that liquefaction-induced ground failure contributed to the localized inland subsidence in central Golcuk. It was also emphasized by Rathje et al., (2004) that 1.5 m vertical displacement on the Gölcük normal fault was responsible for the subsidence as well as the liquefaction.

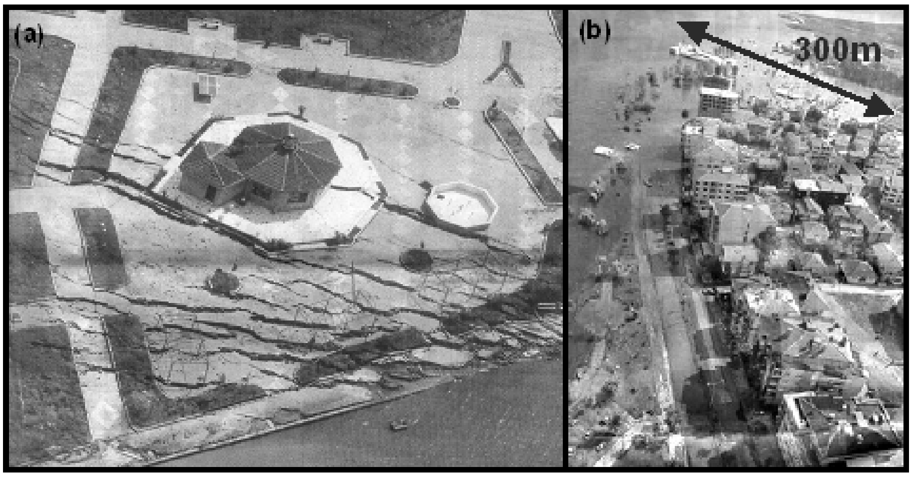

Figure 1.7 : Soil liquefaction during the 1999 Izmit Earthquake (2) (Photos from Bogazici University, KOERI). (a) Gölcük coast (Seymen). (b) Gölcük downtown.

The most severe damage to buildings due to liquefaction occurred in the city of Adapazari. The city is situated in the alluvial plain formed by Sakarya River that has a shallow water table. Most building damages in the city were associated with the loss of bearing strength caused by liquefaction of subsurface soils. In EDMRC, 2000, the most remarkable damages in the district were explained as settlements, inclination of buildings and up-heave of ground around the buildings. USGS (2000) and JSCE (2000) reported sand boils that appeared gradually from the ground. Two buildings at Adapazarı downtown are presented in Figure 1.8 (a) and (b). For the building in the first photo, USGS (2000) reported that it had sunk 1.5 m uniformly into the ground and soil beneath the building was pushed outward from beneath the building. For the other building, EDMRC (2000) reported that it had tilted from 30° to 60° in 10 days. Mollalahmutoğlu, et al. (2003) emphasized that the asymmetric structure of the building (see the attached penthouse on the roof) had also contributed to its inclination.

1.4. Objectives

In this thesis, I am concerned with the measurements of the surface deformation in urban environment using radar interferometry techniques. The questions addressed in this thesis were originated from some incidents occurred during the past years. These incidents are;

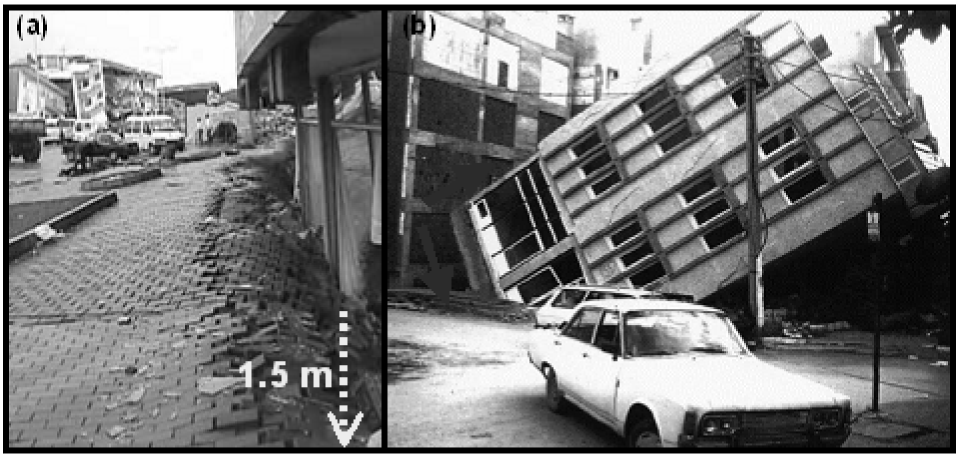

Figure 1.8 : Soil liquefaction during the 1999 Izmit Earthquake (3) (Photos from USGS, 2000 and Mollalahmutoglu, et al. 2003, respectively). The buildings in (a) and (b) were located in the city of Adapazari.

(a) The 1999 Izmit Earthquake. Recovering from this devastating earthquake; science community as well as the Turkish authorities concentrated on the future earthquake near the city of İstanbul. Huge efforts are exerted on the issues of earthquake hazard mitigation and risk management.

(b) New InSAR techniques proposing point target analysis for deformation analysis. In the late 1900's; new InSAR techniques were introduced to the radar community. These techniques enabled researchers to reconsider the value of the 15 years old ERS data archive.

(c) Terrafirma's initiative to provide ground motion hazard information across Europe. Terrafirma, run by ESA-Global Monitoring for Environment and Security (GMES) program, prepared "maps of ground and building motion" of more than 20 cities in Europe by using InSAR techniques (Closset & King, 2005). During this time, Terrafirma also produced a ground motion map of İstanbul (Figure 1.9). Excluding scientific background of the production steps, they presented the map as a case study (UKNERC, 2004, Aktar & Browitt, 2006). The map showed some "hot spots" of negative vertical motion (or "subsidence") in the city of İstanbul (Figure 1.9). As a preliminary, landslides, surface mineral workings, ground-water extractions, underground construction, superficial constructions, and seismicity were considered to be the potential ground motion mechanisms in İstanbul metropolis (Closset & King, 2005).

Main research objectives of the thesis are to:

(a) Master “persistent scatterer” InSAR,

(b) Establish a road map to measure slow and long-term surface deformation,

(b) Measure surface deformation in İstanbul metropolitan area,

(c) Describe physical models of deformation,

(d) Determine the role of current deformation in earthquake hazard risk management (Figure 1.10).

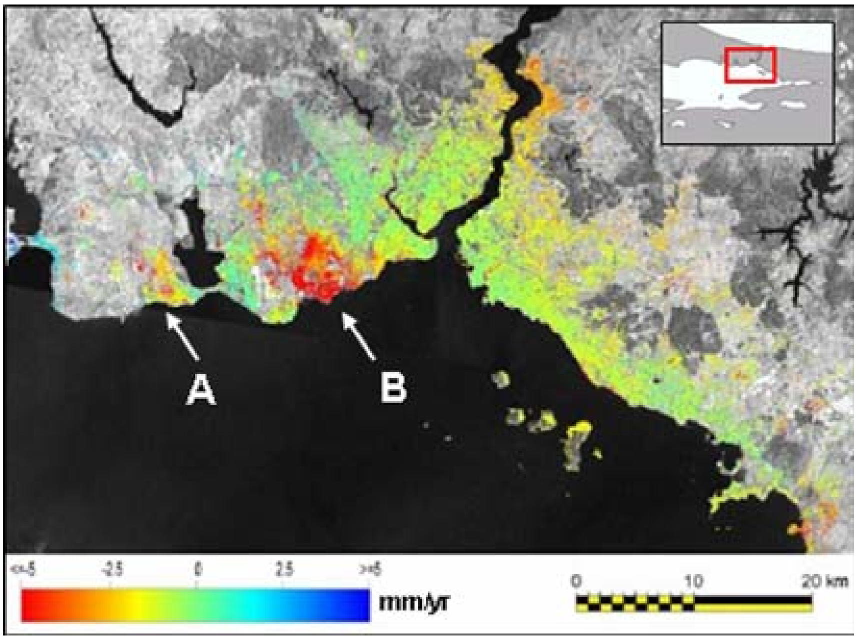

Figure 1.9 : Ground motion map of İstanbul produced by GMES Terrafirma (UK NERC, 2004, Aktar & Browitt, 2006, Closset & King, 2005). Average annual motion rate is represented from red to blue in mm/yr. Arrow A points Avcilar County where some negative vertical motion are noticed. Arrow B points Bakirkoy and Zeytinburnu counties. These regions appear to subside with a rate of 5 mm/yr.

These objectives are addressed in the following 4 chapters of this thesis.

Chapter 2 introduces radar interferometry. So it starts with synthetic aperture radar (SAR) principles and continues with the theory of InSAR. In the InSAR section, a detailed description of error sources in phase measurements and some important aspects of data processing in relation to geophysical applications are described. Point target analysis in INSAR known as “persistent scatterers” is presented at the end of Chapter 2.

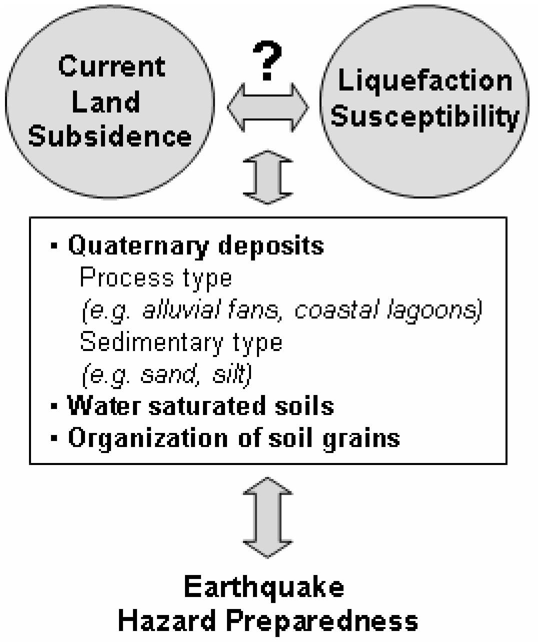

Figure 1.10 : The role of current land subsidence and soil liquefaction in earthquake hazard preparedness. In the rectangular area, some common soil characteristics of soil liquefaction and subsidence phenomena are noted.

Chapter 3 is concerned with the InSAR measurements of the surface deformation in one of the counties of İstanbul, Avcilar. This chapter also includes the physical explanations and the modeling of the deformation. Chapter 4 concentrates on the consequences of the surface deformation in the region of interest.

Chapter 5 presents the conclusions that are composed of final remarks, discussion and future directions.

2. MEASURING SLOW MOTION GROUND DEFORMATION BY SATELLITE RADAR INTERFEROMETRY

Graham published an early study describing the potential of interferometry on pairs of synthetic aperture radar (SAR) images for mapping topography in 1974. In the late 1980's, airborne experiments established the basics of radar interferometry (InSAR, sometimes also referred to as IfSAR) (Zebker & Goldstein, 1986; Goldstein & Zebker, 1987). Later, the technique was extended to radar data acquired by the Seasat satellite and the SIR-B shuttle mission (Li & Goldstein, 1990; Gabriel & Goldstein, 1988; Goldstein et al., 1988). The capability of radar interferometry to measure ground motion was demonstrated by Gabriel et al., 1989. The potential of the technique for deformation mapping was validated by Massonnet et al. (1993) and Zebker et al. (1994) who mapped the co-seismic deformation field of the Landers Earthquake.

This chapter starts with a brief introduction to SAR. This part is based on the books of Curlander & Mc Donough (1991) and Elachi (1987). Radar data processing principles from radar interferometry point of view are mainly described from Hanssen, 2001. Quite a number of reviews and books on theory and applications of InSAR have been published since last decade, e.g., Massonnet & Feigl, 1998; Hanssen, 2001; Madsen & Zebker, 1998; Burgmann et al., 2000; Rosen et al., 2000; Gens & Van Genderen, 1996, Bamler & Hartl, 1998. The InSAR sections, giving brief introduction to this study, are compiled mainly from these references. All the technical descriptions are based on European Space Agency's radar AMI aboard of the ERS satellites. The last part focuses on the analysis of slow motion deformation analysis by InSAR and gives a summary of recent studies.

2.1. Synthetic Aperture Radar

Synthetic aperture radars (SAR) and the side looking real aperture radars work on similar principles. The radar (RAdio Detection and Ranging) as an active sensor illuminates the terrain at particular microwave wavelengths ranging from 1 cm to 1 m receives the signals reflected from the terrain.

The radar, carried on an aircraft, spacecraft or a satellite platform, scans the terrain with the forward motion of the platform (Figure 2.1). The illuminated area is the “footprint” of the radar. The flight direction of the platform is called the “along track” or the “azimuth”. The direction of the radar pulses sent to the surface with a certain “look angle” is perpendicular to the flight direction, and called “across track” or referred to as “range”. With the increasing look angle, two-way path of the radar pulses increases from “near range” to “far range”. The radars measure the “slant range” distance along the “line of sight” (LOS) of the radar. For the maps and spatial products, the inclined slant range has to be projected to the “ground range”.

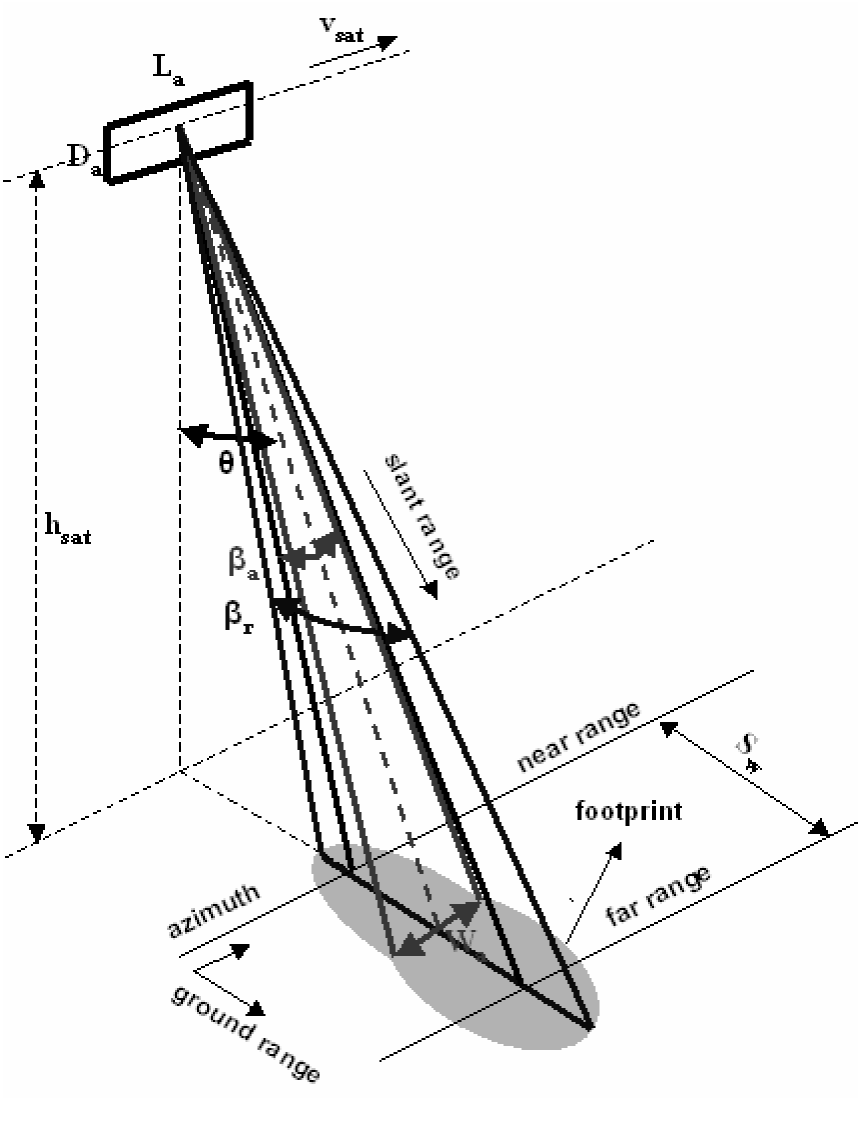

Figure 2.1 : Imaging geometry of a SAR system. See Table 2.1 for the list of parameters.

In this thesis, interferometric SAR analysis are based on the data acquired by Active Microwave Instrument (AMI) on board of the Earth Resources Satellite (ERS) satellites. Therefore, only the parameters of this C-Band system will be given through this chapter. See Table 2.1. for the geometrical parameters of AMI on ERS platforms.

Table 2.1 : Geometrical parameters of AMI on board of the ERS satellites.

ERS Active Microwave Instrument AMI		
h_{sat}	Satellite altitude	785 km
v_{sat}	Ground track velocity	7.6 km/s
L_a	Antenna length	10 m
D_a	Antenna width	1 m
S_w	Image swath width	100 km
W_a	Antenna footprint width	4.8 km
β_r	Range beam width	5.4°
β_a	Azimuth beam width	0.23°
R	Near / middle / far range (km)	826 / 844 / 865
θ	Near / middle / far look angle	20.1° / 23.0° / 25.9°

Hanssen (2001) summarizes the AMI sensor characteristics as in the following: The AMI generates a radar pulse with a “pulse duration” of 37.1 μs. This pulse is generated and since it needs to be shaped into a “chirped pulse” with varying frequency, the signal is fed into a dispersive delay time. To make the pulse longer, this device produces a linear “frequency modulated” (FM) chirp with a “bandwidth” B of 15.55 MHz. This corresponds to a “pulse length” Γ of 64 ns (1/B). The rate at which consecutive chirps are generated is the “pulse repetition frequency” PRF which is programmable in the range 1640-1720 Hz (Hanssen, 2001). A typical PRF of 1680 Hz results 10 transmitted pulses before the first pulse returns to the antenna. Before transmitted, the chirp is shifted to a “carrier frequency” f_0 of 5.3 GHz (C-band wavelength). When the radar signal is received, it is converted into a image data with a “sampling frequency” of 18.96 MHz. Both real and imaginary parts of the signal are stored in one byte.

“Range resolution” corresponds to the minimum distance between two points along the ground range which can still be separable. The smallest time difference that can be discriminated is $1/PRF$. Then, the ground range resolution X_r is given by

$$X_r = \frac{c}{2B\sin\theta} \tag{2.1}$$

where c is the speed of light, θ is the look angle, B is the bandwidth of the radar. For ERS configuration, the range resolution is ~25 m in the middle range (θ=23°).

Similar to ground range, two points along azimuth can only be resolved if they are not within the same azimuth beam width. The “azimuth resolution” is the minimum distance between those points and corresponds to the radar footprint width,

$$W_a = \frac{h_{sat}\lambda}{L_a \cos\theta} \qquad \textbf{(2.2)}$$

where λ/L_a is the azimuth beam width. If we considered ERS as a side looking real aperture radar, the azimuth resolution in the middle range (θ=23°) would be 4.8 km. Moreover, to achieve better resolution in azimuth, antenna size should be much larger than several kilometers. To solve this problem, complex processing techniques referred to as “SAR focusing” are applied.

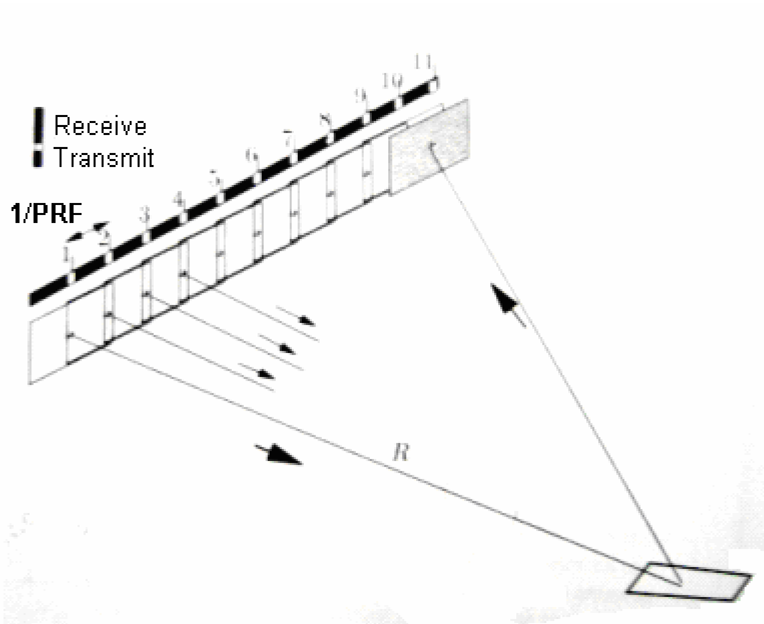

Figure 2.2 : SAR pulse transmitting and receiving mode (from Hanssen, 2001). For ERS, the transmitted pulse in position 1 is received between position 10 and 11. If the SAR instrument transmits the radar pulse each 1/PRF s, then the ERS moves 40 m between transmitting and receiving.

SAR focusing techniques are based on the “Doppler shift” concept. Briefly, they “synthesize” a larger antenna by using a series of consecutive pulse returns from the same point scatterer on the ground. SAR focusing leads to a radar image with high resolution of the order of a meter (Figure 2.2).

Several electronic algorithms for SAR focusing have been developed since its first demonstration by Graham (1974) (Hanssen, 2001 and the references therein). In this thesis, I used the PRISME architecture developed by French Space Agency (CNES) (Massonnet et al., 1994).

The antenna pattern of the ERS SAR is aimed almost exactly perpendicular to the sum of the flight direction vector and the velocity vector due to the earth's rotation. However, there is always a slight "squint angle" ω_s of the platform (Figure 2.3). Regarding the squint angle of the antenna, the Doppler frequency f_D for a target relatively approaching towards the satellite is

$$f_D = \frac{2v_{sat}}{\lambda}\sin\omega_s \sin\theta \qquad \textbf{(2.3)}$$

Note that the relative spacecraft velocity v_{sat} is decomposed to the direction towards the scatterer with $\sin\omega_s\sin\theta$. The center frequency of the passage of a point scatterer through antenna beam is termed the "Doppler centroid frequency" f_{DC} whereas zero-Doppler, $f_D=0$, denotes the direction in which the Doppler frequency is equal to zero (Hanssen, 2001). In other words, this direction is perpendicular to the flight direction of the satellite.

The variation of the Doppler frequency during the passage of the scatterer through the beam is expressed by the "Doppler bandwidth" as

$$B_{Dop} = \frac{2\beta_a v_{sat}}{\lambda} \qquad \textbf{(2.4)}$$

where β_a is the azimuth beam width of the antenna and the v_{sat} is the relative spacecraft velocity (Hanssen, 2001). The radar PRF should be smaller than B_{Dop} to sample Doppler spectrum. Note that, for ERS, B_{Dop} is 1377 Hz and the PRF is 1680 Hz. The Doppler bandwidth determines the azimuth resolution of the focused SAR image, using

$$X_a = v_{sat} / B_{Dop} = L_a/2 \qquad \textbf{(2.5)}$$

To improve the azimuth resolution, the radar requires a shorter wavelength, a wider antenna beam width and a faster moving platform. Consequently, the SAR focusing improves the azimuth resolution of ERS from 4.8 km to 5 m.

Doppler centroid can be estimated using the phase difference between the neighboring pulses for the same range distance (Hanssen, 2001). In practice, Doppler centriod frequency is expressed as a fraction of the PRF (f_{DC}/PRF). For example, if we find an average of phase shifts due to the Doppler frequency as 0.3 cycles, the estimated Doppler centroid frequency for the PRF of ERS (1680 Hz) will be 504 Hz. Using the equation 2.4, we find $\omega_s = 0.27$ degrees for ERS (v_{sat} = 7554 m/s). For focusing the SAR, f_{DC} is important for minimizing the noise associated with the squint angle of the antenna. This also has to be considered during processing the interferometric SAR pairs.

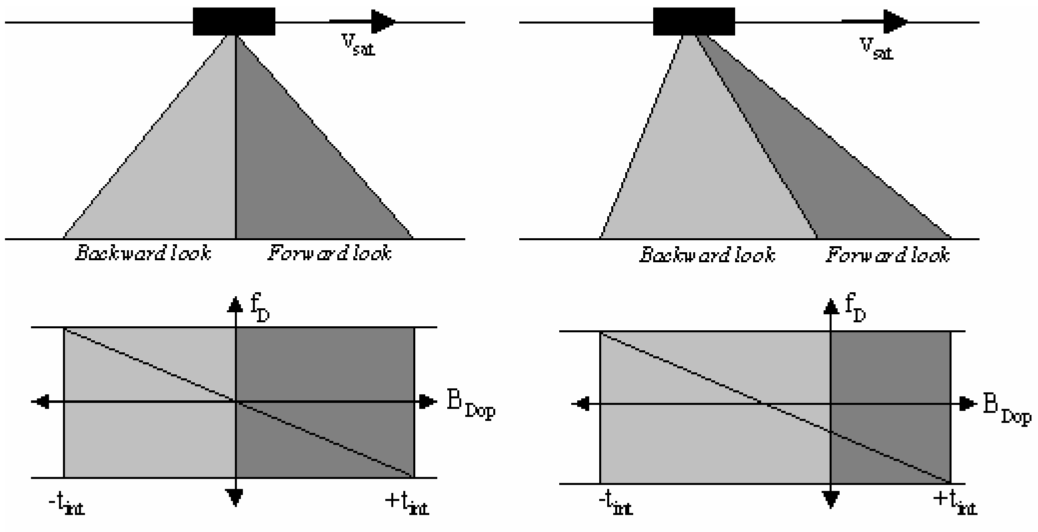

(a) **(b)**

Figure 2.3 : Doppler centroid configuration (from Souyris, 2003). (a) Zero-Doppler centroid (b) Non-zero Doppler centroid.

2.1.1. SAR Image characteristics

The dielectric properties of a material is related to its conductivity. For radar imaging, a high dielectric coefficient implies moisture in or on the ground. As the wetness of the surface increases, the penetration depth of a radar signal decreases (Curlander, 1991). This causes high radar reflectivity but low signal return. Fresh snow, young lavas, watered vegetation, forest canopy or wet soil appear relatively dark on radar images because of this phenomenon. It is possible to discriminate between surface types since they retain different amounts of moisture (Henderson, 1998).

If the surface is smooth, the radar signal is reflected away with a reflection angle equal to its incidence angle. This case, called specular reflection occurs for incidence angles less than 30° from the vertical. So in radar images, calm water surfaces appear dark. However, two or three planar and smooth surfaces at right angles to each other can produce high radar returns if they are properly oriented towards the radar. Such settings are called dihedral or trihedral “corner reflectors”, depending on the number of planar surfaces they include. Corner reflectors occur in a variety of natural settings such as sharp vegetation boundaries, river banks parallel to the flight direction, certain rock formations, boundaries between clear cut and forest (Henderson, 1998). But such features are mostly found in anthropogenic environments. Sidewalks, buildings, railroads and bridges in urban areas, forming smooth surfaces, straight lines and sharp angles, act as corner reflectors and appear very bright in radar images.

As the length scale of the rugosities on the surface increases, the radar signal becomes more diffuse and is reflected to all directions. This phenomenon is “surface scattering”. Most natural objects are diffuse reflectors, or scatterers, sending some part of the signal back to the radar. This behavior depends on the scale of the roughness and on the radar wavelength.

At the “micro-scale”, surface roughness depends on Rayleigh criterion (Hendersen, 1998). If the incidence angle is smaller then 30^o, then the Rayleigh condition for specular reflection applies:

$$h_{rms} > \lambda / 8\cos\eta \qquad \textbf{(2.6)}$$

where h_{rms} is the rot mean square variation in height, λ is the radar wavelength and η is the local incidence angle. On flat ground, the local incidence angle η is equal to the look angle of the radar (see Figure 2.4 in the next section). The scale of roughness determines the magnitude of radar backscatter within a resolution cell which is called “backscatter cross section”.

For incidence angles larger then 30^o, the Bragg model can be used. In the case of ERS, in most urbanized areas, however, this model does not apply because the mean surface slope is less than about 30^o.

Meso-scale roughness on the ground exhibits variations on a scale several times the resolution cell of the radar system. At this scale, it is possible to discriminate various canopy structures of vegetation. Macro scale roughness, a function of the terrain slope, produces effects such as “foreshortening” and “layover” on the radar image.

“Volume scattering” implies that the transmitted radar signal has been reflected mostly from multiple targets such as leaves, branches, trunks, bushes, grasses and soil. So, the part of signal that returns to the radar, is the result of this three dimensional scattering environment. Such inhomogeneous surfaces can be characterized as a collection of uniformly distributed identical scatterers (Elachi, 1987). Long wavelengths, such as L-Band, can penetrate a forest canopy while ERS C-Band radar signals scatter from the plant stalks and branches.

The value of phase for a pixel depends on the phase shift resulting from the interaction of the signal with the ground surface and also, the two-way path length, or the round trip distance traveled by the radar signal between the satellite and the ground.

Since the radar wavelength is much smaller than the pixel dimension on the ground, we can think of each pixel as consisting of hundreds of individual scattering targets. For C-band images from the ERS, ENVISAT and RADARSAT satellites, the radar wavelength is 5 cm, roughly at least 250 times smaller the optimal pixel dimensions of 12.5 m in the azimuth direction. The phase resulting from the sum of all these individual targets is therefore random. The phase is then the argument of a complex number that is the sum of hundreds of unknown complex numbers. This is the reason why a single phase image appears as a noisy image with phase values uniformly distributed between –1/2 and +1/2 cycles. Although it is random from one pixel to another in an image, the internal phase contribution remains the same on a given pixel from one image acquisition time to another under certain conditions (CNES, 1998). That is, the image phase becomes meaningful only when it is compared with another image phase acquired under similar conditions. SAR interferometry is based on this concept of differencing pairs of images acquired at different times (epochs).

2.1.2. Topographic influence

On flat ground where the local incidence angle η is equal to the look angle θ, the ratio between the ground and the slant range is related to $\sin\theta$ (Figure 2.4 (a)). As the local slope increases, additional geometric distortions occur in the cross track (range) direction of the radar images (Curlander & Mc Donough; Elachi, 1987). If the local topographic slope is less than the incidence angle η, then the sloped ground cannot be projected to the image plane in its actual length. That is, a ground facing the radar (where $\eta= \theta - \alpha$) will be imaged as shorter whereas ground sloping away from the radar (where $\eta= \theta + \alpha$) will be imaged longer than its actual length. These effects on radar images are termed “foreshortening” and “lengthening” (Attema, 1998) respectively. Practically, the side of a hill toward the radar will be shortened and will appear brighter on the image than the other side sloping away. If a digital elevation model is available, it is possible to correct these effects. Figure 2.4 (b) shows only the foreshortening effect.

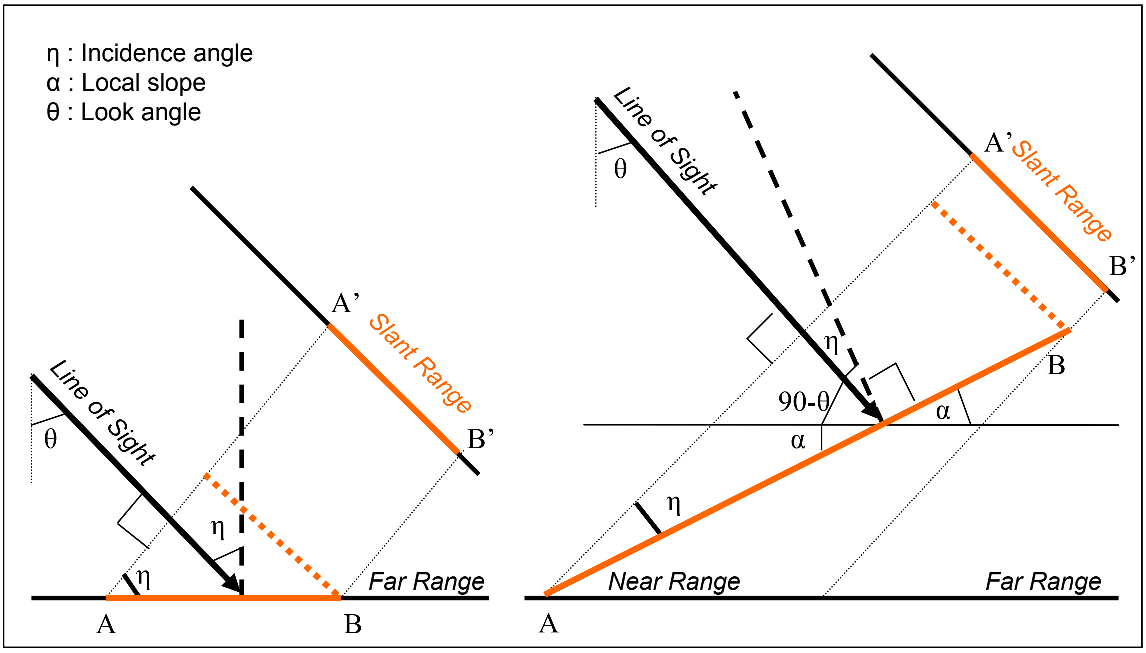

(a) Flat ground (b) Sloping ground

Figure 2.4 : Slant and ground ranges described in terms of look angle θ, local slope α and incidence angle η. a) Projection of a flat ground to the slant range, where local slope α is zero ($\alpha = 0$). In this case, incidence angle η becomes equal to look angle θ of the satellite ($\eta = \theta$). Then the projected length A'B' becomes $AB\sin\theta$. b) Projection of a sloping ground to the slant range, where local slope α is smaller than the incidence angle ($\alpha < \eta$). In this case, incidence angle η becomes equal to the difference between the look angle θ and the local slope α ($\eta = \theta - \alpha$). Then the projected length A'B' becomes $AB\sin(\theta - \alpha)$.

An extreme case occurs when the local slope α exceeds the incidence angle η (where $\alpha \geq \eta$) (Figure 2.5). In this case, the top of a mountain is at a closer slant range than its base. This means the peak of a mountain will be imaged before its base. This phenomenon called "layover" makes hill slopes facing the radar look "laid over" the region in front of them. In addition, their summits appear bright. ERS, with a look-angle of 23° in the middle range, causes steep incidence angles in the sloped landscapes. So in ERS case, layovers occur for slopes greater than 23°, which occurs only in the most extreme mountainous terrain. Another extreme case is the radar "shadow". It occurs when a peak of a steep slope prevents the radar beams from illuminating the slope surface facing away from the radar (Figure 2.5). This effect creates discrete dark regions on the radar image. So, in the case of shadowing, the pixel in the image contains no information from the ground. It is not possible to recover radar images from either of these local effects.

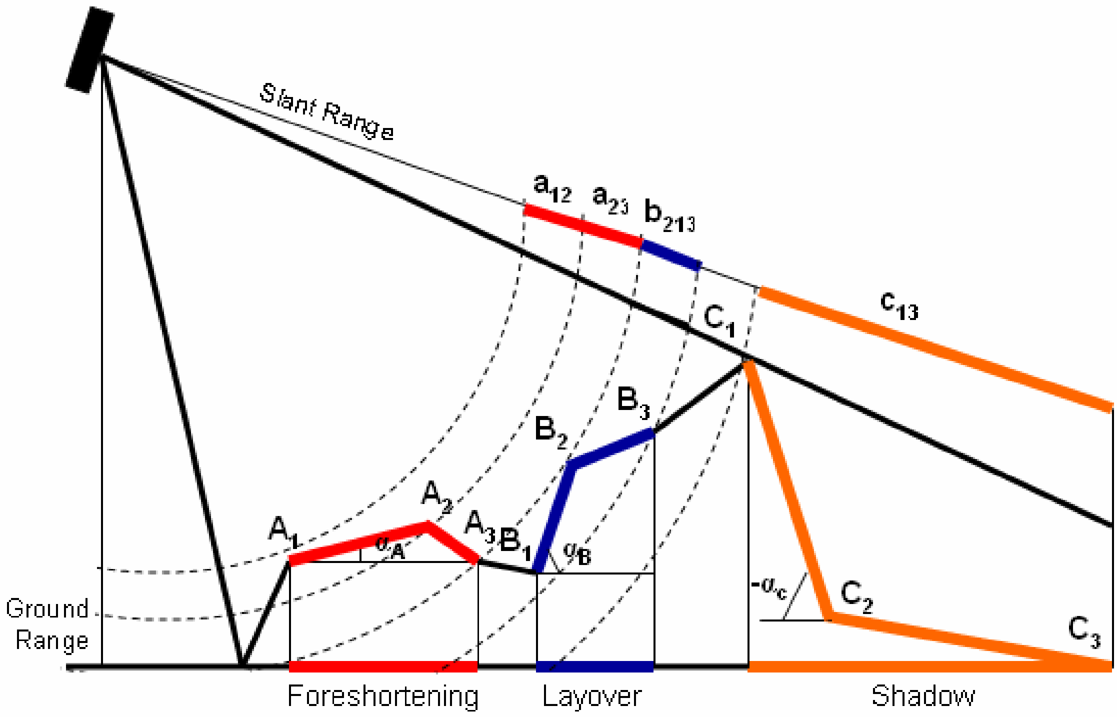

Figure 2.5. Distortions on the radar images caused by topographic slope. In foreshortening, A1A2 and A2A3, will not appear in their actual lengths. Notice that a12 is shorter than A1A2 and a23 is longer than A2A3. In layover, B1B2B3 will appear as b213 because B2 will be imaged before B1. In shadow, C1C2C3 will be imaged as c13. But c13 will appear totally black on the image.

2.2. Synthetic Aperture Radar Interferometry

2.2.1. Principals of radar interferometry

Radar interferometry is a technique that calculates the phase difference between two radar images acquired using slightly different viewing geometries. The resultant interference pattern is called an "interferogram". If certain conditions are met, the phase differences form spatially coherent fringes. Each fringe represents a difference of one cycle of the two-way travel time between the radar aboard the satellite and the target on the ground. Interpreted in units of distance, each fringe represents half the radar wavelength in change of distance, or 28 mm for C-band radars like ERS and ENVISAT. The production of an interferogram is in principal a straightforward procedure (Burgmann et al., 2000). However, planning a study based on radar interferometry and interpreting the interferometric results for a specific application can be complicated.

In principle, the interferometry imaging geometry has a stereoscopic character (e.g. Massonnet & Feigl, 1998; Burgman et al., 2000; Rosen et al., 2000). Therefore, the imaging configuration can be formed by either two antennas on a single platform or one antenna acquiring images at two distinct times. The first case is called "single pass (or single track) interferometry" and the other case as "repeat pass (or repeat track) interferometry".

Figure 2.6 shows the geometry of the repeat pass satellite interferometry. The technique is based on a simultaneous "orbital separation" B that is formed through a "temporal separation" Δt_{12}. Actually, the satellite is supposed to pass in nearly the same trajectory to cover an area twice with the same viewing geometry. For ERS satellites, orbital separation typically ranges from 10 m to several kilometers. Orbital baseline can be interpreted in parallel and perpendicular components, $B_{||}$ and $B\perp$. The parallel component corresponds to the range difference and the perpendicular component is important for the assessment of the stereoscopic quality. The temporal separation Δt_{12} is the time difference between two epochs, t_1 and t_2 that depend on the revisit program of the satellite. If the ground moves between two image acquisition, the difference of the two phase measurements ($\Delta\Phi_{12} = \Phi_2 - \Phi_1$) gives the "line of sight" component of the displacement, d.

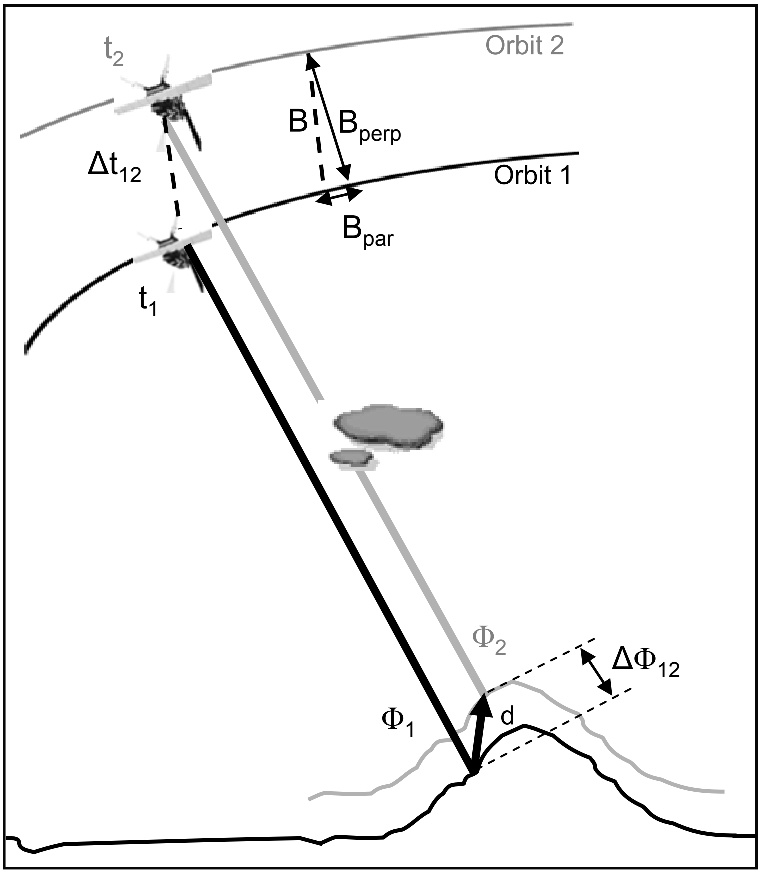

Figure 2.6 : Repeat pass radar interferometry for space borne systems.

A radar image is a two dimensional table of pixels recorded as complex values. Each pixel can be decomposed into amplitude and phase components. In two radar images, the same pixel, s_1 and s_2, will be represented with its amplitude values, A_1 and A_2 and phase values, Φ_1 and Φ_2. An interferogram is the point-wise product of one image with the complex conjugate of the other image (Burgman et al., 2000).

$$s_{12} = s_1 s_2^* \quad \textbf{(2.7a)}$$

So, the value of the same pixel in the interferogram, s_{12}, becomes

$$s_{12} = A_1A_2 (\cos(\Phi_1-\Phi_2) + i \sin(\Phi_1-\Phi_2)) = A_{12}\, e^{i(\Phi_1-\Phi_2)} \quad \textbf{(2.7b)}$$

Note that the interferometric phase Φ_{12} is the phase difference between two radar images Φ_1-Φ_2 while the interferometric amplitude A_{12} is actually the product of the amplitudes A_1A_2:

$$s_{12} = A_{12} (\cos(\Phi_{12}) + i \sin(\Phi_{12})) = A_{12}\, e^{i(\Phi_{12})} \quad \textbf{(2.7c)}$$

We say that the phase is the measure of the round trip distance along range. So, absolute phase Φ inherits an ambiguity n about the integer number of cycles (Figure 2.7). Accordingly, the measured phase difference is only the fractional part of the range change. Mathematically, the interferometric phase is the modulo 2π radians (1 cycle). The interferometric phase Φ appearing in color cycles (fringes) on an interferogram is called “wrapped phase”. In some cases, constant offset Φ_o can also be introduced to avoid relative phase measurements. To find the absolute phase, the ambiguity represented by the integer n should be resolved. This process is called “phase unwrapping” and the resultant phase the “unwrapped phase”.

$$\Phi = \Phi + \Phi_o + n \quad \textbf{(2.8a)}$$

$$\Phi = wrap(\Phi) \quad \textbf{(2.8b)}$$

The simplest method to unwrap phase is simply to count the successive fringes along a profile (Massonnet & Feigl, 1998). On the other hand, very sophisticated unwrapping algorithms have been developed. Their success may depend on numerous parameters (land cover type, nature of the deformation etc.). For example, unwrapping clear interferograms showing coseismic fringes of a strong shaking may be very straightforward. On the other hand, unwrapping noisy interferograms indicating subsidence over a long time interval may be challenging. Phase unwrapping as a separate subject in data processing is beyond the scope of this thesis.

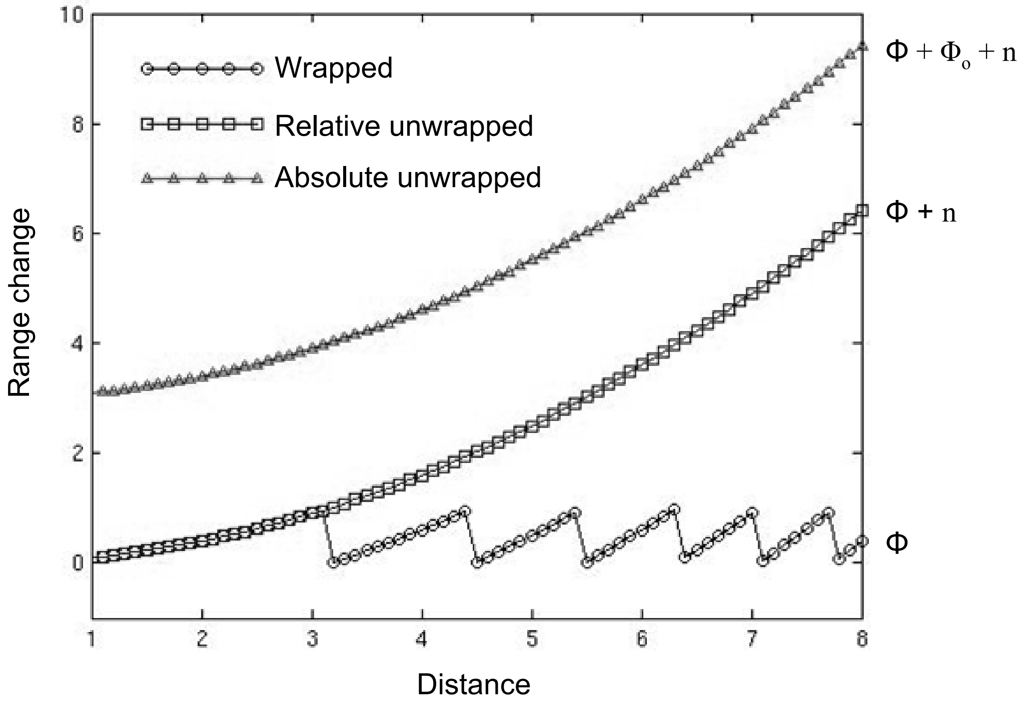

Figure 2.7 : Unwrapped phase.

2.2.2. European Space Agency ERS SAR satellites

ERS-1 was launched by the European Space Agency in 1991 and operated until March 2000. The mission was planned to provide essential data for oceanographic and atmospheric studies. The payload consists of various instruments for various functions. The Active Microwave Instrument AMI was designed to acquire SAR amplitude imagery. It was not optimized for interferometry. The orbit control and the data distribution policy resulted in impressive advances in science and major improvements in radar interferometry (Hanssen, 2001).

ERS-2, a twin copy of ERS-1, except one more instrument for atmospheric observations, was launched in 1995. Both satellites operated together, called “tandem mission” for a year. ERS-2 followed ERS-1 in the same orbit within a 1-day interval. After 1996, ERS-1 acted as a backup satellite in hibernation mode, and was only activated for special occasions, mostly related to radar interferometry (Hanssen, 2001).

The continuity of the ERS missions for almost 15 years has provided a unique data archive which is very valuable especially for observing slow motion deformations occurring over long time intervals (Table 2.2). Moreover, the steep incidence angle of ERS (~23°) is advantageous particularly for measuring subsidence phenomena since its steep incidence, which causes fewer shadows, is more sensitive to vertical displacements. On the other hand, its short wavelength (~5 cm) causes temporal decorrelation over long time intervals.

Table 2.2 : ERS's most important system parameters for radar interferometry

ERS Active Microwave Instrument AMI	
Carrier Frequency, f_0	5.3 GHz (C-band)
Range Bandwidth, B	15.55 MHz
Middle Look Angle, θ	23°
Revisit Time	ERS-1 : 3, 35 or 168 days ERS-2 : 35 days Tandem mode: 1 day
Swath Width	100 km
Full Image Frame	100 x 100 km
Satellite Altitude	790 km
Orbital Inclination	98°

For interferometry studies, it is important to consider some aspects of the ERS mission history (Table 2.3). For ERS-1, only two mission phases, phase C (from April 1992 to December 1993) and phase G (from March 1995 to December 1998), are convenient for interferometry studies. These phases have a 35-day repeat cycle. During phase G, ERS-1 operated in a tandem mission with ERS-2.

Table 2.3 : Mission history of ESA SAR satellites (see the text for explanations).

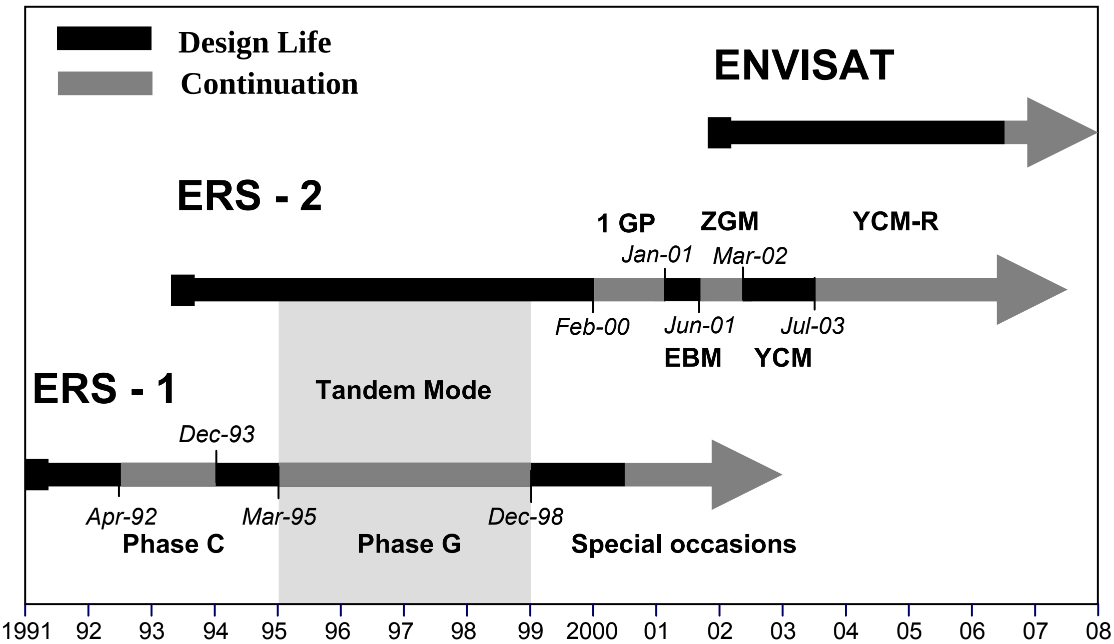

As described by Miranda et al. (2005) in detail, ERS-2 lost two of its three gyroscopes in February 2000 and continued the mission in "Mono-Gyro Mode" (1-

GP) until January 2001. After six months in “Extra Back-up Mode” (EBM), “Zero-Gyro Mode” (ZGM) software was activated onboard to control the satellite’s stability in June 2001. This led to an immediate improvement in pointing performance from ± 10° to ± 5° on the yaw axis which was originally ± 0.2° in 3-GP mode. At the beginning of 2002, the performance was further improved with the implementation of the “Yaw Control Monitoring Mode” (YCM) that constrained the yaw to within ±4°. Nevertheless, this evolution significantly affected the stability of the satellite attitude and the SAR Doppler Centroid frequency (Miranda et al., 2004). In July 2003, the ERS-2 type recorder was declared to be unavailable. This situation did not affect the SAR image mode directly but made the retrieval of Doppler Centroid information extremely difficult. Consequently, it was attempted to modify YCM mode so that ERS-2 would operate within a limited orbital coverage. Miranda et al., 2004 call this mode “YCM-Regional Operations” (YSM-R).

Although ERS-2 acquired images as late as 2005, their usefulness for interferometry is limited by large deviations in Doppler Centroid. ESA published statistics of the Doppler Centroid values for particular tracks and frames so that users could select proper data pairs by comparing their Doppler Centroid values (http://earth.esa.int/pcs/ers/sar/doppler/) (Figure 2.8).

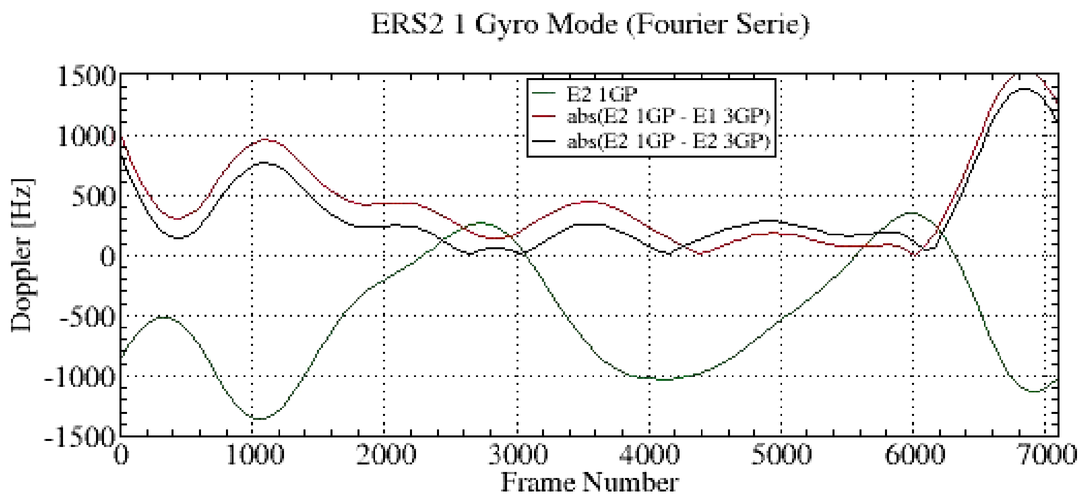

Figure 2.8 : Average Doppler Centroid frequency of ERS-2 during Mono-Gyro Mode (in green). The differences from the Doppler Centroid frequencies of ERS-1 and ERS-2 during Three-Gyro Mode are shown in red and black. (http://earth.esa.int/pcs/ers/sar/doppler/)

ESA’s next radar mission was called ENVISAT. It was designed to provide the continuity of the observations started with ERS program. The satellite has been designed particularly to enhance the ice and the ocean missions of the ERS program and to extend the contributions to environmental studies in the area of atmosphere chemistry and marine biology. The ENVISAT satellite, launched in March 2002, has a combination of ten multi-disciplinary sensors. The Advanced Synthetic Aperture Radar (ASAR) acquiring radar imagery in C-Band, is one of those payload instruments.

Compared to the ERS 1-2 AMI, the ASAR is a significantly advanced instrument employing a number of new technological developments (ASRA-SAG, 1998, Louet, 2001). The primary technical feature of ASAR is the flexibility to acquire data in seven different swath positions. One of the ASAR swaths (number 2) corresponds to ERS data coverage and revisit time. This enables harmonization of the ERS 1-2 AMI and the ENVISAT ASAR data. However, it is important to note that ASAR data is not compatible with ERS data for interferometric analysis since the two radar systems use slightly different wavelengths in C-Band.

2.2.3. Geometrical configuration for InSAR

When a point P on the ground is imaged by two radars having different viewing angles, a phase shift occurs between the corresponding range measurements (Figure 2.9). If we ignore the atmospheric differences and different scattering behaviors during two image acquisitions, the observed phase shift for the round trip or the interferometric phase is

$$\Phi = -\frac{4\pi(R_1 - R_2)}{\lambda} = -\frac{4\pi\Delta R}{\lambda} \qquad \textbf{(2.9a)}$$

Due to the 2π phase ambiguity and orbital inaccuracies it is not possible to derive range difference ΔR from the geometry (Hanssen, 2001). However, ΔR can be found by establishing the cosines law between B, R_1 and R_2. Following the approximation 'B, $\Delta R << R_1$' known as "far field" or "parallel-ray" (Zebker & Goldstein, 1986), we obtain

$$\Delta R \approx B\sin(\theta - \alpha_B) \qquad \textbf{(2.9b)}$$

Then we can write Φ in terms of baseline as

$$\Phi = -\frac{4\pi}{\lambda} B\sin(\theta - \alpha_B) \qquad \textbf{(2.9c)}$$

Then the relation between an interferometric phase change Φ and the change in the look angle θ will be

$$\partial\Phi = -\frac{4\pi}{\lambda} B\cos(\theta - \alpha_B)\partial\theta \qquad \textbf{(2.9d)}$$

Height of the satellite h_{sat} above the flat earth is

$$h_{sat} = R_1 \cos\theta \qquad \textbf{(2.9e)}$$

Change in the look angle $\partial\theta$ will correspond to the height of the point P, h_P. So we can express the h_P in terms of the derivative of h_{sat}.

$$\partial h_{sat} = -h_P = -R_1 \sin\theta\, \partial\theta \qquad \textbf{(2.9f)}$$

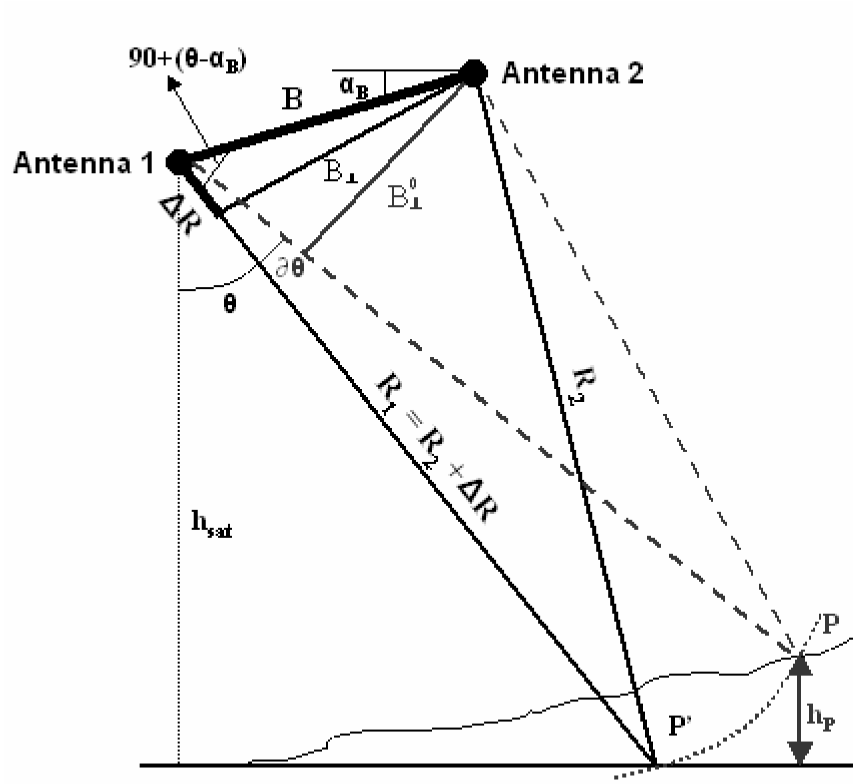

Figure 2.9 : InSAR configuration for topographic heights (adopted from Hanssen 2001) The initial slant range distance R_1 is observed from the round trip of the radar signal. The height of the radar platform h_{sat} and the baseline B (and so its orientation α_B) are estimated from precise satellite orbits. Trigonometric relations between these measurements are used to derive the small angular differences indicated in the figure as perpendicular (or effective) baseline $B_\perp$, range difference ΔR and change in the look angle $\partial\theta$. This basic approach permits the measurement of cumulative angular differences between neighboring resolution cells in an interferogram. It is SAR Interferometry that determines the height h_P of a point P by means of these measurements .

Note that the h_P is the measured height for range resolution cell P, since P and P' are in the same resolution cell and $\partial\Phi$ is the deviation of interferometric phase within the same resolution cell. By combining the equations 2.9d and 2.9e h_P is derived for flat earth geometry,

$$h_P = -\frac{\lambda R_{1P} \sin\theta_P^0}{4\pi B_{\perp,P}^0} \partial\Phi_P \quad \textbf{(2.9g)}$$

The perpendicular baseline $B_{\perp,P}^0$ formed between the ranges towards point P is

$$B_{\perp,P}^0 = B\cos(\theta_P^0 - \alpha_B) \quad \textbf{(2.9h)}$$

The natural range variation across a scene leads to a large gradient of phase across an image. This phase gradient is removed by ''flattening'' the interferogram. In this procedure, an initial value θ_P^0 is given for an arbitrary reference surface (e.g., zero elevation on a spherical Earth) and then a recursive schema is used to find new values for θ_P^0 at this reference surface (Hanssen, 2001). Finally, expected phase produced by the reference surface is subtracted from the original phase. It is the resulting image that consists of fringes following the natural topography.

2.2.4. Properties of interferometric phase

A pixel should conserve its slant range extent in both image acquisitions. Therefore the pixel must not stretch or shrink by more than a fraction of the wavelength from one image to the other (Massonnet & Feigl, 1998). Otherwise, an internal phase contribution is introduced to the pixel that can not be eliminated by the interferometric process. According to the interferometric geometry, the width of the pixel in the (ground) range direction, R_y, corresponds to two different round trip distances, $2R_y\sin\theta_1$ and $2R_y\sin\theta_2$ (Figure 2.10 (a)). So, for interferometry, the difference between these distances should not exceed the radar wavelength. This is the fundamental condition for interferometry (Massonet & Feigl,1998) :

$$2R_y(\sin\theta_1 - \sin\theta_2) < \lambda \quad \textbf{(2.10)}$$

Obviously, this condition restricts the distance between the satellite's orbital trajectories during two passes and causes the "baseline decorrelation" (Figure 2.10 (b)). So, a maximum value of baseline, called "critical baseline" B_c, occurs when the change in the look angle between two passes is sufficient to cause the echoes reflected backscatter from a pixel to become completely independent (Zebker & Villasenor, 1992). Specifically,

$$B_c = \frac{\lambda R}{2R_y \cos \theta} \quad \textbf{(2.11)}$$

It should be noticed from the equation 2.11 that local slope, coarse resolution and short wavelength are the main influences for baseline decorrelation. Orbital cycles of the radar satellites generally meet this condition. For ERS satellites, we find a critical baseline of approximately 1115 m. In practice, ERS pairs having perpendicular baselines less than 1000 m are preferred ($|B\perp| < 1000$ m). Although $B\perp$ applies to a pair of orbits, it has become conventional to calculate a “virtual” value for $B\perp$ with respect to some arbitrary reference trajectory.

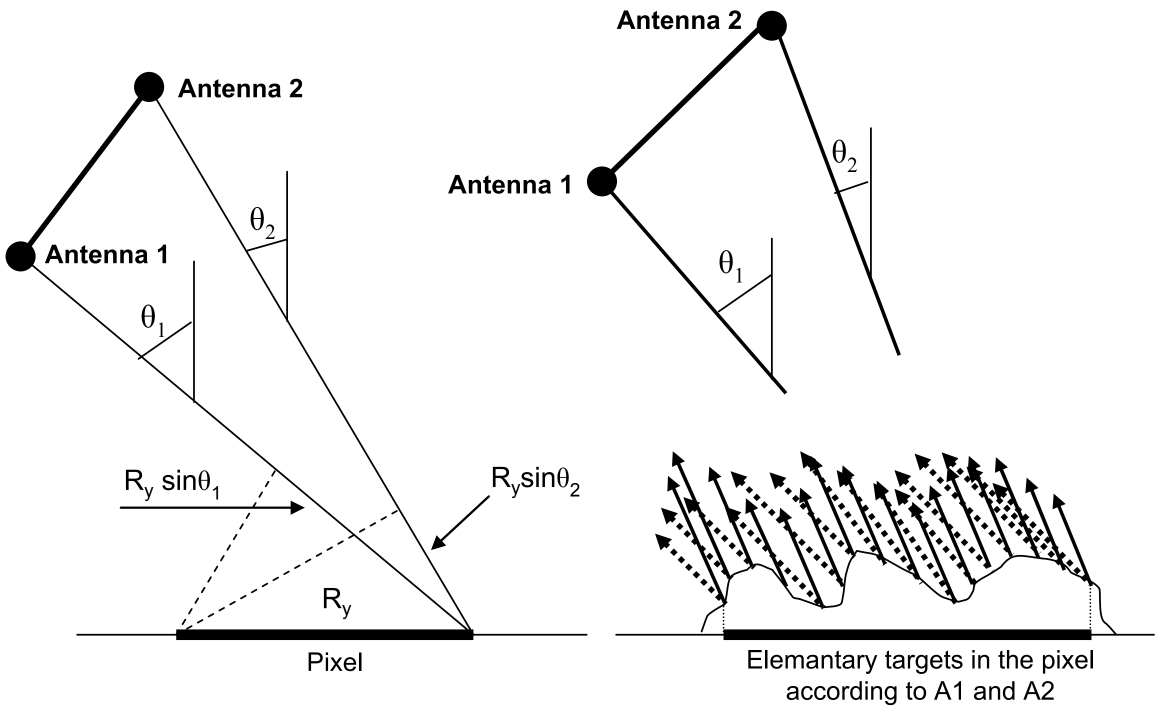

Figure 2.10 : Fundamental condition for interferometry and baseline decorrelation (Li & Goldstein, 1990) a) Antennas 1 and 2 view the same pixel from slightly different look angles. According to this geometry, the pixel corresponds to two different lengths on the slant range. If the difference between these lengths does not exceed the system wavelength λ, a correlation can be obtained. b) Viewing of the antennas from different angles results in a loss of coherence between the two images even when the pixel covers the same area.

For deformation mapping, it is desired to use the image pairs having small separations between orbital trajectories to minimize the orbital contribution to the interferometric phase. However for topographic mapping, there is an ‘optimal’ baseline (Li & Golstein, 1990) giving sufficient phase sensitivity to height measurements.

Five different phenomenon contribute to the interferometric phase difference between two SAR images acquired at distinct times and positions (Massonnet & Feigl, 1998):

$$\phi = \phi_{pix} + \phi_{topo} + \phi_{atm} + \phi_{orb} + \phi_{disp} \quad \textbf{(2.12)}$$

The pixel contribution ϕ_{pix} is the phase due to the response of a resolution cell on earth to the arriving radar pulse. The topographic contribution ϕ_{topo} originates from the stereoscopic characteristic of the interferometry and related to the topographic heights. The atmospheric contribution ϕ_{atm} is the change in the path length of the radar signal due to the instabilities in the atmosphere. The orbital contribution ϕ_{orb} corresponds to difference caused by any shift the satellite orbits. And finally, ϕ_{disp} stands for the phase shift which results from a ground movement along the line of sight. This phenomenon will be discussed in the following paragraphs.

2.2.4.1. Phase variations within a pixel

Scattering from natural terrain is considered as the coherent sum of returns from many individual scatterers within any given resolution cell. This coherent addition of returns from many scatterers causes “speckle”. The relationship between the scattered fields at the interferometric receivers after image formation is then determined by the statistics at each individual receiver, and by the complex correlation function, defined as coherence γ

$$\gamma = \frac{\langle g_1 g_2^* \rangle}{\sqrt{\langle |g_1|^2 \rangle \langle |g_2|^2 \rangle}}, \quad 0 \le \gamma \le 1 \quad \textbf{(2.13)}$$

where g_1 and g_2 represent the SAR return at the antenna, and angular brackets denote averaging over the ensemble of speckle realizations (Rosen et al., 2000).

Within the pixel contribution ϕ_{pix} several sources of decorrelation can be distinguished (adopted from (Hanssen, 2001)):

(a) baseline decorrelation, caused be difference in the incidence angles between the two acquisitions;

(b) Doppler centroid decorrelation, caused by the differences in the Doppler centroids between two acquisitions;

(c) temporal decorrelation, caused by the physical changes in the terrain, affecting the scattering characteristics of the surface;

(d) volume decorrelation, caused by penetration of the radar wave in the scattering medium;

(e) thermal (or system) noise, caused by the characteristics of the system, including gain factors and antenna characteristics;

(f) processing induced decorrelation, which results from the chosen algorithms, e.g., for coregistration and interpolation.

The effects of baseline, Doppler centroid and temporal decorrelation can be avoided to some degree by selecting good pairs of images.

2.2.4.2. Topographic contribution

As the radar observes the terrain in a stereoscopic manner, lines of equal phase in the interferograms appear like elevation contour lines. These fringes are called "topographic fringes". Massonnet & Rabaute (1993) used the expression of "altitude of ambiguity" to quantify the contribution of topography on the interferograms. If the trajectories have a horizontal separation of d, the altitude of ambiguity h_a is

$$h_a = \frac{R_{slave} \ \lambda \ \tan\theta_{master}}{2B_{\perp}} \quad \textbf{(2.14)}$$

where R_{slave} is the range from the slave trajectory to the target, θ_{master} is the angle of incidence for the reference image, and λ is the radar wavelength. Altitude of ambiguity for ERS satellites can range from infinity to ~10 m. In practice, we can use the following approximation for ERS satellites,

$$h_a \approx \frac{10000 m^2}{B_{\perp}} \quad \textbf{(2.15)}$$

Massonnet & Feigl (1998) explains geometric meaning of altitude of ambiguity as the change of elevation which forces the slave range to change by half a wavelength (one-wavelength round trip) with respect to what it would be on the reference. In other words, the altitude of ambiguity is the elevation difference between adjacent fringes in the interferogram after orbital correction.

For geophysical applications, the altitude of ambiguity should be as large as possible because we expect the satellite acquire the two images from exactly the same point. For DEM derivation, the image pairs having small altitude of ambiguity should be selected because these pairs tend to produce more frequent topographic fringes.

2.2.4.3. Satellite orbits

The SAR systems currently in orbit were not specifically designed for interferometry. Therefore, most orbital SAR systems do not have advanced tracking systems providing accurate information on the position and orientation of their platform. However, the orbital separation ("baseline") B and its orientation α should be determined accurately in order to derive (or eliminate) the topographic contribution to interferometric phase. For this purpose, precise orbit data, containing the list of the radars successive positions and velocities, is provided to the ERS users.

The ERS orbital trajectories determined by Delft Technical University have a radial RMS uncertainty of 5-7 cm (Scharroo & Viser, 1998). Another option is to use ERS orbit data calculated by the German National Research Center for Geosciences (GFZ Potsdam) with a radial RMS uncertainty of 8-10 cm (http://www.gfz-potsdam.de/pb1/ERS/GPM/GPM_PRECISEORB.html).

Even after correction using the precise orbit models, interferograms may still contain some residual fringes (2-4 fringes according to the given error budgets). These fringes, so called orbital fringes, sometimes can be recognized by their along-track orientation and parallel nature.

2.2.4.4. Atmospheric perturbations

Phase measurements can be disturbed by mainly two atmospheric effects; "tropospheric turbulence" and "stratification". Troposphere is the atmospheric layer (~15 km above earth) where all weather phenomena originate. One other contamination source is the change in the ionospheric electron density in the atmosphere. The ionosphere is often treated as a spherical shell between 60 and 600 km height with a constant electron density in height, homogeneously varying in time although the electron density is temporally and spatially variable, (Hanssen, 2001). Atmospheric signals on the interferograms have been recognized by Goldstein (1995), Massonnet & Feigl (1995) and Tarayre & Massonnet (1996).

"Tropospheric turbulence" results from the three dimensional refractivity of the radar signal along the range. The refractivity for radar signals is mainly dependent on temperature, pressure and water vapor in the troposphere. It is water vapor that predominantly causes "phase delay" in the interferometric observations. Moreover, turbulent wind can also disperse the radar wave. Since the atmospheric events may vary in wide range of scales, it is very difficult to define the spatial coverage of the artifacts in the interferograms. Because of the heterogeneities in both horizontal and vertical layers of the atmosphere, flat terrain as well as hilly and mountainous terrain is affected by the tropospheric turbulence.

The measure of the phase delay caused by tropospheric turbulence may vary (Figure 2.11). For example, Goldstein (1995) has observed tropospheric time delay error of 0.24 cm on 1-day C-Band interferograms of the Mojave Desert. This is a dry place with stable climate conditions with no deformation and little topographic relief. In another case, Hanssen et al. (1999) have observed a phase delay caused by water vapor that was changing between 1.1 and 6.4 cm over a cold front band of 3 – 5 km in The Netherlands. They have used one day interval C-Band interferograms.

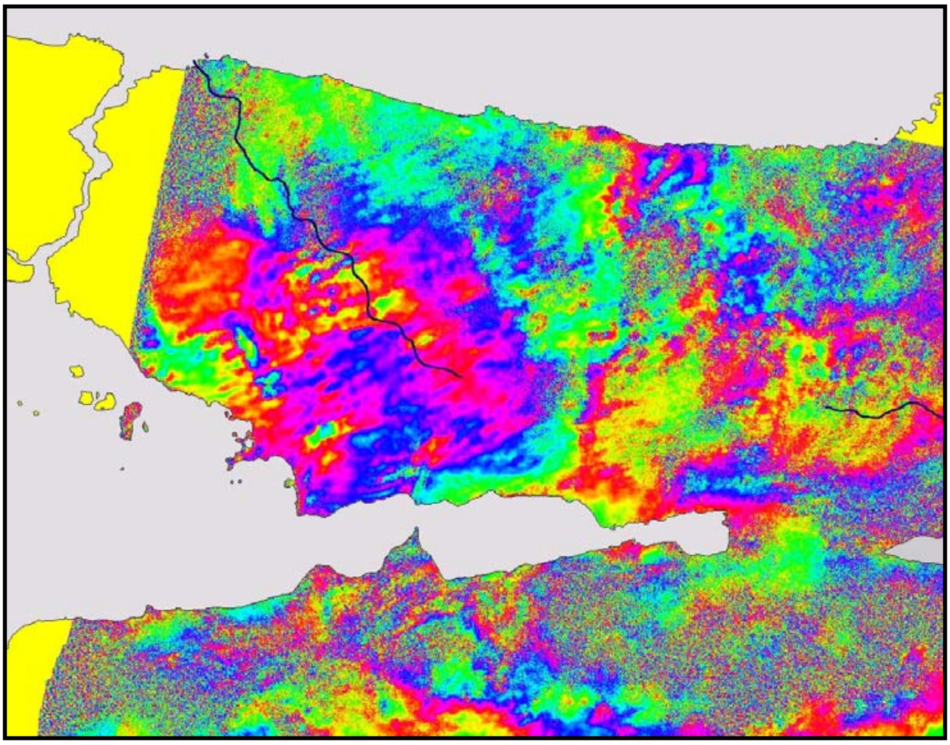

Figure 2.11 : An ERS interferogram severely affected by tropospheric turbulence. Diagonal phase change pattern in the middle of the image indicates atmospheric effect during one of the acquisitions of the ERS images (15 July 1992 or 19 August 1992). One color cycle represents 28 mm range change.

"Stratification" results from the vertical variations of refractivity index in the troposphere. Therefore, the resultant fringes "look like" the topography. They appear on hilly or mountainous terrain. Stratification may cause erroneous interpretation in mapping topography. This phenomenon has been recognized by Beauducel et al. (2000), Tarayre & Massonnet (1996), Massonnet & Feigl (1998) and Delacourt et al., (1988) during the deformation studies of Mt. Etna. Experimental results from radiosondes in the Netherlands show that differential delays can amount to more than 1 cm over height intervals of 500 meters or less (Hanssen, 2001). As a rule of thumb, we consider the worst case to be one C-Band fringe (28 cm) per kilometer of topographic relief. If misinterpreted as topography, one such fringe would create an artifact in the resultant digital elevation model equal to the altitude of ambiguity, or several hundred meters for a typical pair of ERS images. If misinterpreted as deformation, one such fringe would cause a range artifact of 28 mm in the deformation map.

Unlike the tropospheric phase delay, an increase in the electron density in the ionosphere causes "phase advance" in the signal path. This results a decrease in the observed range. Although some examples of ionospheric artifacts have been reported (e.g. Massonnet & Feigl, 1995), they can not be identified very easily. The main difficulty is the limited knowledge about the spatial characteristics of the ionosphere over spatial length scales of less than 100 m (Hanssen, 2001) since the total electron content measurements are provided globally.

There are three important observations that characterize atmospheric signal in the interferogram (adopted from Hanssen, 2001). (a) The relative character of an interferogram does not measure absolute signal delays. (b) Orbital errors can easily cause a nearly linear trend over the whole interferogram. Such trends are usually hard to distinguish from atmospheric signals. (c) The amount of atmospheric signal within a set of interferograms can vary greatly in time and space. Additional data about the climatologic characteristics of the location may be helpful over time intervals of 1 day or more and the two states of the atmosphere appear to be practically uncorrelated. Similarly, differences of more than one C-band fringe can occur over distances of 5 km or less (Feigl et al., 2002).

Since it is not possible to correct for atmospheric errors in a deterministic way, it is important to develop a mathematical model that describes the behavior of the atmospheric delay in interferograms stochastically (Hanssen, 2001). In this context, there are several approaches to discriminate atmospheric perturbations from interferograms. Using meteorological or GPS data to interpret interferograms may require additional measurements (e.g., Williams & Bock, 1997). This is not always practical for differential interferometry that uses interferograms of various time intervals. Massonnet & Feigl (1995) suggest a method "pair-wise logic" that is based on the comparison between different pairs of images spanning different intervals of time. The logical extension of this approach is called temporal adjustment (Feigl et al., 2000). Ferretti et al., (2000a,b) developed a technique, so called "permanent scatterers", which is based on time series analysis of phase measurements to remove the atmospheric contribution. Since one of the objectives of the thesis is to develop and apply these approaches, they will be discussed in more detail below.

2.2.4.5. Contribution of displacements

After removing the other contributions, phase difference measurements may reveal the movement of the ground points along the line of sight of the radar. But the scalar quantity of the phase difference should be reconstructed into orthogonal components (easting, northing, up) so that its geophysical meaning can be understood (e.g., Massonet & Feigl, 1998, Hanssen, 2001, Price & Sandwell, 1998). The vector representation of line of sight displacement is

$$\phi_d = -\hat{s} \cdot \vec{u} \qquad \textbf{(2.16a)}$$

where $\hat{s}$ is the unit vector pointing from the ground to the satellite. The displacement vector $\vec{u}$ with its 3-dimensional components, (Figure 2.12). For a descending right looking satellite, components of the displacement vector become;

$$\phi_d = [\sin\theta\sin\alpha_h, \quad \sin\theta\cos\alpha_h, \quad \cos\theta] \cdot [u_n, \quad u_e, \quad u_u]^T \qquad \textbf{(2.16b)}$$

For the descending ERS case, where the satellite heading α_h = ~188.5° and the look angle $\theta \approx 23°$, we find the components of ϕ_d as;

$$\phi_d = -[0.39, \quad -0.06, \quad 0.92] \cdot [u_n, \quad u_e, \quad u_u]^T \qquad \textbf{(2.16c)}$$

As a result of the steep looking of ERS, θ = ~ 23 °, the satellite is more sensitive to the vertical displacements $(u_u = 0.92)$. Also the combination of ascending and descending orbit interferograms can be used to find the second component of a displacement vector (e.g., Wright et al., 2001).

A model helps determine vector components. For example, assuming purely vertical motion for subsidence leads to

$$\hat{s}_e = \hat{s}_n = 0 \qquad \textbf{(2.16d)}$$

$$\phi_d = -u_u \cos\theta \qquad \textbf{(2.16e)}$$

Accordingly interferometric fringe patterns reveal gradients in the displacement field. For example, a (rigid) tilt , or a rotation of a planar surface about a horizontal axis will create many closely spaced fringes (Peltzer et al., 1994). Similarly, a spin, or rotation about a vertical axis will also create a steep fringe gradient. (Peltzer et al., 1994) If the gradient is too steep, then the phase change will no longer satisfy the fundamental condition of interferometry and the fringes will vanish.

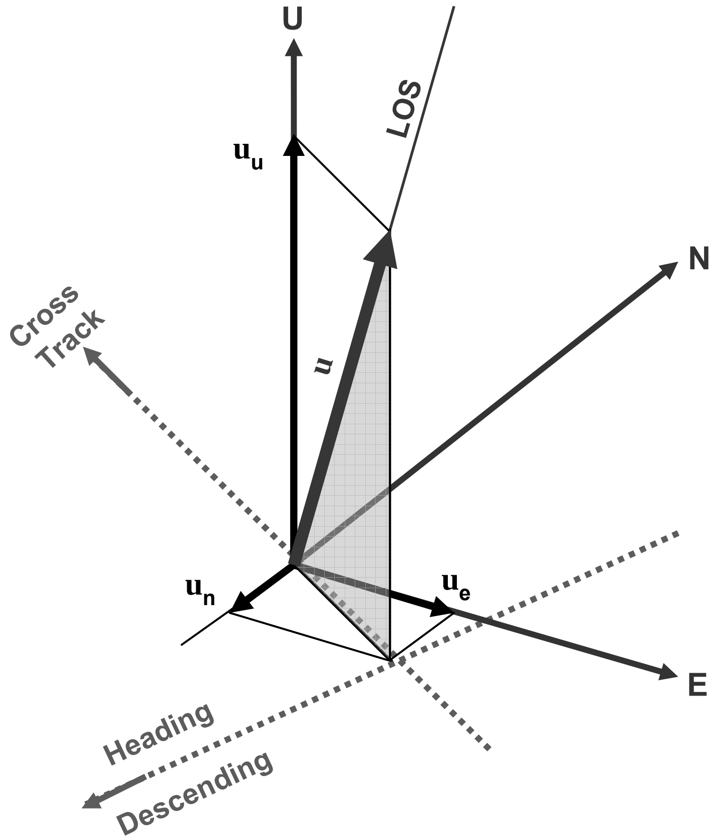

Figure 2.12 : Displacement vector Φ_d along the line of sight of a descending satellite. u_e, u_n and u_u, are the components of Φ_d in North, East and Up directions, respectively. α_h is the azimuth of the satellite heading which is 188.5^o and -8.5^o for descending and ascending orbits, respectively.

2.3. Discrimination of Geophysical Phenomena

To discriminate range changes due to geophysical phenomenon, we need to eliminate topographic contribution from the interferograms. Interferometric applications based on this approach are referred to as "differential interferometry".

There are two ways of separating out the topography. First, interferograms can be produced by subtracting a synthetic fringe pattern calculated with a ready DEM produced by e.g. map digitizing or optical stereoscopy (Massonnet & Feigl, 1995).

DIAPASON InSAR software used in this thesis runs with this principle. Second, an interferogram with no deformation can be used to eliminate the topography. In this case, at least three SAR images are required (e.g., Gabriel et al.,1989; Zebker et al., 1994). The difficulty of finding two coherent SAR images with no deformation and the necessity of unwrapping are the main disadvantages of this approach.

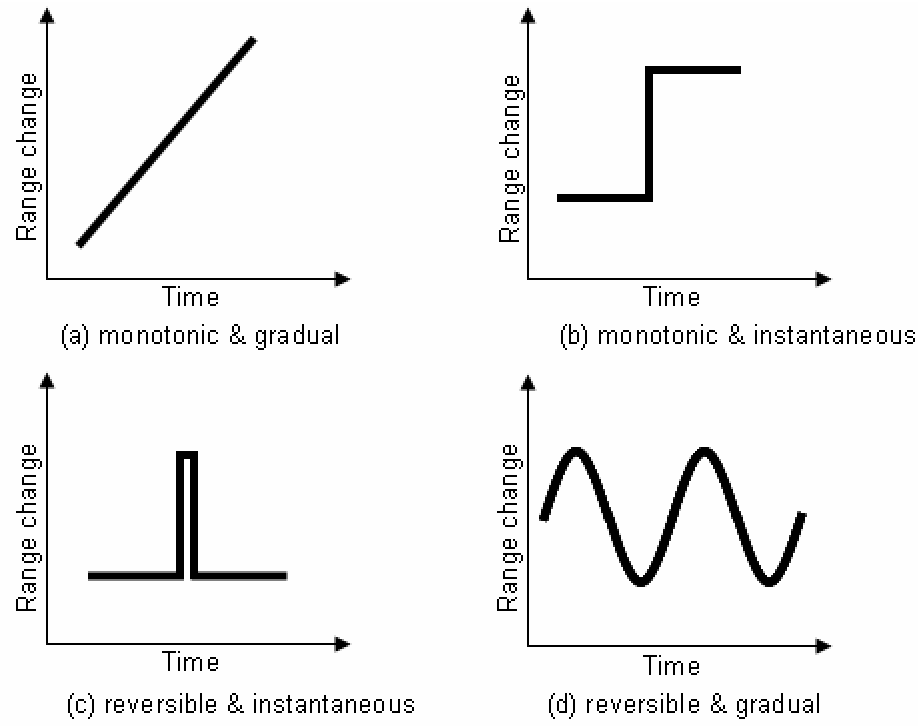

Figure 2.13 : Deformation signatures in time and space.

The geophysical phenomena are classified into four types by their different deformation signatures (Figure 2.13). Similar to the classification of Massonnet & Feigl, 1998, we call them as in the following:

(a)Monotonic and gradual changes (e.g., interseismic strain accumulation and urban subsidence) have a time derivative with the same sign, i.e. always increasing.

(b)Monotonic and instantaneous changes (e.g., co-seismic displacements of an earthquake results permanent) result from rapid changes on the ground and cause permanent displacements.

(c)Reversible and instantaneous changes are single epoch events. The atmospheric signals occurring in daily and hourly intervals may produce artificial fringes similar to deformation signals.

(d)Reversible and gradual changes (e.g., seasonal deformation due to water table changes) are difficult to distinguish. No deformation signal will be observed if the interferogram spans an interval with no change.

The “pair-wise logic” method suggested by Massonnet & Feigl (1995) is useful to validate a deformation signal or to distinguish an atmospheric artefact on the interferograms.

2.4. InSAR Processing by DIAPASON

In this study, the interferometric SAR processing has been realized by DIAPASON (Differential Interferometric Automated Process Applied to Survey of Nature) software, Version 4.0. The software has been developed by the French Space Agency (CNES) and is now distributed by Altamira Information, SL (CNES, 2003, Massonnet, et al., 1994).

The main feature of DIAPASON is to use a pre-existing Digital Elevation Model (DEM) to do differential interferometry (CNES, 1998). The software creates a simulated interferogram from a DEM and subtracts it from the observed interferogram. The resultant “differential” interferogram contains the wrapped phase including all the contributors discussed in the previous section. The advantage of this approach is registration. All three maps (phase, amplitude, coherence) produced by DIAPASON are calculated in exactly the same coordinate system as the DEM. By default, geographic longitude and latitudes in decimal degrees are on a regular grid with square cells (or pixels) each 3 arc seconds on one side. In most cases, the DEM and thus the interferometric products are projected to geographic coordinate system. In other cases, cartographic projections such as Universal Transverse Mercator or Lambert can be used to project and interpolate the wrapped phase values. This approach of DIAPASON is very important especially for interpreting a stack of more than 30 amplitude and phase images in a time series analysis.

In this study presented here, the cell size is ~1.5 arc seconds in both latitude and longitude. Determining the resultant cell size of the interferometric products is important because some InSAR processing parameters depend on it (e.g., multi-looking window size). Accordingly, the default DIAPASON parameters were modified for this study to support DEM cell size and coverage. The details will be described in Chapter 3.

By convention, the two radar acquisitions of an interferometric pair are called “Master” and “Slave”. The orbit having the earlier acquisition date is the Master. DIAPASON processing follows six basic steps (Figure 2.14):

(1) Setting up the data. The “extract” program extracts the auxiliary information from the satellite data from various sources and places it in a standard file called “GEOSAR”. Afterwards, the “concat” program gathers the raw complex radar returns into a single file. The parameters needed for the SAR focusing (e.g., mean Doppler value) are also calculated at this step. Both the Master and the Slave have to be set up.

(2) SAR focusing. At this step, the raw data is transformed to a complex focused image with improved resolution by a program called “prisme”. For the interferometric process, two outputs are generated: A single look complex (SLC) image and an amplitude image averaged by a multi-look window. The focusing process is applied to both the Master and the Slave separately.

(3) Registering the images with the DEM

(3.1) Simulation from DEM. An artificial image is calculated according to the DEM and the imaging geometry (i.e. orbital trajectory) of the Master by a program called “simu_sar”. So all the cells of the DEM are projected to the radar image geometry and the radiometry of all cells is calculated according to the local angle of incidence. Finally, the cells are arranged in order of increasing azimuth and range. In the latter step, the calculated radiometry is averaged according to the given multi-look window size.

(3.2.) Rough correlation between the Master and the simulated image. The simulation and the multi-looked Master are geometrically similar except for the inaccuracies due to the proximal (“near range”) distance r_0 and the start time of the acquisition t_0. These two parameters, are coordinates of the first pixel in the range and azimuth directions, respectively. DIAPASON applies a series of correlations, by a program called “correl”, to measure the level of geometric similarity between the two images and then estimates the shifts in range and azimuth (time). These two shifts, measured to sub-pixel accuracy, are used for the precise setting of the Master. The program called “correct_stnr” (“cormoy”, in the older version) uses the shift in the azimuth to estimate the precise start time of the acquisition and the shift in the range coordinate to estimate the precise proximal distance in the range coordinate.

(3.3.) Superpositioning of the Slave according to the Master. The superpositioning of two images requires large scale correction such as start time of the acquisitions, the proximal distance, the difference in the number of points covering the images but also small scale (several dozen pixels) corrections related to the stereoscopic effect created by the relative position (baseline) vector separating the two orbital trajectories. In this step, DIAPASON performs a second correlation as performed between the Master and the simulated DEM. In this case, the “correl” module precisely estimates the two offset parameters, between the Master and the Slave, Δr and Δt in range and azimuth, respectively for each correlation cell, including several hundred SLC pixels. Correlation cells are larger than the DEM cells. The two-dimensional correlation procedure estimates two components of the horizontal “lag” vectors as well as the correlation coefficient. From the ensembles of these estimates; the program called “geo_grid” (“grillegeo” in the older version) forms “distortion grids” in both range and azimuth. These grids are subsequently modeled as piece-wise bilinear surfaces. Each of surfaces can be thought of as a patchwork quilt where the function, range offset Δr and azimuth offset Δt, depends only on position in the range and azimuth coordinate system. Actually, this process of measuring offsets and smoothing them into grids is performed twice, once between the Master image and its simulation (from DEM and orbits) as well as between the Master and the Slave images. Once the transformation is determined (as distortion grids), it is applied to the Master geometry. Then the Slave image is resampled into the Master geometry as a new single look complex image by a program called “change_geo”.

(4) Interferogram generation. A raw complex interferogram is calculated between the Master and the Slave. The differential interferogram is generated after the theoretical phase for each cell of the DEM is subtracted from the raw phase difference between the Master and the Slave. These two steps are realized by a single program called “interf_mnt”. Generally, interferograms are averaged according to a multi-look window.

(5) Correcting orbital efects. In some cases, the orbital trajectories may not be sufficiently to accurate model the orbital contribution to the phase. The “fringe_gradient” program estimates the average gradients of the interferometric phase in the range and azimuth directions. Then the “clean_fringe” program removes the linear orbital phase ramp from the interferograms.

(6) Filtering. Interferograms are smoothed to be easier to interpret. At this step, the “ps_filt2” program performs a power spectral filtering (Goldstein & Werner, 1998).

Correcting the orbital phase ramps and filtering can be applied to the phase of the differential interferogram separately. Briefly, the simple phase image “pha” can be either corrected or filtered to create an alternative set of different phase images. By convention, file name prefixes used to designate these phase images; “psp”, “cln” and “smp” (Table 2.4).

Table 2.4 : The phase images produced by DIAPASON.

		Linear orbital phase ramp correction: NO	Linear orbital phase ramp correction: YES
Power spectral filtering	NO	pha	cln
	YES	psp	smp

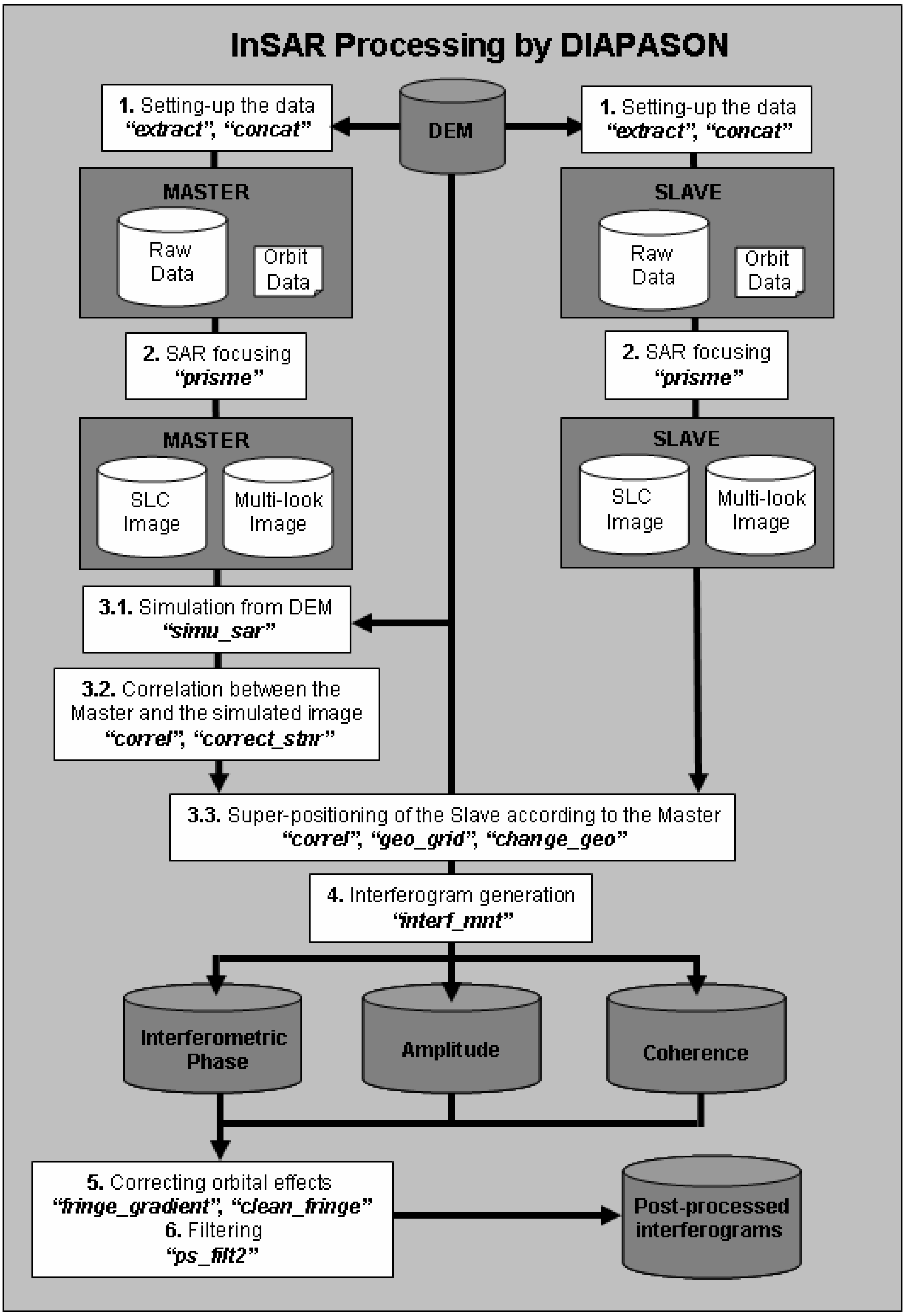

Figure 2.14 : InSAR processing by DIAPASON.

In DIAPASON, the six processing steps are combined in the DTOOLS suite of shell scripts developed by Kurt Feigl and his students (beginning with Gasperi, 1999). Three main shell scripts in DTOOLS that simplify the processing are "setup_image", "create_diapason_files" and "calculate_interferogram".

At the end of the process, three basic products are generated by DIAPASON; phase, amplitude and coherence maps.

2.5. Measuring Slow Motion Ground Deformation

While conventional InSAR has been proven to be a very effective technique to measure ground deformation, its applicability is limited mainly by radar signal correlation and atmospheric effects. Therefore, to measure slow motion deformation occurring over long times requires a challenging effort if conventional InSAR techniques are to be used.

If one of the scatterers contributing to the pixel is much more stable than the others, then its contribution to the phase and amplitude measurements will dominate those from the other scatterers. If we can identify these pixels represented by a single strong scattarer, then we can simplify the process of interpreting the interferogram. These persistent or permanent scatterers (hence called “PS pixels”) are more reliable because they are less susceptible to all processes causing decorrelation. Accordingly, they have less noise then other pixels. Once the data set has been reduced in size by several orders of magnitude by selecting only the reliable PS pixels in the interferograms, the subsequent interpretation and analysis involving unwrapping and modeling are considerably simpler.

Identifying the PS pixels is the “tricky” part of the methodology. Several approaches have been proposed, as discussed below (e.g., Hanssen & Usai, 1997, Ferretti et al., 2000, 2001; Colesanti et al., 2003a, 2003b; Lyons & Sandwell, 2003, Hooper et al., 2004; Hooper, 2006)

2.5.1. Spatial coherence

Geographic features that are resistant to temporal decorrelation are not likely to change their structure or composition much in the course of time (Usai, 2000). But this attribute still does not help us predict their locations. Generally, man-made features have stronger backscattering characteristics than natural features because of the corner reflector effect. In urban areas, the location and the direction of man-made features (e.g., dihedral buildings, outcrops of bare rock, roads, bridges and walls) reflect most of the radar signal back to the antenna aboard the satellite. Therefore, phase images of urbanized areas tend to correlate better over several years than rural areas.

Studies about the interferometric characteristics of man-made features show that phase of high coherent pixels can remain stable over 3-4 years with a standard deviation of less than 0.25 cycle of C-band phase (e.g. Usai & Klees, 1999, Usai, 2000). In this respect, coherence maps can be exploited to identify points with stable phase.

Hanssen & Usai (1997) suggest that point targets having coherence above a selected threshold may be used to analyze slow deformation processes. However, there are several constraints to their approach. First, coherence depends on the time interval between the two image acquisition epochs.

A high coherence value over 1 or 35 days does not necessarily imply stability over long time intervals. Similarly, large orbital separations or differences in doppler can cause a low coherence for a given point target even it can remain as a strong reflector over years. By choosing sets of image pairs to minimize three variables, time interval, orbital separation and Doppler centroid difference, we can work around this constraints. But deciding the coherence threshold and the coherence estimation window is more problematic.

If we increase the size of the coherence estimation window, overall coherence decreases. As shown in Hanssen & Usai, 1997, this increases the discrimination between areas of different coherence. However, the choice of a multi-looking window equal in size to the estimation window reduces the statistical correlation only to the adjacent multi-looked pixels (Usai & Klees, 1999). This is because multi-looking uses an averaging window while the coherence estimation is performed with a shifting window.

2.5.2. Persistent scatterers

If many (>30) SAR epochs are available, the variation of the amplitude value of each pixel over time can help identify PS pixels. The basic idea is that the amplitude of a stable pixel varies little over time. By analyzing time series of superimposed amplitude images, we can measure this variability. It is called "the amplitude dispersion index" and denoted "D_A" by Ferretti et al. (2001). It is called "scattering amplitude" and denoted "s" by Lyons & Sandwell (2003).

Ferretti et al. (2001) explain the relationship between the phase stability and amplitude as in the following. A stable scatterer is characterized by a complex reflectivity g and circular Gaussian noise n. Real and imaginary components of noise, n_R and n_I of have Gaussian distribution that is characterized by zero mean and standard deviation σ_n. Then SNR becomes g/σ_n. See Figure 2.16 for the graphical representation.

At high SNR (>4), the distribution of the amplitude values approaches a Gaussian distribution. For very high SNR values, standard deviation of phase σ_v can be estimated from amplitude dispersion;

$$\sigma_v \approx \frac{\sigma_{n_I}}{g} \approx \frac{\sigma_A}{m_A} \approx D_A \qquad \textbf{(2.17)}$$

where m_A and σ_A are the mean and the standard deviation of the amplitude values of a single pixel (Figure 2.15). Ferretti et al., 2001 defines this ratio as "amplitude dispersion index" D_A. For large values of SNR, D_A becomes the measure of phase stability. Finally, a threshold can be set to identify pixels with small D_A values.

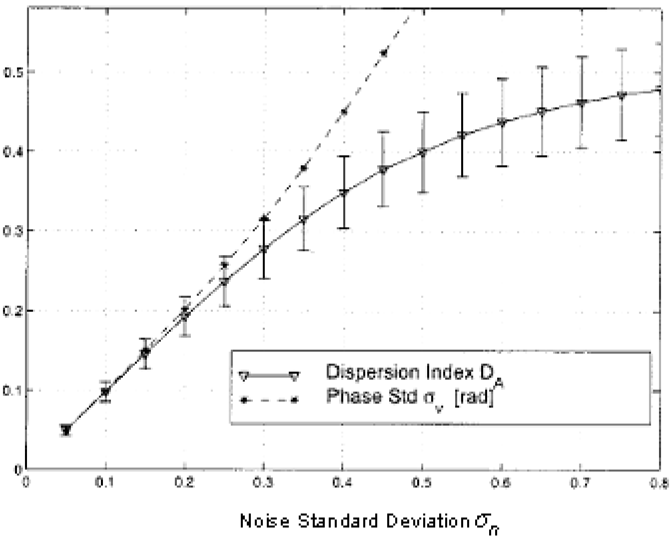

Figure 2.15 : Amplitude dispersion numerical simulation results of Ferretti et al. (2001). They set the value of g to 1 while they incremented the noise standard deviation σ_n gradually from 0.05 to 0.8. For each value of σ_n, they estimated 5000 D_A and σ_v from 34 scenes. Mean D_A and σ_v were plotted for each σ_n. Notice that small values of D_A (D_A < 0.25) correspond to low σ_v.

It is important to note that a radiometric calibration has to be applied to the multi-temporal SAR data set before the statistical analysis of the amplitudes. Several methods exist for calibration. An algorithm using the calibration factor specified by ESA can be applied to the data set for absolute calibration (Laur et al., 1998; Adam et al., 2003). Relative calibration methods can also be performed. (Bovenga et al., 2002, Lyons & Sandwell, 2003). In this study, the relative calibration proposed by Lyons & Sandwell (2003) is applied.

Even though PS technique can not find all the buildings in cities, PS density can be very high in urban areas. Experimental results of Colesanti et al., 2003a have shown that PS density can lead to 125-400 PS / km^2 in urban areas and 15-50 PS / km^2 in rural areas (1 km^2 = 50 [range] x 250 [azimuth] = 12500 pixels). Actually, it is not easy to provide general figures for rural areas. As for the natural surfaces where PSs mostly correspond to bare rocks, a PS density of 200 PS / km^2 is possible. Colesanti et al., 2003a suggest a minimum PS density of 3-4 PS / km^2. Table 2.5 gives the various preferences for PS selection from various studies.

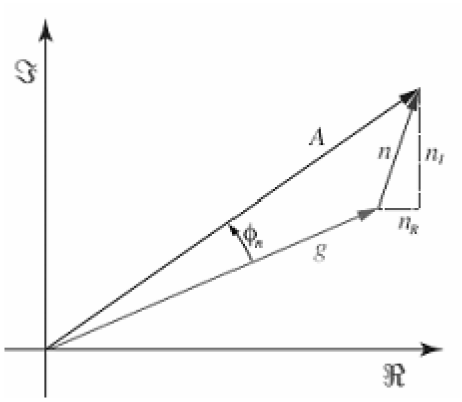

Figure 2.16 : The relationship between signal g, noise n, amplitude A, and phase noise σ_v for a single pixel in a single pixel (from Hooper, 2006). n_R and n_I are the real and imaginary parts of the noise.

Since a PS is a dominant scatterer within the pixel, the pixel resolution should be as high as possible to identify that dominant scatterer and to provide the suggested PS densities. However, achieving fine resolution radar images may not always be possible because of image registration issues. In this case, it may be more general to quantify the number of PS pixels as a fraction of the image.

PS pixels are characterized by low phase standard deviation. Therefore, analyzing the PS candidates for their phase standard deviation is another critical step. Colesanti et al. (2003a) estimate standard deviation of phase σ_v on a pixel by pixel basis directly from coherence $|\gamma|$. They calculate the "single pixel coherence" $|\gamma|$ from a set of interferograms.

$$\gamma = \frac{1}{N}\sum_{i=1}^{N} e^{jv_{x,y,i}} \quad \textbf{(2.18a)}$$

$$\gamma = \frac{1}{N}\sum_{i=1}^{N} \cos(v_{x,y,i}) + j\frac{1}{N}\sum_{i=1}^{N} \sin(v_{x,y,i}) \quad \textbf{(2.18b)}$$

$$\gamma = \gamma_R + j\gamma_I \quad \textbf{(2.18c)}$$

where v is the phase, x, y are indices denoting the image pixel in the i^{th} interferogram of N interferograms. γ_R and γ_I are the real and imaginary parts of the complex random variable γ.

Phase residuals of PS pixels are expected to have a standard deviation much below one radian. Accordingly, Colesanti et al. (2003a) suggest that $\sigma_v \leq 0.6$ radian (2.7 mm along LOS) should be used for PS selection. They estimate the σ_v directly from the measured $|\gamma|$

$$\sigma_v \simeq \frac{\lambda}{4\pi}\sqrt{-2\ln|\gamma|} \quad \textbf{(2.19)}$$

Coherence values $|\gamma|$ = 0.8, 0.9, 0.95 and 0.975 correspond to estimated σ_v = 3, 2, 1.4 and 1 mm, respectively.

Table 2.5 : Major PS InSAR studies and their preferences for PS selection

Study area / Deformation process	**Reference**	**PS criteria**	**PS density**
Pomona, CA (USA) Urban subsidence (16 x 20 km)	Ferretti et al., 2000	$\|\gamma\| > 0.75$	~ 3 PS / km^2
Ancona (Italy) *Landslides (5 x 4 km)*	Ferretti et al., 2001	$\|\gamma\| > 0.75$, $D_A < 0.25$	1% of image pixels
Los Angeles Basin, CA (USA) *Various processes* *(60 x 60 km)*	Colesanti et al., 2003a	Amplitude Stability Index: 2.5 – 3	150 PS / km^2
Fremond City, CA (USA) *Tectonic process* *(6 x 3 km)*	Colesanti et al., 2003b	$\|\gamma\| > 0.8$	170 PS / km^2
San Jose City, CA (USA) *Seasonal subsidence* *Tectonic processes* *(18 x 11 km)*		$\|\gamma\| > 0.8$	230 PS / km^2
Long Valley Caldera, CA (USA) *Volcanic process* *(20 x 15 km)*	Hooper et al., 2004	$D_A < 0.4$ Selection based on PDF of $\|\gamma\|$	44 PS / km^2 ~ 10% of image pixels
Volcan Alcedo (Galapagos) *Volcanic process* *(40 x 40 km)*	Hooper, 2006	$\sigma_v \leq 0.6$ Selection based on PDF of PS	> 3 PS / km^2
Ranafjord (Norway) *Various processes* *(80 x 60 km)*	Dehls et al., 2002		75 PS / km^2 250-300 PS / km^2 (max)

2.5.3. Temporal adjustment

A set of interferograms is combined to reveal a time series of phase measurements describing the spatial and temporal evolution of deformation. The method corrects the phase measurements by using the redundant information in a set of interferograms spanning different time intervals.

Temporal adjustment was proposed by Beauducel et al. (2000). The same approach was applied to Hengill Volcano by Feigl et al. (2000). As Beauducel et al. (2000) summary in their study; interferometric data sets can be compensated as a geodetic network would be compensated. So, a set of interferograms can be defined in terms of m observations, n known and covariance V. If $m > n$, then we can write the undetermined linear system;

$$Ax = b + E \quad \textbf{(2.20a)}$$

A is the m-by-n dimensional design matrix. It consists of 1, -1 and 0. Each 1 and –1 represent the interferograms as master and slave, respectively. x is the n dimensional vector of unknown parameters. It contains the unique epochs of the interferometric data set. b is the m dimensional vector of observations that contains phase differences. E is the residual vector. The solution of the linear system is

$$x = (A^T V^{-1} A)^{-1}\ A^T V^{-1} b \quad \textbf{(2.20b)}$$

and the uncertainties of the solution is

$$\Delta x = \sqrt{\frac{(A^T V^{-1} A)^{-1} b^T (V^{-1} - V^{-1} A (A^T V^{-1} A) A^T V^{-1}) b}{m - n}} \quad \textbf{(2.20c)}$$

As described by these authors, temporal adjustment applies to any parameter which describes the data as a linear function. Accordingly, this approach is applied to interferograms having orbital separation values $B\perp$ with respect to a “virtual” orbit. We call such group of interferograms “specie”. An example of species plot is shown in further sections.

Temporal adjustment of interferometric data sets requires unwrapping the phase data. Recently, Feigl and Thurber (2007) have extended the approach to include wrapped (nonlinear) phase observations. In this thesis, Feigl and Thurber’s (2007) approach is applied to reveal urban subsidence around Istanbul metropolitan area.

3. GROUND MOTION IN THE AVCILAR DISTRICT OF İSTANBUL

3.1. Introduction

Avcılar vicinity of İstanbul is selected for ground motion analysis. All the displacement measurements are based on ERS radar images acquired between 1992 and 1999.

Avcılar is located between Küçükçekmece and Büyükçekmece counties of İstanbul. The major reasons for analyzing the ground deformation in the vicinity of Avcılar are as follows:

(a) Avcılar county of İstanbul was severely affected from the 1999 Izmit Earthquake although the town was located 125 km away from the epicenter of the earthquake.

(b) The region between Büyükçekmece and Avcılar has been suffering from landslides for many years. The landslides are mostly occurring on the slopes facing the coast.

(c) The region between Büyükçekmece and Avcılar is one of the fastest developing areas of İstanbul.

(d) The region is surrounded by two lagoons, in the west Küçükçekmece Lake and in the Büyükçekmece Lake. Lagoon environments can cause variations on the ground water table.

(e) The ground motion map presented by GMES - Terrafirma shows “hot spots” in this region subsiding by an annual rate of greater than 5 mm/yr.

3.2. Avcılar District

Avcılar is located 25 km west of İstanbul. The city center of Avcılar is situated at the triangular area between the Küçükçekmece Lake and the Marmara Sea (Figure 3.1). The Küçükçekmece Lake is a lagoon lake with a connection to the Marmara Sea in the east. The main residential area of Avcılar is on a NW-SE elongated hill that rises to 135 m from the shores of the Küçükçekmece Lake and the Marmara Sea.

Avcılar, having 6% an annual rate of population growth between 1990 and 2000, is one of the fastest developing areas of İstanbul. The town had at least 230 thousand habitants in 2000 (TUIK, 2000). There is also a great deal of industrial development at the vicinity. Some agricultural areas still exist at the north-west of the Küçükçekmece Lake.

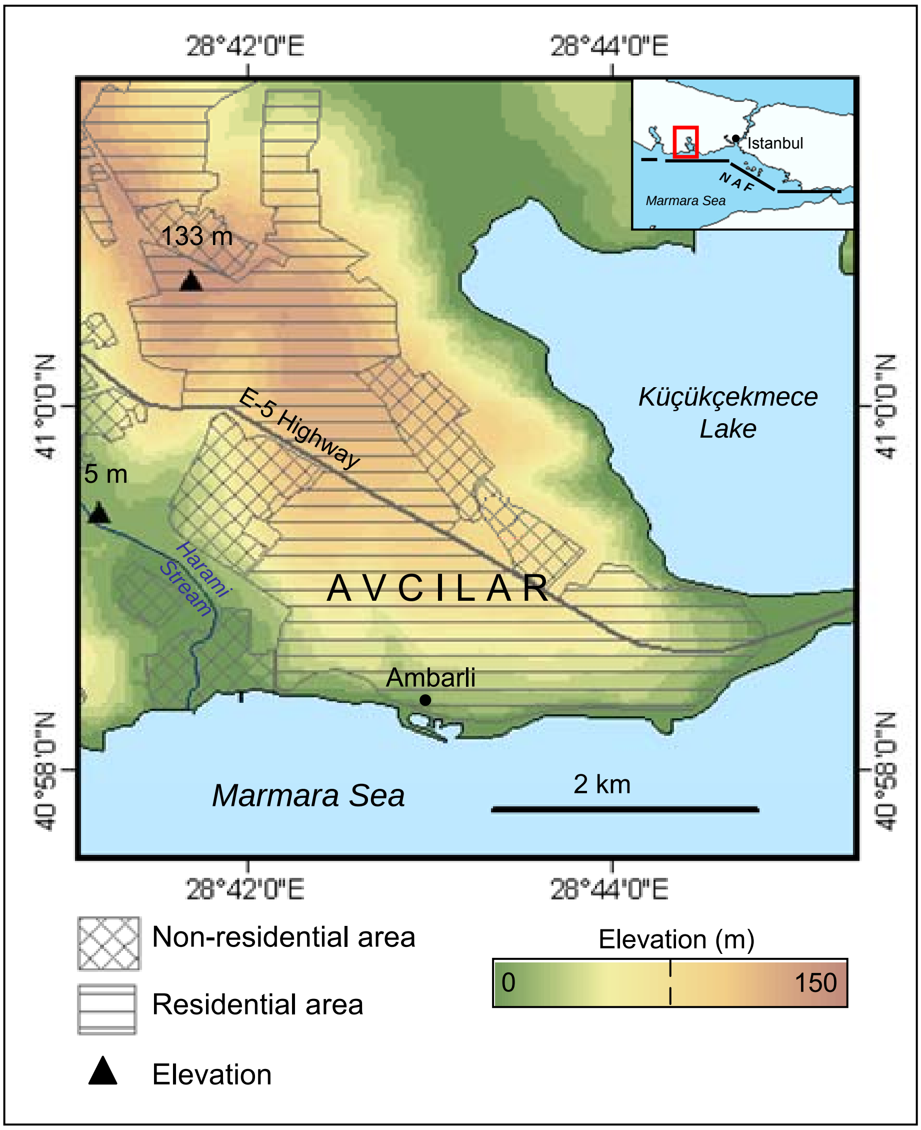

Figure 3.1 : Map of the Avcılar district showing urbanized areas, and the E-5 highway (dark gray) on topographic data (JICA-IMM, 2002). Most of the buildings damaged in the 1999 earthquake are located between the highway and the coastline (Tezcan et al., 2002). Inset shows the trace of the North Anatolian Fault and the outline of the study area (red frame).

3.2.1. Geological features

There are three main geologic formations in the vicinity of Avcılar; Bakırköy, Çukurçeşme and Gürpınar. (The map showing these geological formations is shown in Figure 3.24). The descriptions of these formations are given in detail in elsewhere (Duman et al., 2004) and summarized in various studies, e.g., by Tezcan et al. (2002), Ergin et al. (2004), Duman et al. (2005a) and Duman et al. (2005b). Bakırköy formation (of late Miocene age) is composed of limestone, clayey limestone and clay. Ergin et al. (2004) describe the Çukurçeşme formation (of

Miocene age) as weakly consolidated or unconsolidated sand and gravel with localized clay or silt lenses and the Gürpınar formation (of Oligocene age) as clay and siltstone. In the urbanized section of Avcılar, depth to ground water table varies between 6 and 16 m Tezcan et al. (2002). Some inactive faults are found in the area. The closest one is the Yeşilbayır Fault elongated in NW-SE direction and is located 5km out of the study area.

Based on the geological and geotechnical investigations of the soil conditions under the urbanized section of Avcılar, Tezcan et al. (2002) present eight different soil profiles. These profiles show that the soil under Avcılar consists of Güngören (0-10 m thick, a member of Bakırköy formation consisting of clay), Bakırköy (7.5-15 m), Güngören (4-15 m thick), Çukurçeşme (15 m thick) and Gürpınar (300 m) formations, respectively. Tezcan et al. (2002) notes the existence of 15 m thick Çukurçeşme formation composed of fine dense sand and recommends a proper liquefaction hazard analysis for Avcılar, especially where the unconsolidated and partially saturated formation is less than 12–15 m below the surface.

The Avcılar area has been severely affected by landslides for many years. There have been some efforts to map and classify the landslides in the area, e.g., by Örmeci (1972) and Duman et al. (2004). The recent studies focused on the landslide susceptibility in the regional scale, e.g., Duman et al., 2005a, Duman et al., 2005b and Alparslan et al., 2006.

As Örmeci (1972) and Duman et al. (2004) explain, the landslides are located in the lithologies composed of permeable sandstone layers overlying impermeable claystone, siltstone or mudstone layers (The map showing these geological formations is shown in Figure 3.24). During the wet season, while the water passes through the fissures of the upper permeable layer, it increases the pore pressure and weakens the soil. When the water reaches the impermeable layer, it flows along the interfaces of the two layers. The Çukurçeşme and Gürpınar geological formations have soil characteristics that are typical for this kind of landslide.

Landslides, known for years, have not been a great treat to urban life in Avcılar until some movements in Ambarlı residential area were reported to İstanbul Metropolitan Municipality in 2004. One year after the incident, municipality decided to evacuate 57 blocks of buildings in the region (~0.5 km^2) and to start a project to analyze the landslides by geophysical and geological methods (ELC, 2005, Ergintav, 2006). To analyze the displacement of landslides on Ambarlı Port (SW end of the study area), Kalkan et al. (2003) conducted a project based on a network of GPS surveys and terrestrial measurements. They measured a maximum displacement of 29 cm at vertical and 130 cm at horizontal at Ambarlı Port area between the years 1999 and 2003.

3.2.2. Damage during the 1999 İzmit Earthquake

Avcılar county of İstanbul was severely affected by the 1999 İzmit Earthquake. At least 250 people were killed and 1450 buildings damaged during the earthquake. Some 11% of the buildings were either totally collapsed or heavily damaged beyond repair (Tezcan et al., 2002). Surprisingly, the damage in Avcılar County was much greater than in the whole metropolitan of İstanbul. Avcılar is located 25 km west of İstanbul downtown and 120 km from the epicenter of the earthquake.

Recent studies (i.e., Tezcan et al. (2002), Ergin et al. (2004)) explained the severe damage in Avcılar by “site amplification”, a ground shaking phenomenon that occurs when the soft soils or rocks overlying hard bedrocks amplify seismic waves. This causes amplified levels of ground shaking that is higher than other sites at the same distance from the fault rupture. Field et al. (2001) summarized the two main geologic factors that cause site amplification as (1) the softness of the rock or soil near the surface and (2) the thickness of the sediments above hard bedrock. Surprisingly, no damage associated with landslides was reported after the earthquake.

Based on the affects of various large earthquakes on some sites of Avcılar, Ergin et al., (2004) suggested that “trapping” of body waves and subsequent resonance was the primary cause of the amplification in Avcılar. Tezcan et al. (2002) conducted a wave amplification study on different types of soils underlying Avcılar.

After the 1999 İzmit Earthquake, numerous studies were conducted to understand the extent of damage on the buildings. Besides the site and the building response, “improper building practices” was obviously another reason for the damage. This subject is beyond the scope of this thesis. But for Avcılar, Çağatay (2005) noted that common usage of sea sand in the constructions was also one of the causes of damage in Avcılar.

3.3. SAR Data Set for Interferometry

3.3.1. SAR acquisitions

The ERS frame analyzed in this study covers a portion of the North Anatolian Fault zone and the metropolitan area of İstanbul. The frame title is Track 336 / Frame 2783 and will be called T336/F2783 in the next sections.

Table 3.1 : SAR acquisitions of ERS T336/F2783.

ORBIT	DATE	ERS
3988	1992-APR-20	1
4489	1992-MAY-25	1
6994	1992-NOV-16	1
7996	1993-JAN-25	1
8998	1993-APR-05	1
10000	1993-JUN-14	1
11002	1993-AUG-23	1
12004	1993-NOV-01	1
19362	1995-MAR-29	1
19863	1995-MAY-03	1
20364	1995-JUN-07	1
20865	1995-JUL-12	1
1192	1995-JUL-13	2
21366	1995-AUG-16	1
1693	1995-AUG-17	2
21867	1995-SEP-20	1
2194	1995-SEP-21	2
22368	1995-OCT-25	1
2695	1995-OCT-26	2
23370	1996-JAN-03	1
3697	1996-JAN-04	2
4699	1996-MAR-14	2
25374	1996-MAY-22	1
6703	1996-AUG-01	2

ORBIT	DATE	ERS
7204	1996-SEP-05	2
10711	1997-MAY-08	2
18226	1998-OCT-15	2
19228	1998-DEC-24	2
20230	1999-MAR-04	2
42408	1999-AUG-25	1
22735	1999-AUG-26	2
42909	1999-SEP-29	1
23236	1999-SEP-30	2
43410	1999-NOV-03	1
23737	1999-NOV-04	2
25741	2000-MAR-23	2
26242	2000-APR-27	2
26743	2000-JUN-01	2
27244	2000-JUL-06	2
28246	2000-SEP-14	2
28747	2000-OCT-19	2
29248	2000-NOV-23	2
29749	2000-DEC-28	2
31753	2001-MAY-17	2
34759	2001-DEC-13	2
35260	2002-JAN-17	2
37765	2002-JUL-11	2
39268	2002-OCT-24	2

Four basic criteria were considered while selecting the ERS scenes.

(a) The orbital track that provided as many epochs as possible from the same frame was preferred. Ferretti et al. (2001) suggest ~30 SAR images for PS selection. Only the descending orbital passes could satisfy this criterion.

(b) The data set should span a long duration of time and include the 1999 earthquakes. A large data set spanning the 1999 earthquakes allows us to find PS pixels that remained unchanged during the earthquake shaking. But the number of epochs should provide a sufficient number of image pairs to analyze the ground deformation before the earthquake.

(c) Seasons were not considered during the selection.

(d) ERS-2 scenes acquired after the satellite lost two of its three gyroscopes in February 2000 were excluded from the data set. The Doppler centroid values of the selected scenes were examined from the dedicated web site of ESA (see section 2.2.2.) and found to be within 0.2 PRF of nominal.

Consequently, a total of 48 descending ERS-1/2 epochs were available from the ESA archive. The data set covers a period of 10 years between 1992 and 2002 (Table 3.1).

3.3.2. Digital elevation models

Three different digital elevation models (DEM) have been used in this study:

1) For the conventional interferometric analysis that covered the whole ERS 1/2 SAR frame, I used a DEM derived from the Shuttle Radar Topography Mission (SRTM). SRTM is a global digital topographic data set that has been produced by a radar interferometry mission called "Shuttle Radar Topography Mission". In this DEM, the elevation is posted every 3 arc seconds in geographic latitude and longitude. This posting leads to pixels that are approximately 90 m x 90 m on the ground. The horizontal position of each pixel is accurate to within 20 m (Rodriguez et al. 2005). The vertical accuracy of each height value is specified to be 16 m (Rodriguez et al. 2005). For interferograms with ambiguity heights less than 100 m, uncertainties in the SRTM DEM would contribute 20m/100m or 0.2 cycles of error to the interferometric phase. Interpreted as deformation, this artifact would be equivalent to a 6 mm mistake in range. Some pixels in the DEM are missing height values because of the steep topographic slopes and atmospheric conditions that had influenced the radar mission. These gaps have been filled by interpolation.

2) A digital elevation data set with 10 m posting and a vertical accuracy of ±5 m is used (JICA and IMM, 2002).

3) A digital elevation data produced from SPOT stereo pairs have also been used. This data, referenced to UTM projection Zone 36 with an ellipsoid reference of WGS 84 has a posting of 10 m x 10 m.

Finally, a DEM mosaic was formed in a GIS environment by combining the three different patches. Then the DEM mosaic was resampled onto a grid with a posting of ~1.5 arc seconds or approximately 40 m on the ground.

3.3.3. Satellite orbits

Delft estimates of the ERS satellite orbits were preferred in the data analysis because of their relatively better radial errors (see section 2.2.4.3) than DLR's. For the orbits that did not exist in the Delft archive, (such as the special missions performed by ERS-1 after the 1999 Kocaeli Earthquake), DLR's estimates were useful.

3.4. Radar Data Analysis

The main interferometric analysis of the ERS 1/2 T336/F2783 data set consisted of two different steps. First, the amplitude images were calculated individually one epoch at a time. Seconds, the phase change images (interferograms) were calculated pair-wise, taking one epoch as Master and another as Slave. Images consisted of 4000x3000 pixels in northing and easting directions, respectively. Geographical coverage of the T336/F2783 is shown in Figure 3.2.

The primary considerations in determining the parameters of the interferometric data analysis are:

(1) It is important to obtain geo-coded amplitudes and interferograms. To achieve this, DIAPASON applies a series of correlations between the SAR images and a simulated radar image obtained by the DEM. As a result of the correlations, DIAPASON shifts the interferometric images in range and azimuth according to the DEM geometry. This step requires a larger frame than the study area. Considering this processing philosophy of DIAPASON, all the amplitude images and interferograms were calculated in this full data frame. Accordingly, they are also automatically geocoded (projected) onto the DEM.

(2) To select the persistent scatterers, amplitude images should be created without averaging, using the full resolution of the SAR image. However, it is not always possible or practical to correlate the (noisy) single-look complex images with the simulated radar image. Accordingly, the complex images are focused using averaging in azimuth. Averaging is applied in two steps, first by “pre-summing” by a factor of 2 in azimuth and then by “multi-looking” by another factor of 2 in azimuth. No averaging is applied in the range direction. The result is a pixel which is approximately 40 m wide in range and 50 m long in azimuth. To match these dimensions, the DEM was resampled to 40 m x 40 m pixels.

By averaging the interferometric images by a 2x1 multi-looking window rather than a larger multi-looking widow results a high level of noise. Because of this noise level, the correlations between the master and the slave or the simulated radar image of the DEM failed in few cases. There were also constraints regarding the study area since the large portion of the data frame is covered by sea. Similarly, the fine resolution DEM coverage was very small compared to the whole data frame.

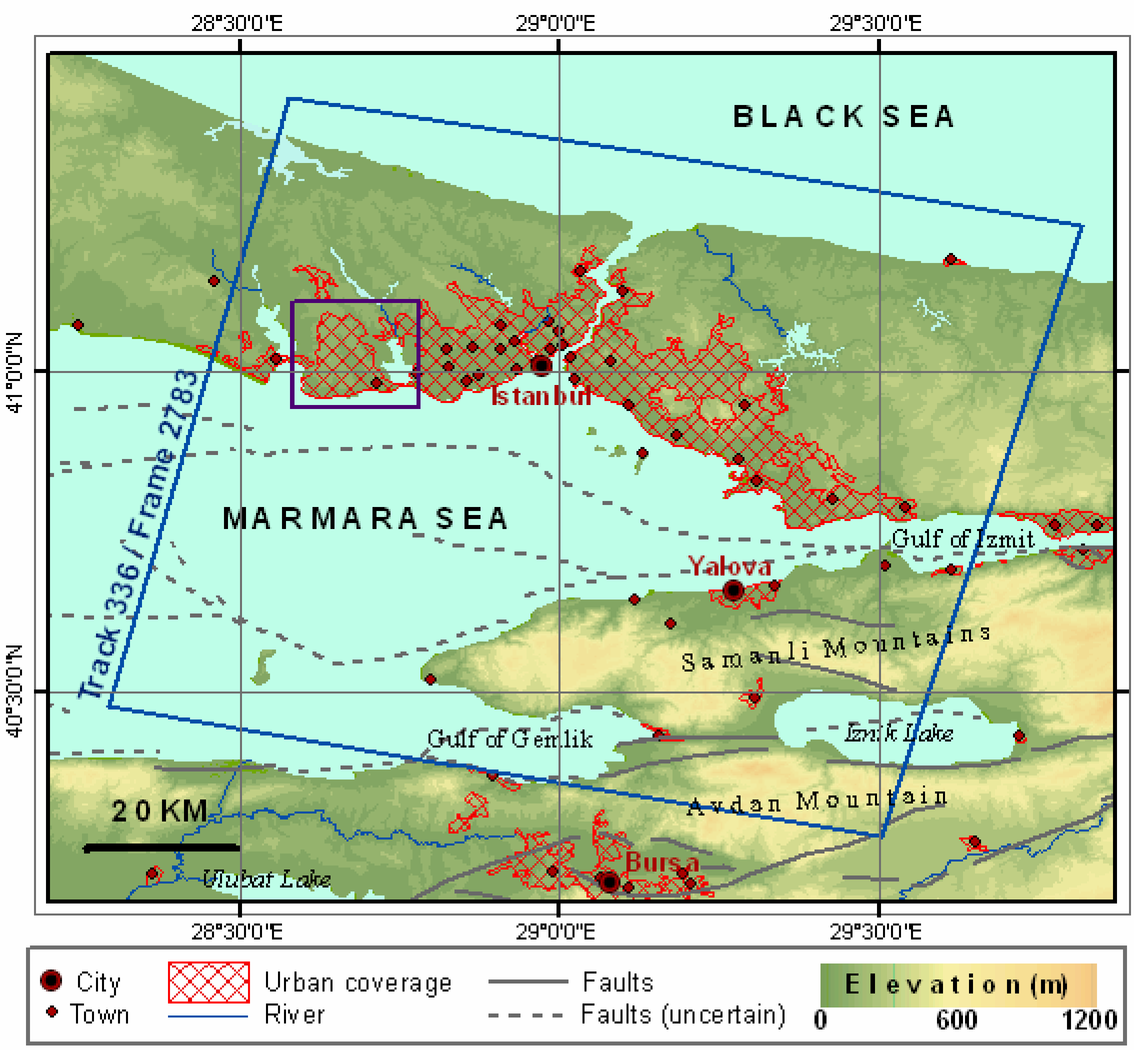

Figure 3.2 : Geographical coverage of T336/F2783 of ERS satellite (blue frame). The frame covers an approximately 100 x 100 km area. Small purple frame shows the coverage of interferograms analyzed in this study (Appendix B). Faults are taken from Armijo et al., 1999 and the elevation map is created from SRTM data.

3.4.1. Amplitude formation

All 48 SAR acquisitions between 1992 and 2002 were focused and geocoded. The DIAPASON processing parameters were set to calculate;

(a) four-byte integer complex ("ci2") values with a gain of 1 (in "prisme"),

(b) four-byte amplitudes with a gain of 1 (in "prisme"),

(c) four-byte geocoded amplitudes with a gain of 1 (in "interf_mnt").

3.4.2. Interferogram formation

The interferometric data pairs of T336/F2783 having an altitude of ambiguity in absolute value H_{amb} larger than 100 m were selected at the first step. This list containing 97 interferograms is given in Appendix A. Then the number of interferograms was reduced according to the following criteria:

▪ Data pairs having a Doppler difference more than 0.4 PRF were avoided.

▪ 30 SAR acquisitions between the years 1992 and 1999 were selected. The acquisitions after the August 17, 1999 Izmit Earthquake were excluded. More details about the time coverage of the data pairs are given in the next sections. No restrictions were made for the time span or the seasonal properties of the data pairs.

▪ The interferograms containing atmospheric and orbital fringes were carefully investigated with "pair-wise" logic. The interferograms severely affected by these contributors were eliminated.

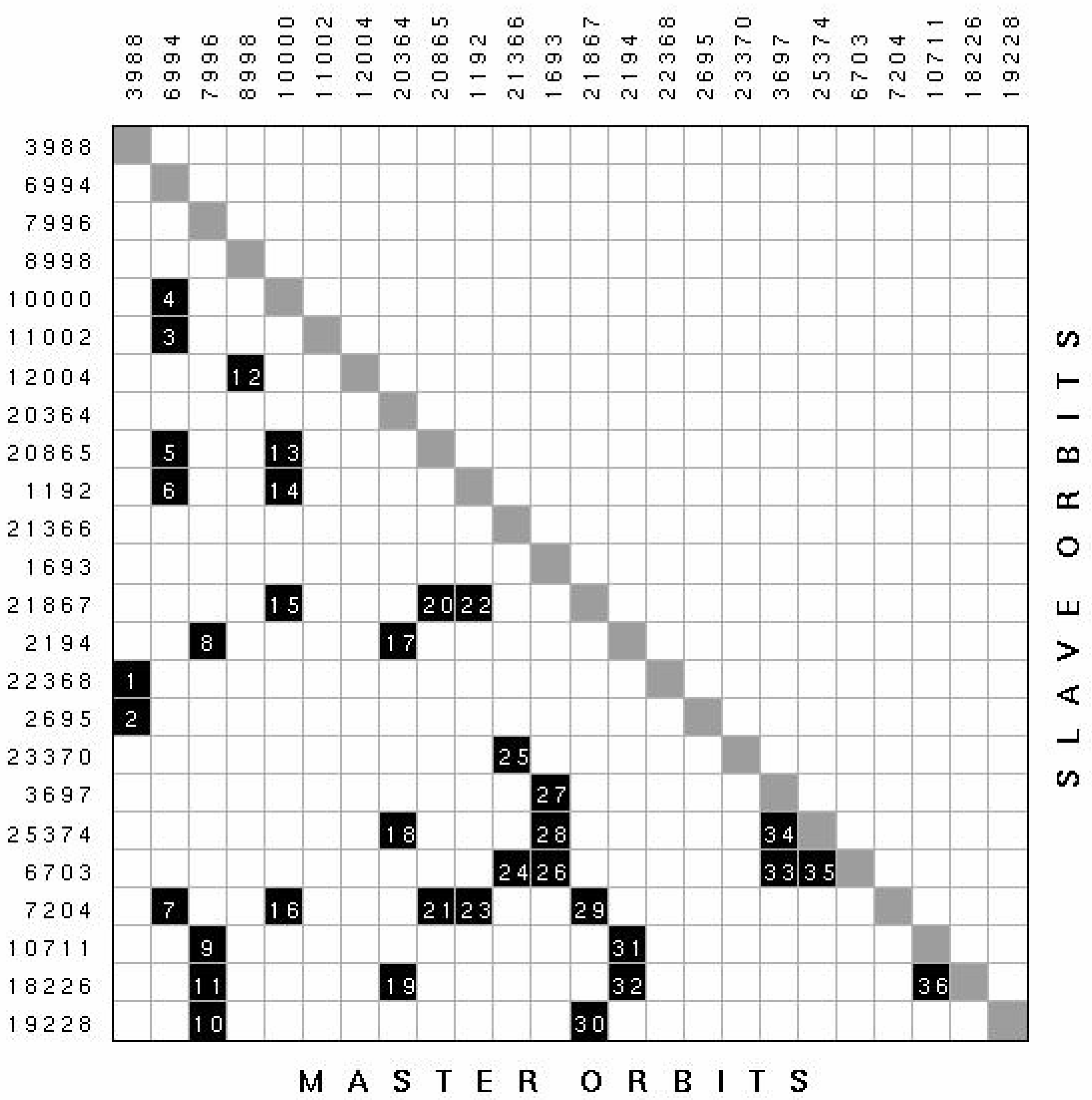

Figure 3.3 : Matrix of image pairs analyzed in T336/F2783 for this study. Each black square corresponds to an interferogram. The Master and the Slave orbits forming the interferograms are shown on the horizontal and the vertical axis, respectively. The numbers are used to label the interferograms. Gray squares represents the interferograms with the same Master and Slave orbits.

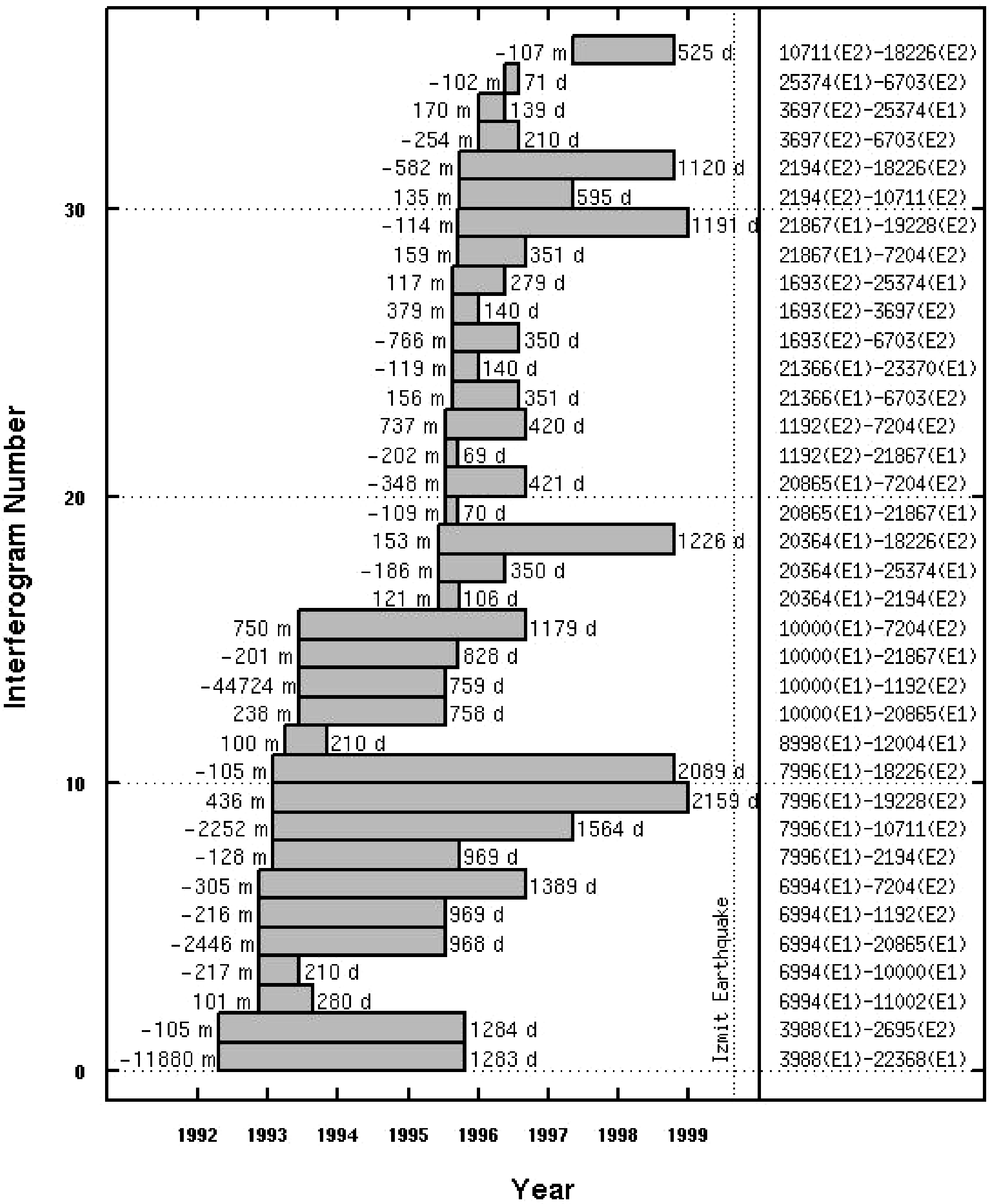

Figure 3.4 : List of interferograms analyzed in T336/F2783 for this study. Time span of the interferograms are shown as gray bars. The number on the left side of the bars is the altitude of the ambiguity in meters and the number on the right side is the time difference in days. The orbits forming the interferograms are given on the right side of the graph. E1 and E2 represent the ERS satellites. Note that the time spans of the interferograms do not include the 1999 Izmit Earthquake.

- “Noisy” interferograms having no coherence around İstanbul city were eliminated.

Regarding this selection criteria, 36 data pairs retained from the 445 possible combinations of image pairs (C_2^{40} = 30x29/2). Figure 3.3 presents a matrix of 36 image pairs selected for further analysis.

Figure 3.4 gives the list of the 36 interferograms according to their time span and altitude of ambiguity. These interferograms are graded as “A” in the list given in Appendix A. For the interferogram formation, the DIAPASON processing parameters were set;

(a) to calculate four byte integer complex values with a gain of 100 (in “prisme”),
(b) to calculate one-byte amplitudes with a gain of 10 (in “prisme”),
(c) to form geo-coded interferograms in signed one-byte with a gain of 1 (in “interf_mnt”),
(d) to use the average Doppler of the data pairs in azimuth,
(e) to exclude the topographic slope filtering (Massonnet et al., 1994),
(f) to apply phase smoothing (linear orbital phase ramp correction, power spectral filtering).

The processing chain failed in a few cases for two reasons. First, a few raw data files were not in a proper format and had to be set up individually. Second, the correlation between the Master and the Slave images failed because of the high noise level in one of the images. In such cases, initial shifts in azimuth and range between the Master and the Slave were estimated manually.

3.4.3. T336/F2783 interferograms

Linear orbital phase ramp correction and power spectral filtering were applied to all the T336/F2783 interferograms. After visual assessments, it was observed that the filtered interferograms (“psp”, see section 2.4) were easier to interpret than “raw” interferograms (“pha”).

Appendix A gives the list of interferogram titles. The best 36 interferograms are indicated as “A quality” in the list. These interferograms are generally noisy because of the dense vegetation cover in the Eastern Marmara region. However, the interferograms exhibit good correlation in the urbanized areas. In particular, the extensive urban coverage of İstanbul city exhibits very good coherence in most of the interferograms. Figure 3.5 shows one of the A quality interferograms.

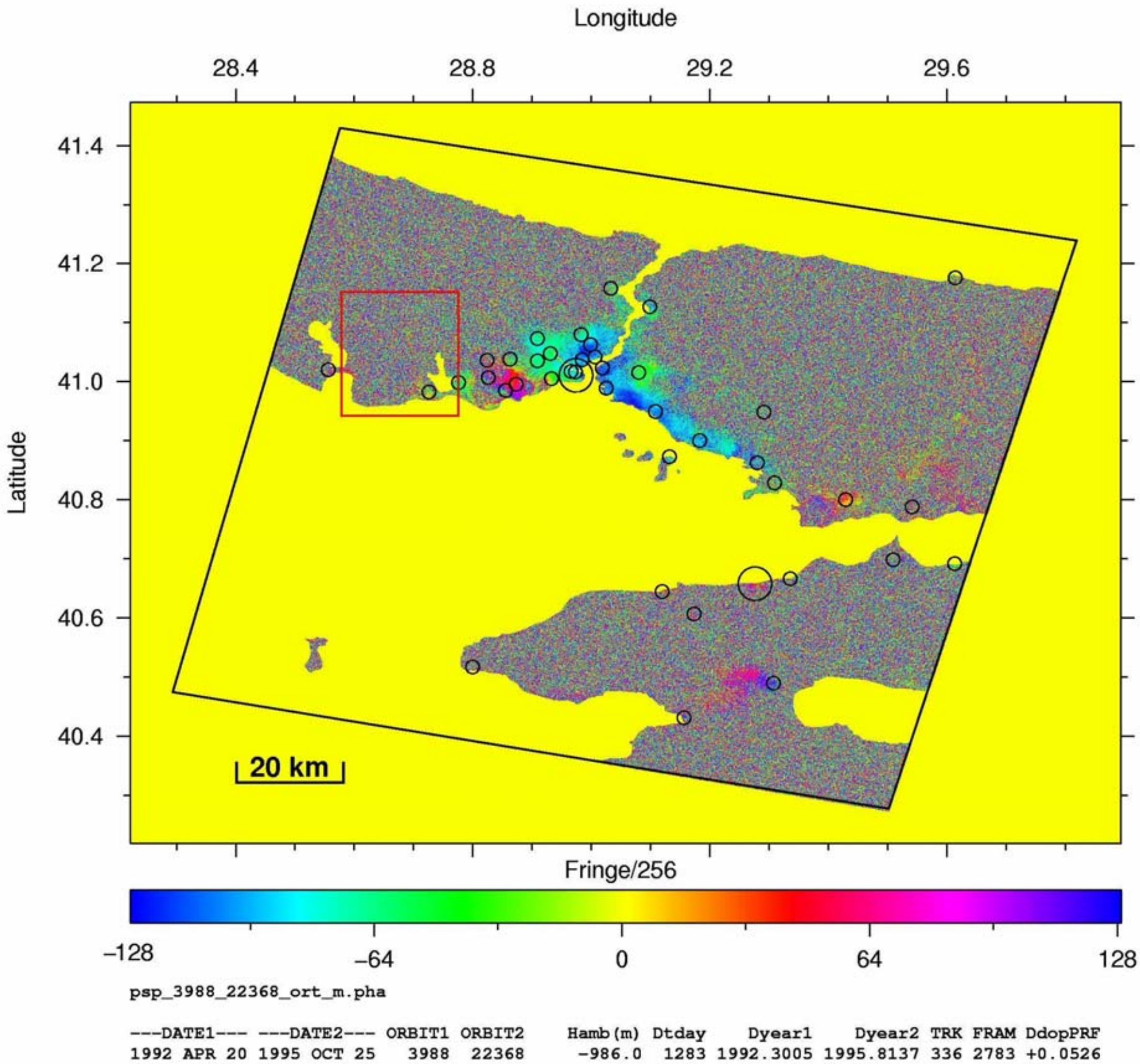

Figure 3.5 : One of the high quality interferograms in the T336/F2783 data set. In the interferogram title (below), the acquisition dates and the orbit numbers of the Master and the Slave, the altitude of ambiguity in meters (Hamb), the difference of the acquisitions days (Dtday), the decimal years (Dyear), the track (TRK) and the frame (FRM) number and the difference in the Doppler shifts in PRF (DdopPRF) are given respectively. One color cycle represents 28 mm range change (2π radians of phase = 256 DN) along the line of sight of the satellite. Positive phase results from the lengthening of the range in the second SAR acquisition. Urbanized areas of İstanbul city exhibit significant correlation over 3.5 years. Circles show the locations of major settlements. The red frame shows the coverage of interferograms analyzed in this study (Appendix B).

Appendix B gives the A quality interferograms around Avcılar. The land between the lagoons and the northern part of the Küçükçekmece Lake are noisy in most of the interferograms. Avcılar town center, located at the triangular area between the Küçükçekmece Lake and the coast, is coherent in most of the interferograms. Another coherent area is noticed at Büyükçekmece town center located between the Büyükçekmece Lake and the sea. As many as 15 interferograms might have atmospheric effects; the interferograms 3, 4, 12, 17, 18, 20, 22, 23, 24, 26, 27, 28, 33 and 35. According to pair-wise logic, the orbits 1693, 1192, 25374 and 6703 contain atmospheric affects. Two examples of interferograms are shown in Figure 3.6.

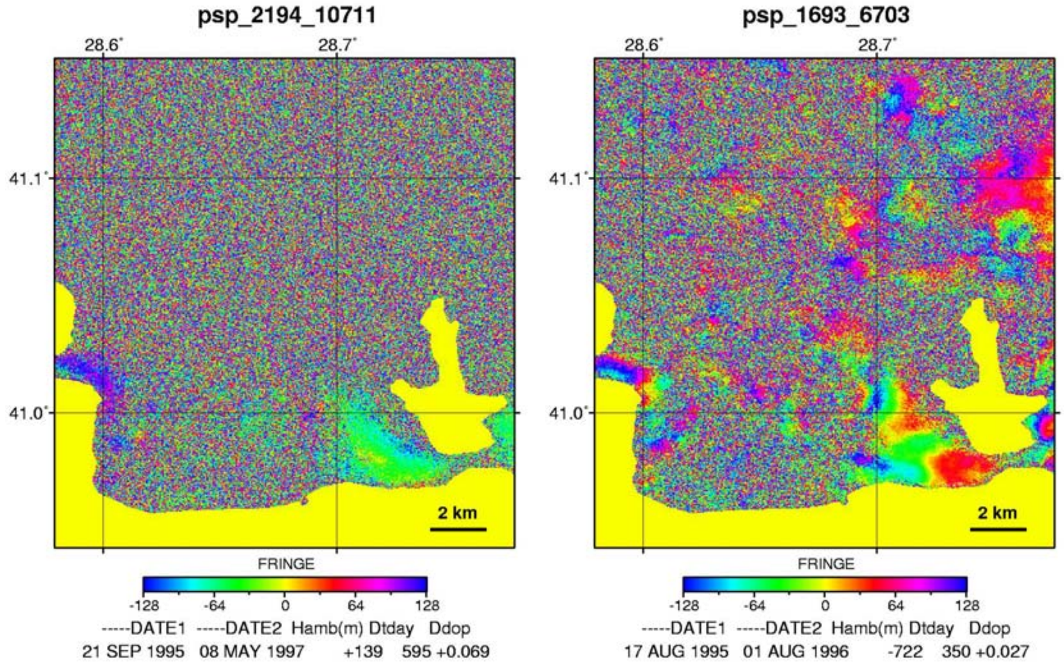

(a) (b)

Figure 3.6 : Two interferograms of the Avcılar vicinity (For the explanation of the interferogram titles, see the previous figure). (a) The interferogram No 31 spanning more than two years exhibits good correlation around Avcılar and Büyükçekmece towns (green and blue, respectively). If we had been analyzing only this single interferogram, we would have concluded that Avcılar was having an "uplift" (or, positive vertical change) rate of ~2 mm/yr and Büyükçekmece a "subsidence" (or, negative vertical change) rate of ~5 mm/yr. (b) The interferogram 26 spanning almost one year is affected by atmospheric contributions.

3.5. Identification of Persistent Scatterers

In this step, the point targets persistent to phase decorrelation will be selected through their amplitude dispersion index (D_A) and standard deviation of phase. The theoretical aspects of the approach are explained in Chapter 2.

3.5.1. Calibration of the amplitude images

The amplitude stack was calibrated by the approach suggested by Lyons & Sandwell (2003). As they described in their study, they calculated "the average calibration factor" for each amplitude image using the ratio of the amplitude of each image (mean pixels) X_k to the mean of the amplitude stack X_{stack} as

$$A_{ijk} = a_{ijk} \frac{X_{stack}}{X_k} \quad \textbf{(3.1)}$$

Accordingly, the amplitude pixels a_{ij} of image k was calibrated to give A_{ij}. One of the main reasons of choosing this kind of relative calibration method is its simplicity. This method, similar to histogram equalization, is independent from any InSAR processing software and does not require any additional radar parameters.

By applying the calibration method of Lyons & Sandwell (2003); the mean and the standard deviation of the new amplitude stack brightness was found to be 10.53 and 5.07, respectively (Figure 3.7). Sea coverage was masked to avoid biasing the statistics.

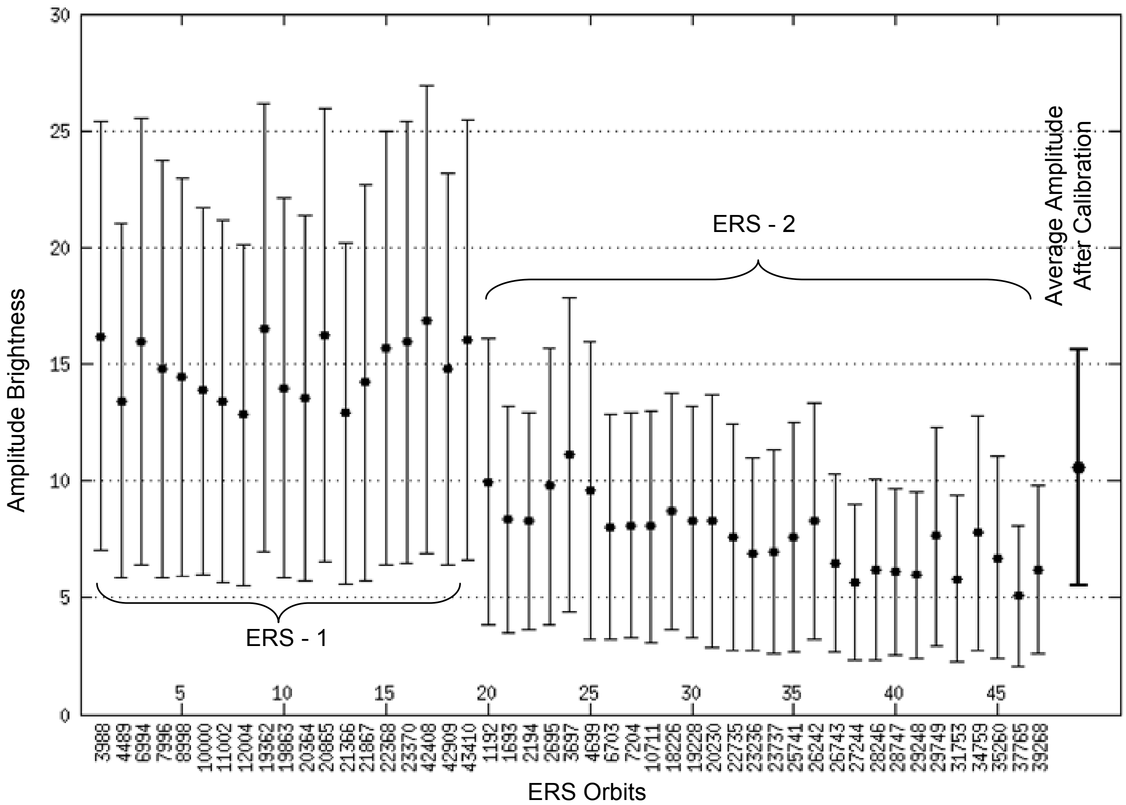

Figure 3.7 : Calibration of the T336/F2783 amplitude stack. Each amplitude image is represented with its mean and standard deviation. The last presents the mean and standard deviation of the calibrated amplitude images.

Figure 3.7 gives the mean and the standard deviation of the ERS amplitude stack containing 47 scenes. Only one of the scenes was excluded from the computations because of the gain problem in the amplitude image. The minimum brightness values of all the amplitude images are close to 0 and the maximum values vary between 500 and 1200. As seen from the Figure 3.7, ERS-2 amplitudes have lower brightness values than ERS-1 amplitudes and appear darker. Figure 3.8 shows the amplitude image computed by averaging all the calibrated amplitudes.

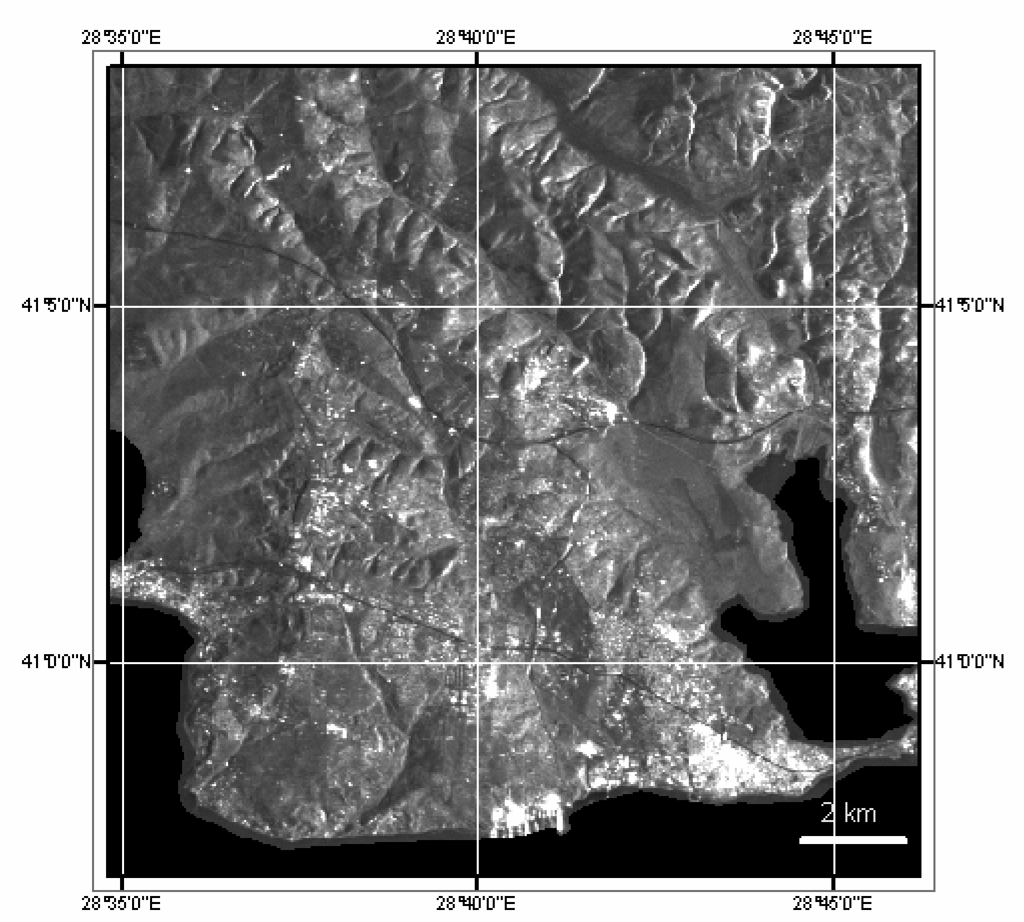

Figure 3.8 : The amplitude image of Avcılar vicinity subset from T 336/F2783 after averaging the 47 calibrated amplitude images. For the averaging, 47 ERS scenes between 1992 and 2002 were used. The brightness values of this frame varied between 0 and 160, and were scaled between 0 and 25 (~2.5 standard deviation) for visual purposes. Bright point targets correspond to urban and industrial areas.

3.5.2. Amplitude dispersion index coverage

Amplitude dispersion index D_A coverage for T336/F2783 was computed (Figure 3.9) as described in Chapter 2. The ERS amplitude stack containing 47 SAR scenes between 1992 and 2002 were used in the calculations. Sea surface was excluded to avoid biasing the statistics.

As Ferretti et al. (2001) describe the probability density function of amplitude values tends to a Rayleigh distribution for low SNR and it approaches a Gaussian distribution for high SNR. By definition, amplitude dispersion index D_A values less than 0.25 are good estimates of high SNR (> 4). Accordingly, the small values of D_A (typically < 0.25) are used for good estimates of phase measurement.

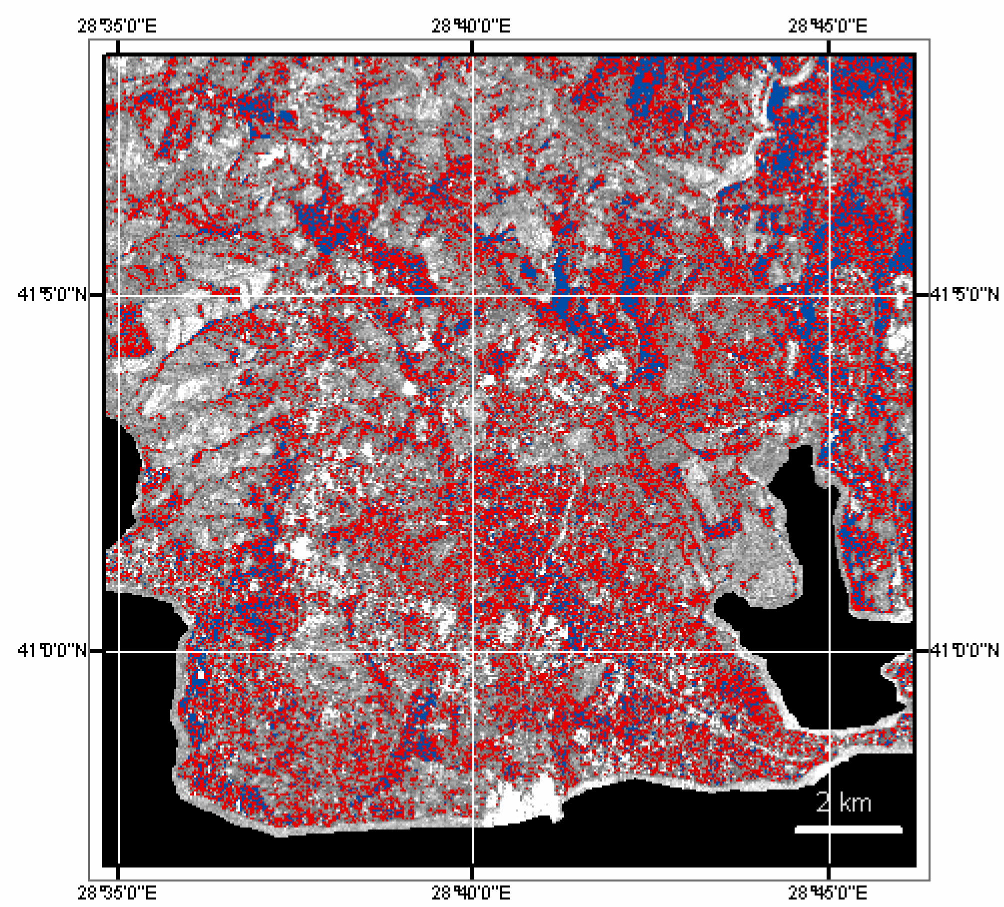

Figure 3.9 : Amplitude dispersion index D_A coverage of Avcılar vicinity. The blue pixels represent D_A between 0 and 0.20 and the red pixels between 0.20 and 0.25. Obviously, D_A tends to be between 0.20 and 0.25. The pixels from gray to white represent the other interval of the histogram that is greater than 0.25. The light gray color pixels corresponding to valleys, agricultural areas and other natural terrain have quite high Da. Also notice that the harbor and the highway crossing Avcılar downtown do not present stable amplitude values over time.

The distribution of D_A in the Avcılar frame (containing ~200.000 pixels) is given in Figure 3.10. The D_A values in the data frame have a mean of 0.29 and a standard deviation of 0.10. The values vary between 0.11 and 4.10. D_A values greater than 1.00 (corresponding to 0.2% of the pixels) are not shown in the histogram. The shape of the histogram fully satisfies the explanations of Ferretti et al. (2001). The right side of the histogram fits a shifted (by 0.16) Rayleigh distribution with a mean of 0.095. The right side fits a Gaussian distribution with a mean of 0.255 and a standard deviation of 0.05. The minimum value of the original distribution (0.11) is the same with the experiment of Ferretti et al. (2001).

However, a discrepancy occurs between the Gaussian model and the data values in the right tail of the histogram. It might be the consequence of the calibration method. When calibrating the amplitude images by a method similar to histogram equalization, the means and the standard deviations of the amplitudes tend to be very close to each other.

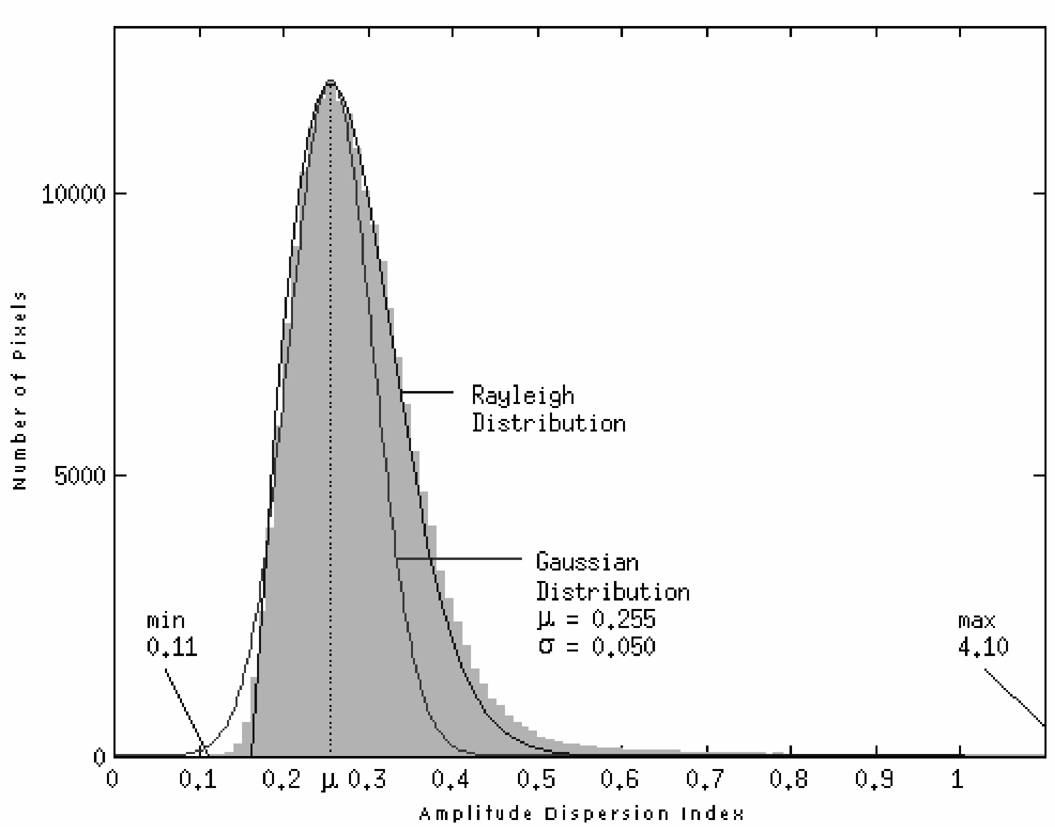

Figure 3.10 : Amplitude dispersion index D_A distribution of the Avcılar frame (gray histogram). The right side of the histogram fits the Rayleigh distribution and the right side the Gaussian distribution.

Consequently, pixels with D_A values less than 0.25 are selected. These pixels form the 33% of the study frame, (excluding the sea surface). In the next step, the coherence of the selected pixels will be analyzed.

3.5.3. Coherence Analysis

The interferograms with less atmospheric contribution were selected for multi-coherence calculations. Pair-wise logic was applied to eliminate the interferograms with atmospheric contribution. Also unwrapped profiles containing several hundred pixels were used to understand the phase variations in the interferograms. Finally, 15 interferograms (numbers 1, 2, 4, 6, 7, 8, 9, 10, 11, 14, 16, 19, 21, 31 and 32) were selected to calculate the multi-coherence of the stack.

The multi-coherence image has a mean value of 0.23 which is quite low (Figure 3.11). There are almost no pixels having a multi-coherence value greater than 0.75. So a threshold of 0.50 was set. The pixels having a multi-coherence value more than 0.5 were selected. These pixels cover the 1.7% of the Avcılar frame.

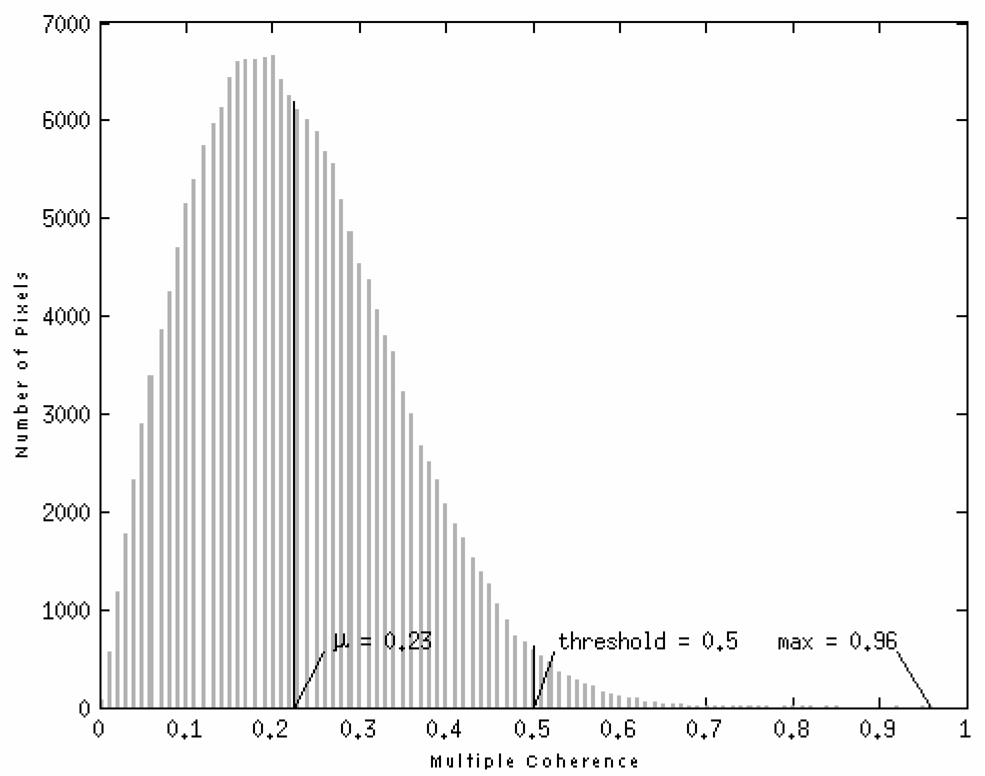

Figure 3.11 : Distribution of the multi-coherence values in the Avcılar frame.

3.5.4. Selection of persistent scatterers

Persistent scatterers were selected by setting a coherence threshold of $\gamma > 0.5$ and an amplitude dispersion index threshold of $D_A < 0.25$. Figure 3.12 shows the scatterplot of the pixels in the data frame according to their standard deviation of phase and the amplitude dispersion index. 1257 PS pixels representing the 7 x 7 km area were found (the pixels in the back box in Figure 3.12). These pixels constitute the ~ 1% (0.64%) of Avcılar data frame. PS density is ~ 4 PS/km^2.

The PS density of ~ 4 PS/km^2 is comparable to the results of Ferretti et al. (2000). To analyze urban subsidence in the city of Pomona (CA, USA) (16 x 20 km), they found a PS density of ~ 3 PS/km^2 by eliminating the pixels having coherence less than 0.75 ($\gamma > 0.75$). By using the same thresholds, Ferretti et al. (2001) analyzed the landslide area in Ancona region (Italy) (5 x 4 km). In that study, they found PS coverage of 1%. Hooper (2006) also found PS density of 3 PS/km^2 to analyze the volcanic deformation of Alcedo (Galapagos) by applying a threshold of 0.6 radians ($\gamma \approx 0.83$) to the phase standard deviation.

The PS distribution in the Avcılar data frame does not show any pattern when plotted on a map. Moreover, it is does not show any pattern difference between

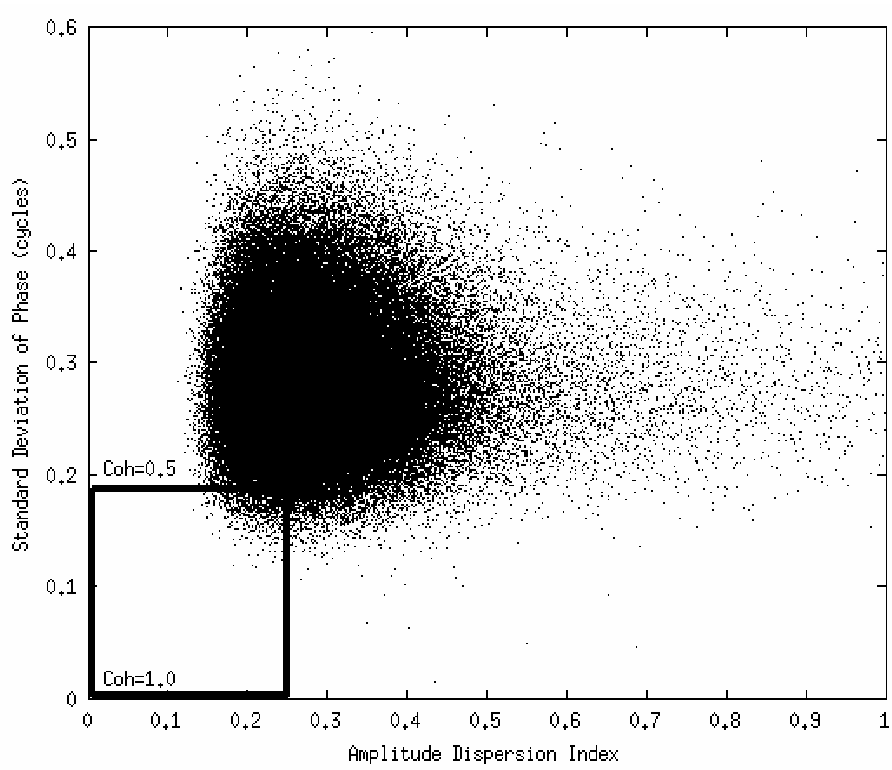

Figure 3.12 : Scatterplot of amplitude dispersion and standard deviation of phase. The back box shows the thresholds for PS selection.

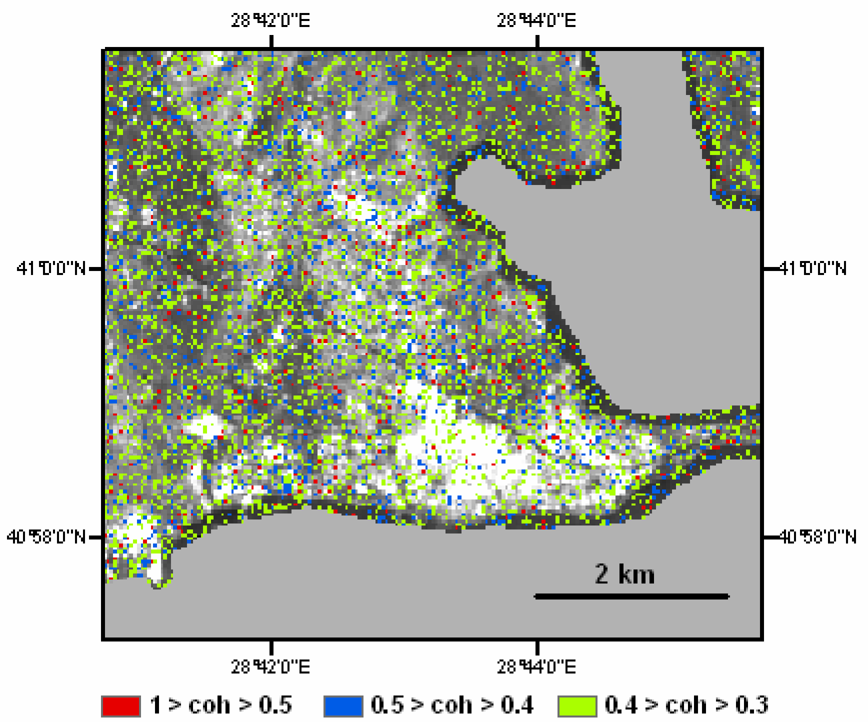

Figure 3.13 : An enlargement to the multiple-coherence image superimposed on the calibrated amplitude. White area in the middle is Avcılar downtown. The red color represents the "highly" coherent pixels. Notice that the locations of the coherent pixels are quite random and do not show any clear pattern.

urban and rural areas (Figure 3.13). It is important to note that in this area, the annual population growth rate between 1990 and 2000 was at least 5%. The urban coverage has dramatically changed since 1990's. Since the amplitude dispersion index was computed from the ERS SAR images acquired between 1992 and 2002, the altered urban coverage might have affected the number of persistent scatterers. The oldest settlement in the region is Avcılar downtown. Therefore, I have chosen the western side of Kucukcekme Lake that also includes the downtown of Avcılar. The geophysical characteristics of the area were explained in the beginning of the chapter in detail. Finally 237 PS pixels were chosen for deformation analysis. In this group of PS pixels, the longest distance between two pixels is less than 1.5 km.

3.6. Temporal Adjustment

3.6.1. General Inversion for Phase Technique (GIPhT)

Feigl and Thurber (2007) have developed a scheme, called "General Inversion for Phase Technique" (GIPhT), for analyzing interferograms without unwrapping them. The new idea here is to define a misfit cost C in terms of wrapped phase. The cost function C may be interpreted geometrically as the L_1 norm of the phase angles between the data phasors and model phasors. The cost function C ranges from 0 to ½ cycle per pixel. By minimizing the cost C with a simulated annealing algorithm (Kirkpatrick et al., 1983), this approach can solve simultaneously for both linear and non-linear parameters.

Following Feigl and Thurber's GIPhT, the phase change between the master epoch t_i and slave epoch t_j for the th pixel in an interferogram is written as

$$\phi_{ij}^{k} = \phi^{k}(t_j) - \phi^{k}(t_i) \quad \textbf{(3.2)}$$

Generalizing to a time series of images, with $Q \geq 2$ epochs forming $P \geq 1$ pairs, we write the phase change for a single pixel in matrix form

$$\phi_{ij}^{k} = D \begin{bmatrix} \phi^{k}(t_{j=1}) \\ \phi^{k}(t_{j=2}) \\ \ldots \\ \phi^{k}(t_{j=Q}) \end{bmatrix} \quad \textbf{(3.3)}$$

where D is a differencing operator defined such that

$$ {}^{k}D_{pq}^{(i,j)} = \begin{cases} -1 \text{ for } q = i \text{ (master)} \\ +1 \text{ for } q = j \text{ (slave)} \\ 0 \text{ for } q \neq j \text{ (neither)} \end{cases} \quad \textbf{(3.4)} $$

Here, the index p ranges over the P pairs and index q ranges over the Q epochs. Thus the D operator has Q rows and P columns for each pixel k.

The system of equations described by 3.2 thus specifies the phase change at location (pixel) k in the interferometric pair spanning the time interval between epochs t_i and t_j. For simplicity, however, GIPhT assumes that the spatial dependence and temporal dependence are separable, as suggested by Fialko (2004). Accordingly, the modeled phase change for a single pixel with index k is

$$ \phi_{ij}^{k} = D^{(i,j)}\left(fg^{k} + h^{k}\right) \quad \textbf{(3.5)} $$

where f is a function of time only ($\partial f/\partial x$ = 0); g is a mapping function of space only ($\partial g/\partial t$ = 0) that describes the signal of interest, the geophysical deformation on the ground; and h is a mapping function of space only ($\partial h/\partial t$ = 0) that describes the nuisance effects pertaining to a single epoch such as tropospheric perturbations or residual orbital fringes. It is also safe to assume that the differencing operator D is the same at all locations, i.e. it does not depend on the pixel index k.

In this study, the scalar function $f(t)$ describes the time dependence of the geophysical deformation as secular deformation with constant rate such that f(t) = t.

To describe the geographic dependence, a 2-dimensional vector mapping function is used. This is $g^{k} = g(X)$ of the position k^{th} pixel, $X^{k} = \left[X_E^k \quad X_N^k \quad X_U^k\right]$ written as easting, northing, and upward components reckoned in a local Cartesian reference system (see section 2.2.4.5.) The shape of the deformation field in map view is $g = -u\,\hat{s}$ where u is the vector field of displacements at the surface of the Earth calculated using Mogi's (1958) formulation for an infinitesimal spherical source in an elastic half space and $\hat{s}$ is a position-dependent unit vector pointing from the pixel on the ground to the radar sensor along the line of sight.

The set of model parameters m of interest are thus the Mogi source parameters describing the three position coordinates of the source (easting, northing and depth), as well as its change in volume ΔV. In other words, we parameterize the vertical displacement signal as the product of the time interval $\Delta t = t_j - t_i$ and the deformation field produced by a sink deflating with constant rate dV/dt.

The nuisance parameters h^k depend on position and the time epoch t_i, but not on the time interval Δt, such as tropospheric effects. In this study, we consider a linear simple parameterization in terms of a vertical gradient

$$h^k = -h_U^k \left(X_U^k - X_U^0 \right) \hat{s}^k \tag{3.6}$$

where X_U^0 denotes the vertical (elevation) component of the position coordinate of the reference pixel with index $k = 0$. Summation over the pixel index k is not implied. In other words, we are allowing tropospheric fringes that look like a scaled version of the topographic relief. We estimate one such parameter per epoch. By neglecting horizontal phase gradients, we are neglecting orbital effects, a reasonable approximation over the small (~2 km) dimension of the study area.

The inverse problem consists of estimating the model parameters m from the phase data ϕ_{ij}. We solve the inverse problem using GIPhT (Feigl and Thurber, 2007), based on a simulated annealing algorithm (Kirkpatrick et al., 1983) as implemented by Cervelli et al. (2001).

3.6.2. Selecting interferometric data pairs

Some images do not form useful interferometric pairs because of temoral decorrelation, orbital separation, or differences in azimuthal Doppler frequency. Following Feigl and Thurber (2007), a “species” is described as the set of single-epoch images that can be combined pair-wise to form a useful interferogram. According to this definition, any member of a species can form a useful interferometric pair with any other member of the species, either by direct calculation, or by construction, i.e. linear combination of pairs of other members of the species.

From the T336/F2783 data set containing 36 interferometric pairs, single large specie with 33 pairs is available (Figure 3.14). In this specie, some of the epochs form only one or two interferometric pairs. By eliminating such “isolated” epochs, we reduce the data set by 2 epochs. Some other orbits are eliminated because of their poor image qualities. For example, the interferograms including the orbit 19928 are eliminated because of the temporal decorrelation. When combined with the orbit 21867 and the orbit 7996, this image yields interferograms spanning ~3.3 and ~6.0

years that do not show coherent fringe patterns. The orbit 6703 appears to have atmospheric variations in local scale. The interferograms combining orbit 6703 show fringe patches over the area that causes problems in the modeling process.

Table 3.2 : SAR images of the T336/F2783 data set used for modeling.

Epoch	ERS Orbit	Date	Year	Specie
01	- 6994	1992-NOV-16	1992.87	A
02	- 7996	1993-JAN-25	1993.07	B
03	- 10000	1993-JUN-14	1993.45	A
04	- 20364	1995-JUN-07	1995.43	B
05	- 20865	1995-JUL-12	1995.53	A
06	+ 1192	1995-JUL-13	1995.53	A
07	+ 1693	1995-AUG-17	1995.62	B
08	- 21867	1995-SEP-20	1995.72	A
09	+ 2194	1995-SEP-21	1995.72	B
10	+ 3697	1996-JAN-04	1996.01	B
11	- 25374	1996-MAY-22	1996.39	B
12	+ 7204	1996-SEP-05	1996.68	A
13	+ 10711	1997-MAY-08	1997.35	B
14	+ 18226	1998-OCT-15	1998.79	B

(-) and (+) indicate ERS-1 and ERS-2 satellite, respectively.

After eliminating 3 images at isolated epochs and 2 images that form low-quality interferograms, we retain the 14 images listed in Table 3.2 for further analysis. Pair-wise combination of these 14 epochs gives 24 high-quality interferometric pairs listed in Table 3.3. The corresponding 24 interferograms constitute the data set considered in the modeling described below. It contains two species, labeled A and B, and shown as red and blue networks in Figure 3.14.

3.6.3. Estimate of model parameters

The inverse problem consists of estimating the model parameters from the phase data. GIPhT uses “a simulated annealing algorithm” to estimate the model parameters fitting the interferograms. In this study, a vertical ground motion with a constant rate is modeled by using a simple 4-parameter Mogi source (easting, northing, volume, depth). Also, a tropospheric parameter (vertical gradient) for each epoch is introduced to the parameter set. Finally, the parameter set contains a number of 18 free parameters (4 for the Mogi source and 14 for the tropospheric gradients). A summary of the inputs for modeling with GIPhT is given Table 3.4. The prior model parameters of the Mogi source and the tropospheric gradients are listed in the second column of Table 3.5.

Table 3.3 : Interferometric pairs of the T336/F2783 data set used for modeling.

Pair index	Orbit0	Orbit1	Year0	Year1	Δ yr	Specie
01	- 6994	- 10000	1992.87	1993.45	0.58	A
02	- 6994	- 20865	1992.87	1995.53	2.65	A
03	- 6994	+ 1192	1992.87	1995.53	2.65	A
04	- 6994	+ 7204	1992.87	1996.68	3.81	A
05	- 7996	+ 2194	1993.07	1995.72	2.65	B
06	- 7996	+ 10711	1993.07	1997.35	4.28	B
07	- 10000	- 20865	1993.45	1995.53	2.08	A
08	- 10000	+ 1192	1993.45	1995.53	2.08	A
09	- 10000	- 21867	1993.45	1995.72	2.27	A
10	- 10000	+ 7204	1993.45	1996.68	3.23	A
11	- 20364	+ 2194	1995.43	1995.72	0.29	B
12	- 20364	- 25374	1995.43	1996.39	0.96	B
13	- 20364	+ 18226	1995.43	1998.79	3.36	B
14	- 20865	- 21867	1995.53	1995.72	0.19	A
15	- 20865	+ 7204	1995.53	1996.68	1.15	A
16	+ 1192	- 21867	1995.53	1995.72	0.19	A
17	+ 1192	+ 7204	1995.53	1996.68	1.15	A
18	+ 1693	+ 3697	1995.62	1996.01	0.38	B
19	+ 1693	- 2537	1995.62	1996.39	0.76	B
20	- 21867	+ 7204	1995.72	1996.68	0.96	A
21	+ 2194	+ 10711	1995.72	1997.3	1.63	B
22	+ 2194	+ 18226	1995.72	1998.79	3.07	B
23	+ 3697	- 25374	1996.01	1996.39	0.38	B
24	+ 10711	+ 18226	1997.35	1998.79	1.44	B

(-) and (+) indicate ERS-1 and ERS-2 satellite, respectively.

Table 3.4 : Inputs for GIPhT technique.

No of epochs	14
No of interferograms	24
No of species	2
Geographic coverage	4x5 km
Image size	171x171 pixels
PS criteria	$\|\gamma\|>0.5$
No of PS pixels	387 pixels
No of Mogi sources	3
Easting and northing of Mogi source 1	X1 = -700 m Y1 = -1700 m
Easting and northing of Mogi source 2	X2 = X1 - 1800 m Y2 = Y1 + 500 m
Easting and northing of Mogi source 3	X3 = X1 - 1550m Y3 = Y1 + 3300 m

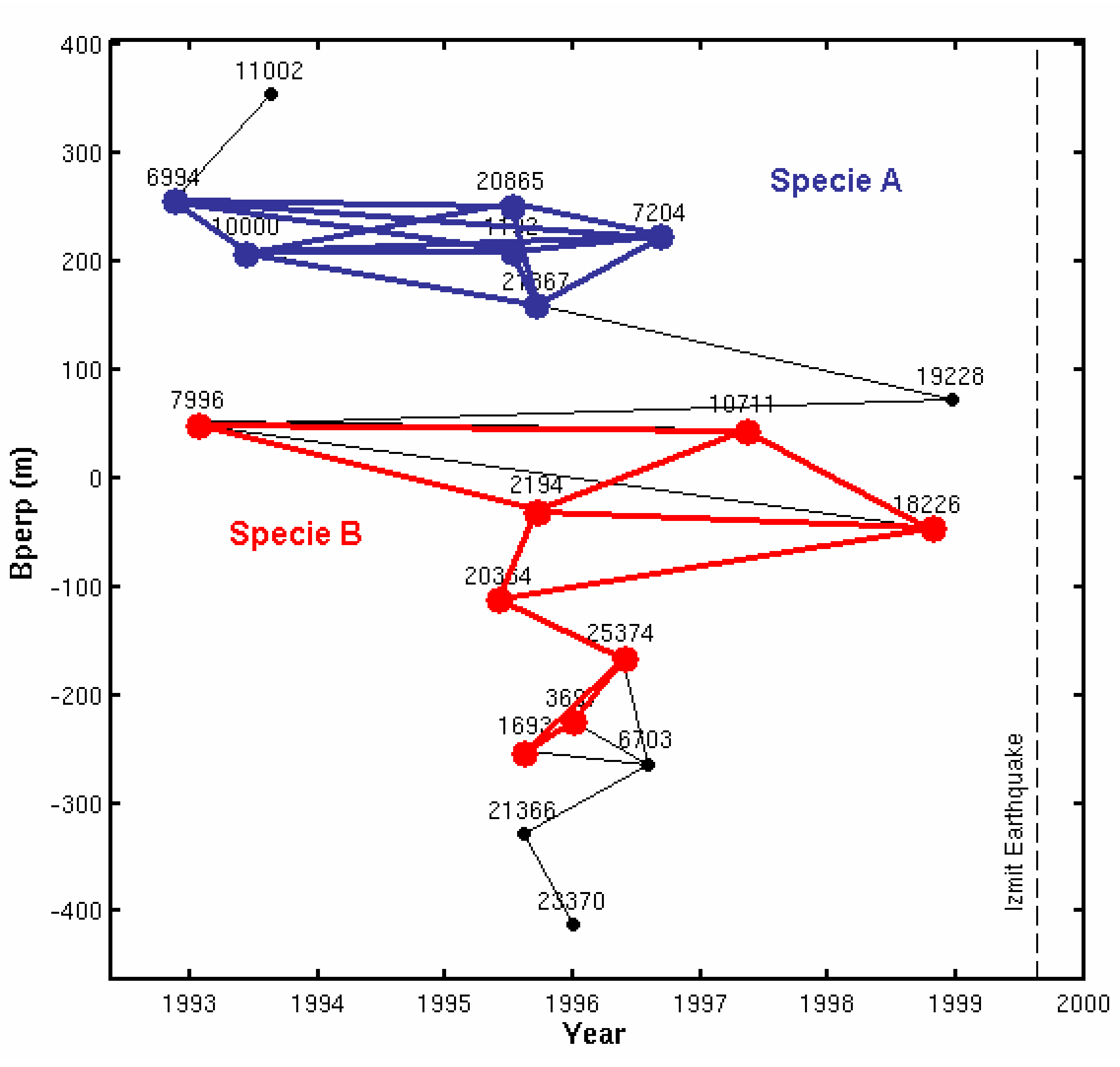

Figure 3.14 : Orbital seperation versus time for the radar images analyzed in this study. 19 individual images (epochs) are shown as circles. The 33 interferometric pairs considered here are shown as line segments connecting the circles. 14 pairs forming 24 interferometric pairs fall into two distinct “species”, labeled A (blue) and B (red). The horizontal coordinate displays the acquisition date (epoch) of each image in decimal years. The vertical coordinate shows the orbital separation, or perpendicular component of the “baseline” vector between the positions of the radar sensor at the acquisition epoch. For a single image, the orbital separation is calculated with respect to a virtual orbit. The dotted line shows the date of the M 7.4 Izmit Earthquake on 17 August 1999.

PS pixels are considered for inversion. As described in previous sections in detail, the evaluation is based on two criteria, one is the “multiple coherence” of the phase measurements and the other is the “amplitude dispersion index”. Applying both criteria, 163 pixels remain for the inversion of the area in interest. The distribution of the pixels is ~3 PS/km^2. Applying only the coherence threshold, we obtain 387 pixels with an areal density of approximately ~7 PS/km^2. Since the total costs for the prior and final estimates improve slightly when using the points selected only with the coherence threshold, we retain the 387 pixels so selected for the subsequent analysis. This issue will be mentioned again in the further sections.

Observing the common features of the fringe pattern on the interferograms spanning different time intervals, three Mogi sources have been located. The ground motion map of İstanbul produced by GMES Terrafirma (UKNERC, 2004) has been considered for determining the locations of the sources. To keep the model simple, the same volume and depth parameters have been used for all of the sources. For the source parameters, the depth and annual volume change rate are set to within the ±30% of the initial values. For the easting and the northing coordinates of the source, the bounds are set to ± 600 m away from the initial location.

Initially, the prior tropospheric parameters are set to 0.03 mm/m per epoch (see Section 2.2.4.4). This vertical gradient corresponds to a difference in path delay of 4 mm in range between a pixel located at highest point in the Avcılar area at an elevation of 135 m and a pixel located at sea level. Although the epochs with atmospheric artifacts are recognized by pair-wise logic, it is not easy to decide the sign and the magnitude of the atmospheric phase contribution in the interferograms. Running the GIPhT on trial-and-error basis, the possible tropospheric phase gradients for some epochs are found to be higher than the theoretical value. The estimates of the trial-and-error analysis form the prior tropospheric gradients given in the second column of the Table 3.5. The upper and lower bounds for the tropospheric gradient parameters are set to within approximately ±0.056 mm/m of the initial values.

Once the simulated annealing algorithm has located the minimal cost, the corresponding values of the parameters remain as the final estimate of the model parameters, as listed in the third column of the Table 3.5. In this step, only the PS pixels are used. To evaluate the uncertainty of these estimates, we consider each parameter separately to calculate cost as a function of the parameter’s value. The minimum of this function corresponds to the final estimate of this parameter, as expected. The half-width of this function at a cost corresponding to 69% confidence gives the 1-sigma uncertainty (standard error) of the corresponding parameter estimate (Press et al., 1992).

Table 3.5 : Model parameters.

Parameter	Pre-fit value	Post-fit value	Diff %	Adjustment	Uncertainty	Significance
U grad @ epoch 01 (-6994) in mm/m	-1.00E-02	2.36E-02	-336	3.36E-02	8.96E-02	0.38
U grad @ epoch 02 (-7996) in mm/m	-5.00E-02	-1.74E-03	-97	4.83E-02	1.04E-01	0.46
U grad @ epoch 03 (-10000) in mm/m	-7.00E-02	-6.44E-02	-8	5.58E-03	1.10E-01	0.05
U grad @ epoch 04 (-20364) in mm/m	3.00E-02	1.19E-02	-60	-1.81E-02	1.33E-01	0.14
U grad @ epoch 05 (-20865) in mm/m	-5.00E-02	-3.90E-02	-22	1.10E-02	1.34E-01	0.08
U grad @ epoch 06 (+1192) in mm/m	5.00E-02	1.00E-01	100	5.00E-02	9.26E-02	0.54
U grad @ epoch 07 (+1693) in mm/m	5.00E-02	2.51E-02	-50	-2.49E-02	8.09E-02	0.31
U grad @ epoch 08 (-21867) in mm/m	3.00E-02	2.88E-02	-4	-1.25E-03	9.28E-02	0.01
U grad @ epoch 09 (+2194) in mm/m	6.00E-02	1.16E-01	93	5.60E-02	1.21E-01	0.46
U grad @ epoch 10 (+3697) in mm/m	-5.00E-02	-1.04E-01	108	-5.42E-02	1.84E-01	0.29
U grad @ epoch 11 (-25374) in mm/m	-3.00E-02	-2.99E-02	0	6.12E-05	9.96E-02	0
U grad @ epoch 12 (+7204) in mm/m	5.00E-02	6.76E-02	35	1.76E-02	1.13E-01	0.15
U grad @ epoch 13 (+10711) in mm/m	-3.00E-02	-1.13E-02	-62	1.87E-02	1.48E-01	0.13
U grad @ epoch 14 (+18226) in mm/m	4.00E-02	8.19E-02	105	4.19E-02	9.79E-02	0.43
Mogi Easting in m	-7.00E+02	-8.06E+02	15	-1.06E+02	1.89E+03	0.06
Mogi Northing in m	-1.70E+03	-1.86E+03	10	-1.62E+02	6.62E+02	0.25
Mogi Depth in m	1.90E+03	2.30E+03	21	4.02E+02	1.30E+03	0.31
Mogi Volume increase in m^3	-6.20E+04	-7.82E+04	26	-1.62E+04	3.36E+04	0.48

(-) and (+) indicate ERS-1 and ERS-2 satellite, respectively.

The corresponding post-fit residual interferograms (e.g., Figures 3.17(d) and 3.18(d)) show less unmodeled signal than the pre-fit residual interferogram (e.g., Figure 3.17(c) and 3.18(c)). The final estimate of the model parameters fits the observed interferograms better than the prior estimate. The map of the marginal costs for the final estimate (e.g., Figures 3.19(b) and 3.19d) shows lower values than for that for the prior estimates (e.g., Figures 3.19(a) and 3.19(c)).

The final estimate for the depth of the Mogi source is 2300 ± 1300 m. Its volume is decreasing at rate of (–7.82 ± 3) $\times 10^4$ m^3/yr. The maximum rate of range increase is

+0.21 cycle/yr, which we interpret as purely vertical change at 7 mm/yr at a point directly above the volume sink. The estimate of the Mogi parameter set produces the simulated annual vertical displacement in Figure 3.15.

The cost C values for the null, prior and final estimates are 0.255, 0.215 and 0.206 cycles per datum, respectively for the 9288 phase measurements included in the inversion. For the complete data set, including 29,241 unmasked pixels in the 24 pairs, the cost of the final estimate is 0.19 cycles per datum. Both the final estimates of the 18 free parameters are significantly better than the null hypothesis with 95% confidence for both data sets. In addition, the final model fits the data significantly better than the prior model, based on an F-test for 9288 observations, 18 free parameters, and 95% confidence. In both these statistical tests, the confidence values based on the $L2$ norm provide a good approximation to those based on the $L1$ norm when the number of degrees of freedom is large (Parker and McNutt, 1980).

3.6.4. Modeling the interferograms

Using the final model parameters calculated by the simulated annealing program of GIPhT (Feigl & Thurber, 2007), 24 interferometric pair-wise combinations of SAR images of the Avcılar area acquired at 14 different times (epochs) have been modeled.

The estimates of the vertical fringe gradient parameter suggest that the troposphere contributes to the range change in a manner which varies considerably in time. In the worst case, on epochs 9 and 6 (orbits 2194 and 1192), the vertical gradient in range is ~+0.1 mm/m or 13 mm of range over 130 m of topographic relief at the highest point in the study area. Similarly large, significant values are estimated for these epochs, as listed in Table 3.5. On epoch 10 (orbit 3697), the situation is similar but the sign of the range change is different. These values approach the worst-case values documented elsewhere (Goldstein, 1995, Massonnet & Feigl, 1995, Zebker et al., 1997, Williams, et al., 1998, Beauducel et al., 2000, Hanssen, 2001). Other epochs have tropospheric contributions with vertical gradient less than 0.03 mm/m, for example, epochs 1, 2, 5, and 7 (orbits 6994, 7996, and 1693). Similarly small, significant values are estimated for epochs 3, 5 and 11 (orbits 10000, 20865 and 25374).

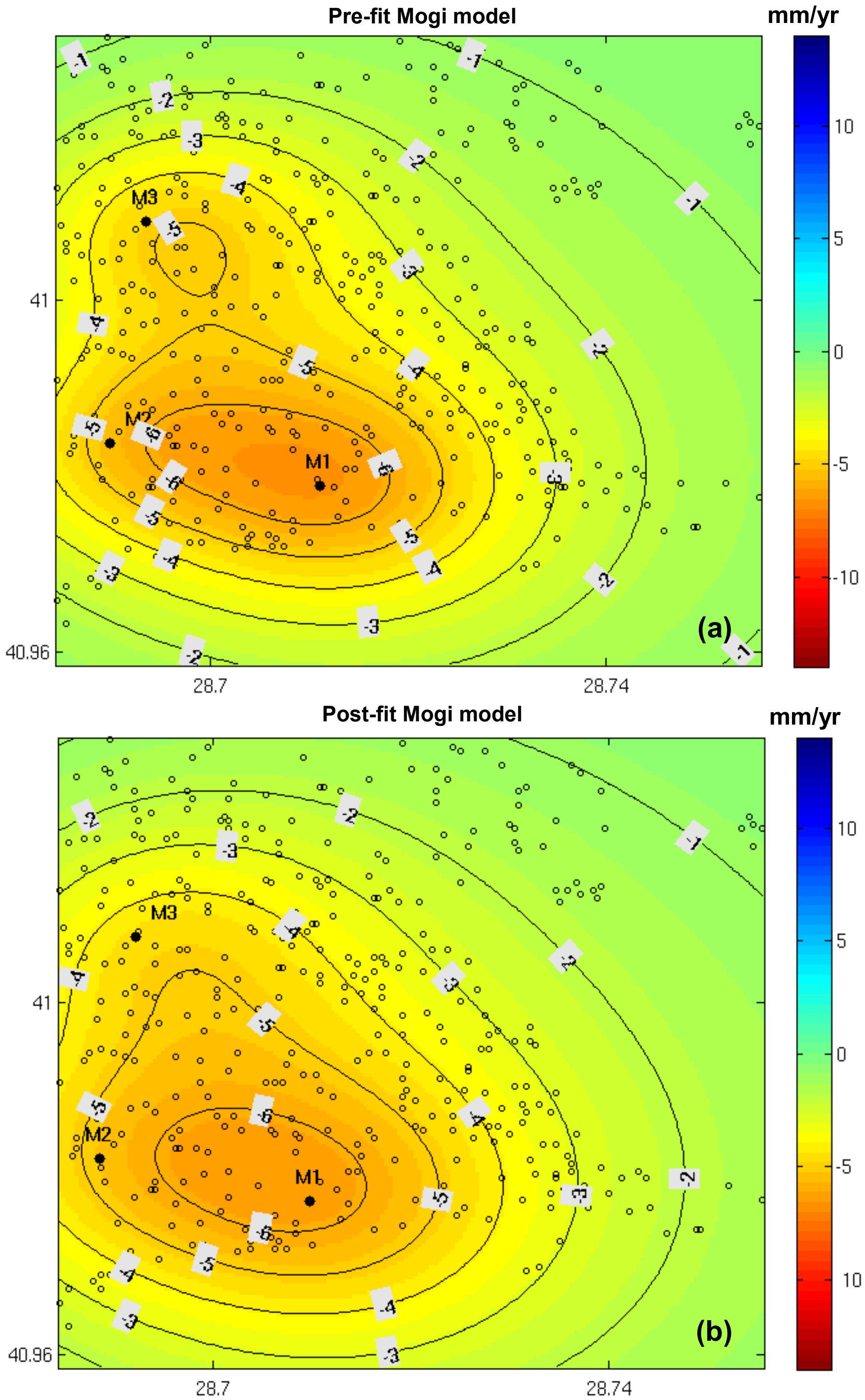

Figure 3.15 : The prior (a) and final (b) estimate of the Mogi source as vertical change rate in mm/yr. Black lines are the contour representation of the models. The dots are PS pixels used for calculating the final estimates. The three black circles are the Mogi source locations.

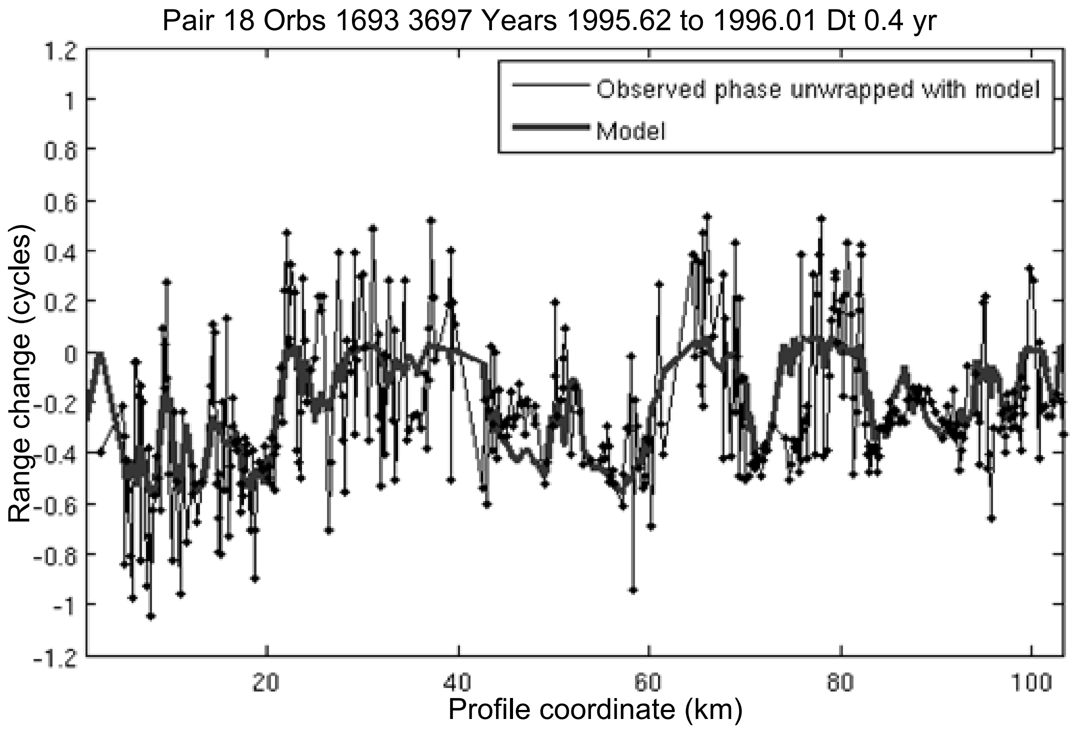

Figure 3.16 : Profile of range change, showing observed phase values unwrapped using the final model (black dots) and the modeled values (red line) of pair 18. The horizontal axis is the distance along the shortest ("traveling salesman's") path (Corpus, 1998) connecting PS pixels selected for analysis with GIPhT (Feigl & Thurber, 2007).

Figure 3.16 shows the observed and modeled values of range change for interferometric pair 18 in a profile passing through the pixels selected for inversion. The modeled curve computed from the final estimates fits the data points within 0.2 cycles in most places, consistent with overall cost of 0.206 cycles per datum.

Figure 3.17 and 3.18 show two modeled interferograms from the T336/F2783 data set. The interferogram displayed in Figure 3.17(a) spans 1.6 years. The interferogram displayed in Figure 3.18(a) spans 4.5 months. Both of the interferograms have tropospheric effects. The final estimate of the parameter set produces the simulated fringe patterns shown in Figures 3.17(b) and 3.18(b). The corresponding post-fit residual interferograms (Figures 3.17(d) and 3.18(d)) show less unmodeled signal than the pre-fit residual interferograms (Figures 3.17(c) and 3.18(c)). The final estimate of the model parameters fits the observed interferograms better than the prior estimate. The maps of the marginal costs for the final estimate (Figures 3.20(c) and 3.20(d)) show lower values than for those for the prior estimates (Figures 3.20(a) and 3.20(b)).

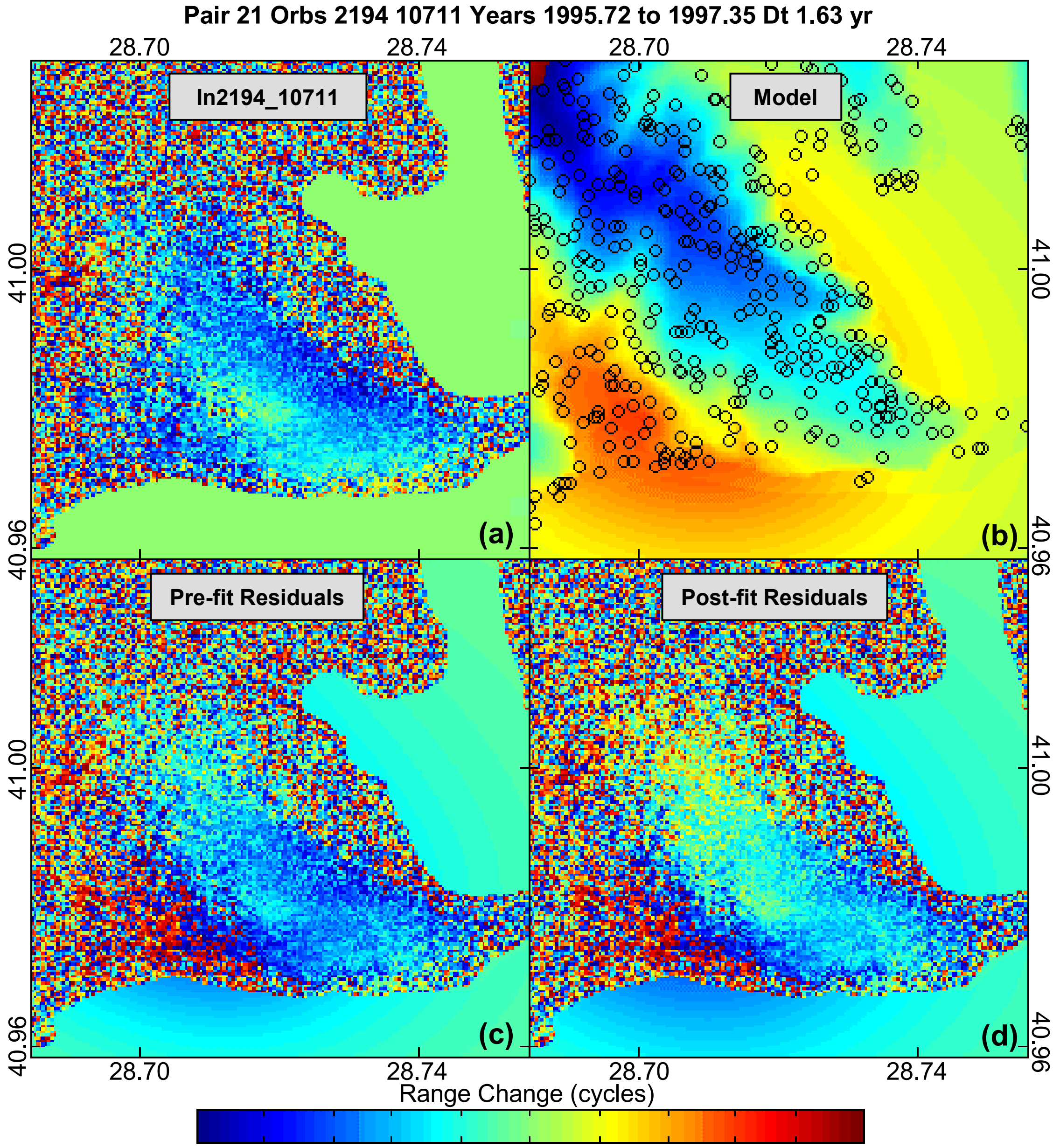

Figure 3.17 : An interferogram from the D336/T2783 data set for the time interval 1995.72 and 1997.35. At the master epoch 1995.72 (orbit 2194), the vertical gradient of the tropospheric contribution is +0.12 mm/m in range that corresponds to ~15 mm range increase at the highest point in the Avcılar area. This is the highest rate in the data set. On the other hand, slave epoch 1997.3 (orbit 10711) has a tropospheric contribution of -0.01 mm/m. (a) Observed fringe pattern. (b) Simulated fringes calculated from the final estimate of model parameters. The dots are PS pixels used for calculating the final estimates. (c) Residual fringes formed by subtracting the simulated fringes calculated from the prior estimate of the model parameters from the observed fringe pattern. (d) Residual fringes formed by subtracting the simulated fringes calculated from the final estimate of the model parameters from the observed fringe pattern. One colored fringe corresponds to one cycle of phase change, or 28 mm of range change.

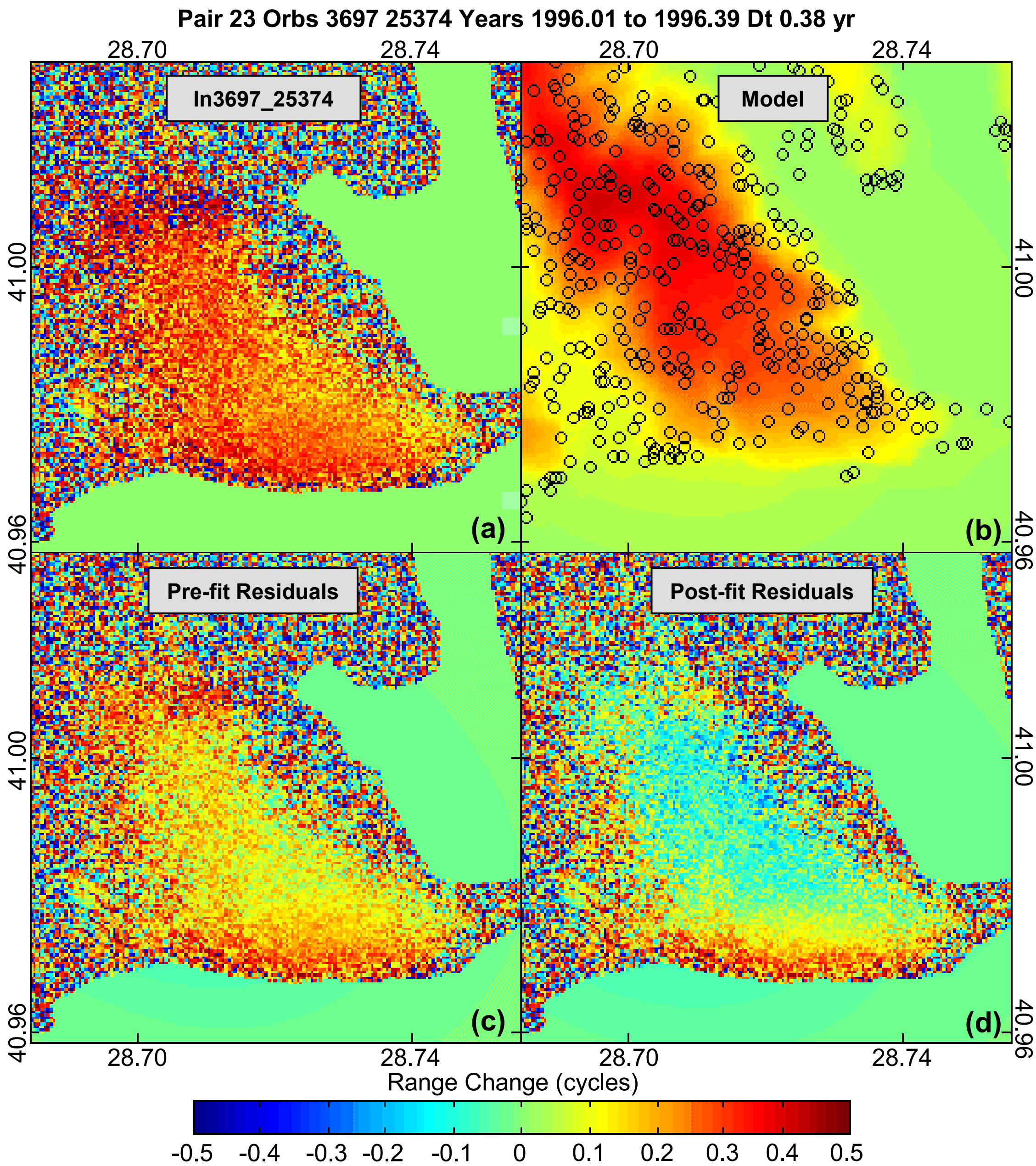

Figure 3.18 : An interferogram from the T336/2783 data set for the time interval 1996.0 and 1996.4. At the slave epoch 1996.4 (orbit 25374), the vertical gradient of the tropospheric contribution is -0.03 mm/m. On the other hand, master epoch 1996.0 (orbit 3697) has a vertical gradient of tropospheric contribution of -0.10 mm/m that corresponds to ~-13 mm range change at the highest point in the Avcılar area. (a) observed fringe pattern. (b) Simulated fringes calculated from the final estimate of model parameters. (c) Residual fringes formed by subtracting the simulated fringes calculated from the prior estimate of the model parameters from the observed fringe pattern. (d) Residual fringes formed by subtracting the simulated fringes calculated from the final estimate of the model parameters from the observed fringe pattern. One colored fringe corresponds to one cycle of phase change, or 28 mm of range change.

Total costs of post-fit models vary between 0.13 and 0.27 cycle/pixel (Figure 3.19). Since the interferograms spanning more than 2 years have more decorrelation problem than others, the post-fit models of these interferograms tend to have higher costs. For example, the total post-fit model costs of pairs 4, 6, 10, 13 and 22 (spanning 3.8, 4.3, 3.2, 3.4, and 3.1 years, respectively) are higher than others. On the other hand, the post-fit model costs of pairs spanning less than 1 year show relatively low values (e.g., pairs 16, 17, 18, 19, and 20).

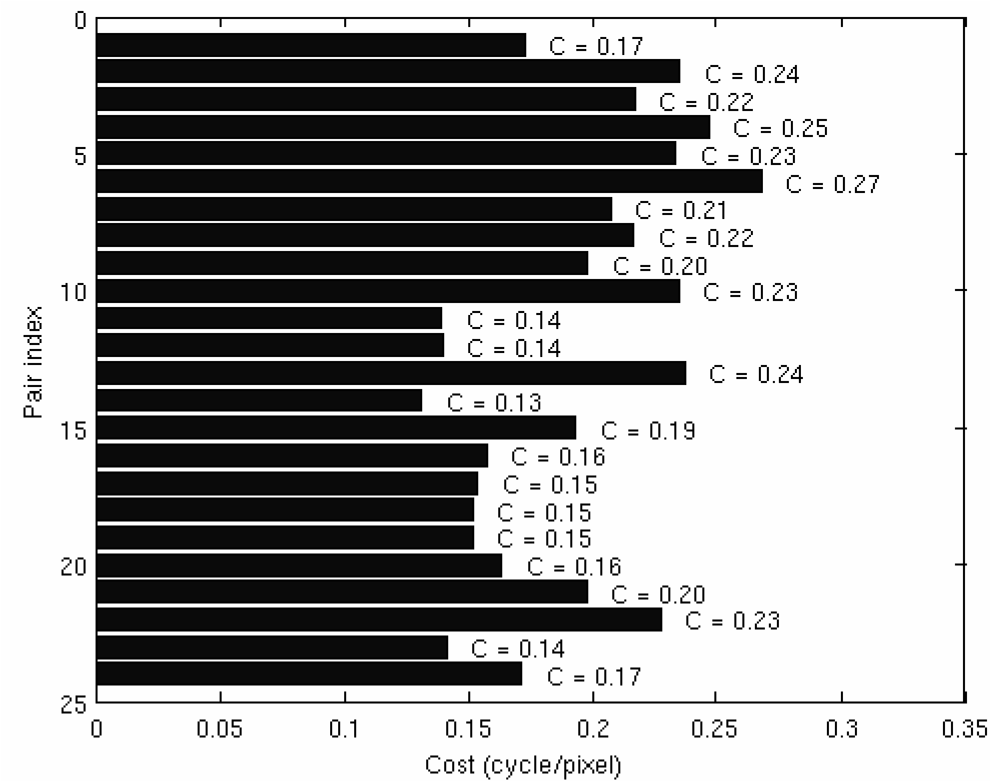

Figure 3.19 : Total costs of post-fit models in the T336/F2783 data set.

3.6.5. Robustness of the model

To verify the robustness of the model parameters, the GIPhT analyses are repeated on two slightly different data sets. First, the number of phase observations varies by changing the PS selection criteria (Table 3.6). Second, two subsets of interferometric pairs, corresponding to species A and B are considered (Table 3.7). In both cases, the same prior values are used. In all of the best-fit models, the “shape” of the range change pattern is fairly similar. The results are compared only in terms of maximum annual vertical displacement.

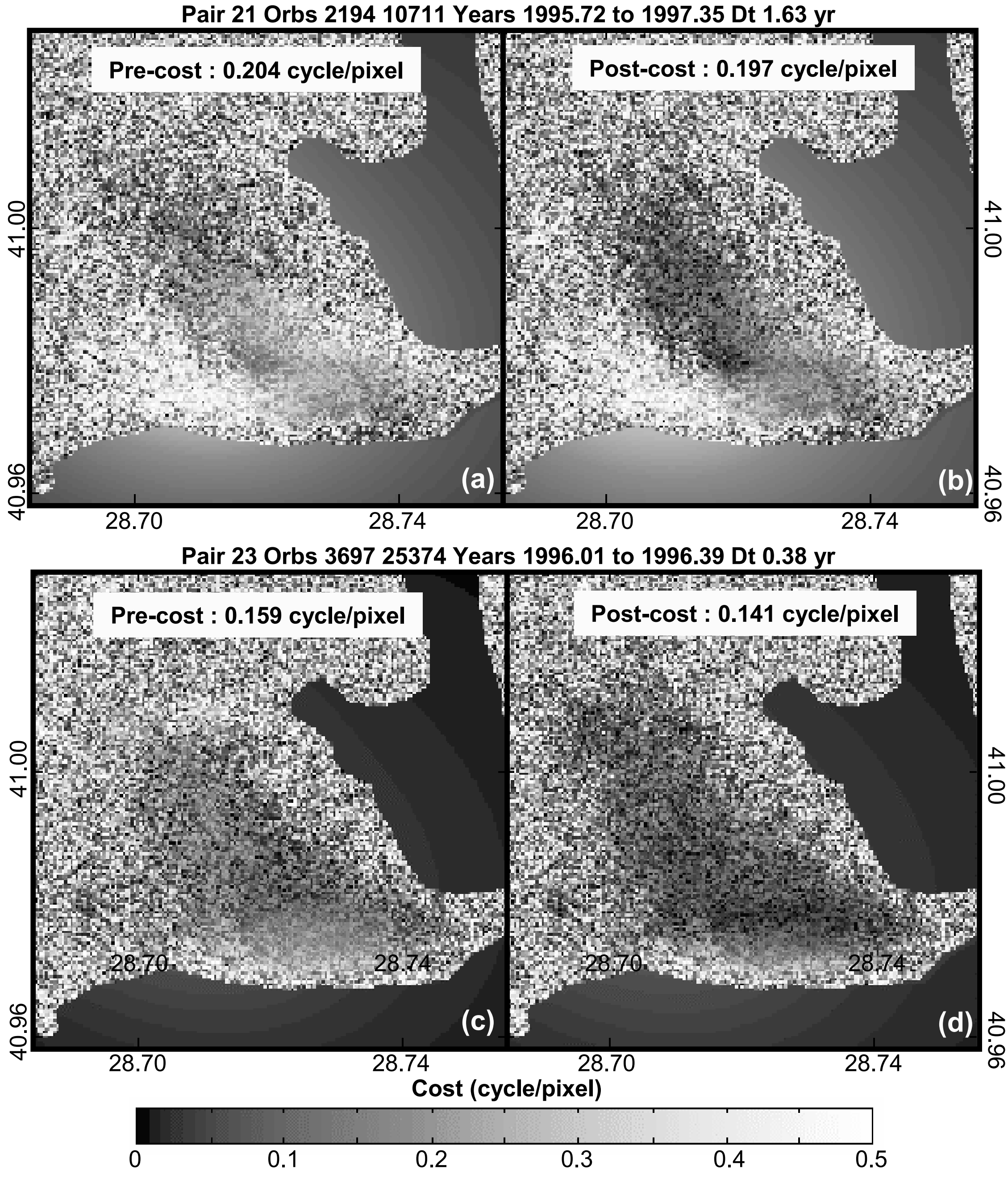

Figure 3.20 : Maps of the marginal cost contributed by individual pixels for four sets of model parameters. Notice that the distribution of low cost pixels (darker colors) increases in the map of final model costs. (a) Prior estimate for the interferogram spanning 1.6 years. (b) Final estimate for the same interferogram. (c) Prior estimate for the interferogram spanning 4.5 months. (d) Final estimate for the same interferogram. One colored fringe corresponds to a cost of half a cycle in phase, or 14 mm in range.

In the first test, the number of data included in the inversion is reduced to 163 by selecting pixels the pixels according to both the amplitude dispersion index D_A<0.25 and the coherence |γ|>0. In this case, the final estimate does not fit the data significantly better than the prior model with 95% confidence.

In the second test, including 16305 pixels in the inversion, the estimated position of the sink shifts horizontally by 380 m. The final model fits the data significantly better than the prior model based on F-test with 95% confidence. The depth of this new Mogi source is 1920 ± 1600 m. Its volume is decreasing at rate of $(-7.60 \pm 4) \times 10^4$ m^3/yr. These geophysical parameters show a range increase of +0.27 cycle/yr that corresponds to a vertical annual displacement of -8 mm/yr at the bottom of the signal pattern. When compared with the vertical annual displacement of 7 mm/yr obtained from 387 pixels (γ|>0.5), we can assume that the values estimated from the both data sets are significantly close. Since these estimates are statistically indistinguishable from those listed in Table 3.6, we infer that the estimation procedure is robust to the choice of pixels.

Tablo 3.6 : Estimate of model parameters according to data points.

PS Criteria	No of pixels	Prior cost	Final cost	F-Test at 95% confidence	Max. range change rate	Max. vertical change rate
|γ|>0.5*	387	0.22	0.21	Significant	+ 0.21 cycle/yr	- 7 mm/yr
D_A<0.25 & |γ|>0.5	163	0.22	0.21	Not significant	+ 0.21 cycle/yr	- 6 mm/yr
All the pixels	16305	0.23	0.22	Significant	+ 0.27 cycle/yr	- 8 mm/yr

**This study*

Although both data sets can be accepted as inversion solutions, in this study the geophysical parameters indicating a maximum displacement rate of -7 mm/yr is accepted. The main reason is that the total final model cost is lower when using the coherence threshold. On the other hand, computing the model parameters with fewer points is more practical since it needs less computation duration.

The analysis is also repeated using two subsets of the data set, corresponding to two species, A and B of interferometric pairs (Table 3.7). The values estimated from specie B is significantly similar from those estimated from the complete data set. Specie A formed by 6 distinct epochs cannot find a model better than the prior model, based on F-test for 95%confidence and overestimates the vertical displacement rate.

Tablo 3.7 : Estimate of model parameters according to interferometric pairs.

Pair selection	No of pairs	No of epochs	Prior cost	Final cost	F-Test at 95% confidence	Max. range change rate	Max. vertical change rate
All the pairs*	24	14	0.22	0.21	Significant	+ 0.21 cycle/yr	-7 mm/yr
Specie A	13	6	0.22	0.21	Not significant	+ 0.29 cycle/yr	- 9 mm/yr
Specie B	11	8	0.22	0.21	Significant	+ 0.18 cycle/yr	6 mm/yr

**This study*

3.7. Discussion

Accounting for the tropospheric effects allows us to map the average rate of vertical displacement (Figure 3.21). To increase confidence in the interferometric results, we compare other geodetic observations carried out in Avcılar district:

1. The distribution of the negative vertical displacement rates shown within the frame A in Figure 3.21 resembles the displacement rates measured by GMES Terrafirma (UKNERC, 2004, Aktar and Browitt, 2006) using a data set that partially intersects that of this study, but a different analysis strategy (e.g., Ferretti et al., 2001) and PS distribution. Although both approaches assume a constant rate of vertical change, this study estimates parameters of a simple geophysical model.

2. A GPS station installed in the east half of the study area following the 1999 earthquakes (P1 in Figure 3.21) indicates an average downward displacement of 12 ± 2 mm/yr (Ergintav, 2006). This value is less than half the 5 mm/yr rate found in this location with InSAR during the time interval 1992-1999.

3. Repeated leveling surveys near Ambarlı Port in the SW corner of the study area (P2 and P3 in Figure 3.21) indicate 11 to 12 mm of vertical subsidence over 30 months (Kalkan et al., 2003), or an average rate of 4 to 5 mm/yr, in very good agreement with the 3-4 mm/yr of vertical motion found in this study using InSAR.

If we had been considering only the interferometric results, we would have concluded that the area of negative vertical displacements was actively subsiding with a constant rate as a result of "compaction". However, no clear evidence of water withdrawal, mechanical loading, drainage network, construction, or hydro-compaction, as described in the introductory chapter, has been found to explain the negative vertical displacement rates. Consequently, an anthropogenic "subsidence" process may not be the main cause of the negative vertical displacement.

When we plot the contours of the vertical change rate on a simplified geologic map (Figure 3.22), we see that the contours of -5 and -6 mm/yr mainly cover the alluvium and the sediments of the Çukurçeşme and Gürpınar formations. The pattern of negative vertical displacement rates (< -5 mm/yr) overlapping the same geological setting is shown in Figure 3.21 with Frame A and B. As described in the introduction of this chapter, the Çukurçeşme and Gürpınar sediments on the 5°-10° slopes are unconsolidated, porous, permeable, saturated, weak, and susceptible to landslides. So, it seems likely that the ground motion around Avcılar interpreted as purely vertical and appearing as subsidence is related to the landslides (Tüysüz, 2007). The presence of active and inactive landslides in the region leads us to propose an interpretation with three main points:

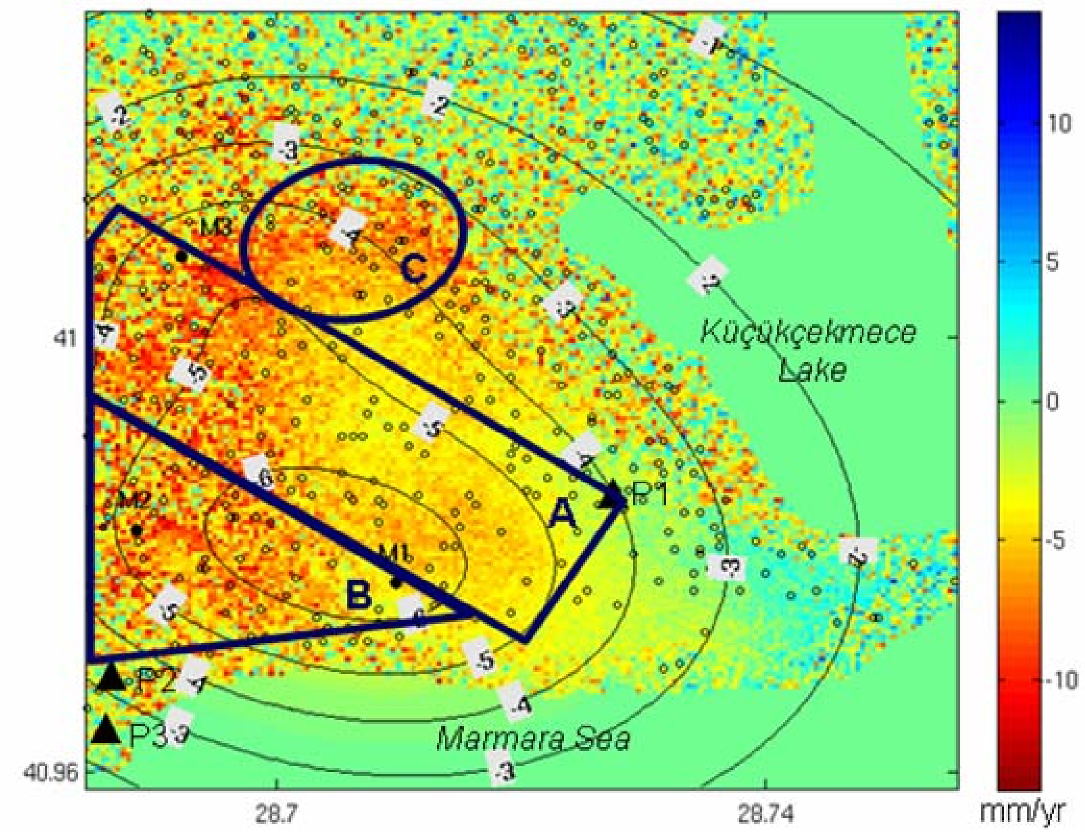

Figure 3.21 : Map of mean rate of vertical displacement in the observed fields. The observed values have been unwrapped using the final model. The black lines are the contour representation of the final model in mm/yr. See the text for the explanation of frames, A, B, and C. P-1 is a GPS point from Ergintav (2006), P-2 and P-3 are leveling points from Kalkan et al. (2003).

1. The change in range (along the line of sight) cannot be uniquely decomposed into the there components (u_n, u_e and u_u) of the displacement vector using a single type of orbital pass (either ascending or descending). Although the ascending and the descending ERS orbits can be used together to resolve a second component of the displacement field (e.g., Wright et al., 2001, Casu et al., 2007), most studies make a simple assumption. This assumption neglects the horizontal components of the line of sight displacement vector and assumes purely vertical displacement since the look angle of the ERS satellite is steep (approximately 23° from vertical) (Figure

3.23). In this study, the vertical displacement rates around Avcılar are interpreted from descending orbits with this approach. Finally, if the constant rate displacements result from landslides, they may have large horizontal components as well. In this case, the vertical displacement rates in Avcılar would be slightly overestimated. It should also be noted that the ESA archive does not provide a sufficient number of ascending ERS orbits covering Avcılar (a total of 15 between 1992 and 2000) for further analysis.

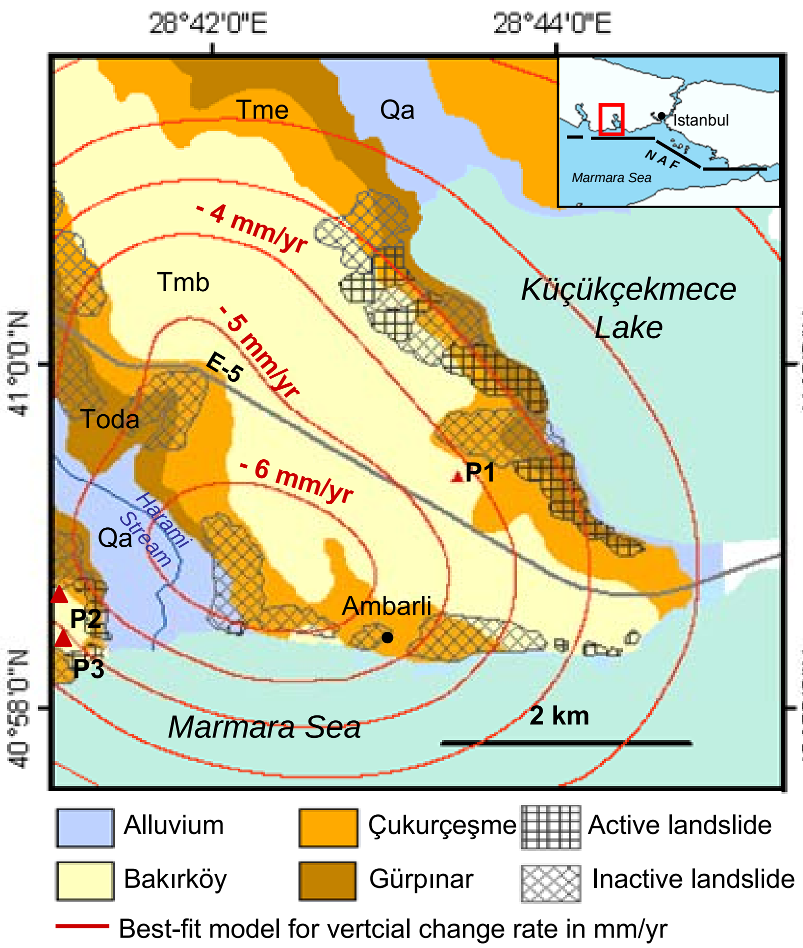

Figure 3.22 : Map showing geological formations and landslides in Avcılar district (from Duman et al., 2005a, Duman et al., 2005b and Alparslan et al., 2006). P1, P2 and P3 are the locations of geodetic surveys from Erginvtav, 2006 and Kalkan et al., 2003.

2. In this study, a constant-rate 3-source Mogi model is used to describe the ground motion in Avcılar between 1992 and 1999. This approach does not aim to detect rapidly occurring or discontinuously moving landslides. For this reason, we do not see transient deformation signals such as those that would be produced by any significant vertical displacement rates in the active landslide areas along the coasts of Marmara Sea and Küçükçekmece Lake (as reported by e.g. Örmeci (1972),

Ergintav (2006), Kalkan et al. (2003)). On the other hand, the inactive landslides along the slopes of Harami Stream valley coincide with the areas of high downward displacement rates (Frame A and B in Figure 3.21). These dormant landslides surrounding the Harami stream valley have not shown any significant activity for a long time according to the study of Duman et al. (2004). So, it seems likely that the material once displaced on the slopes of Harami Stream after a series of landslides has been gradually sliding and settling down (Figure 3.23). This is why the constant-rate time dependence explains the ground motion in the inactive landslide area better than in the active landslide area. Also, since most (two-third) of the epochs used for inversion are from the dry season, they miss the times when the landslides occur. This is another reason why the distribution of vertical displacement rates do not show any significant pattern indicating the locations of the main body, the head or the toe of the landslides.

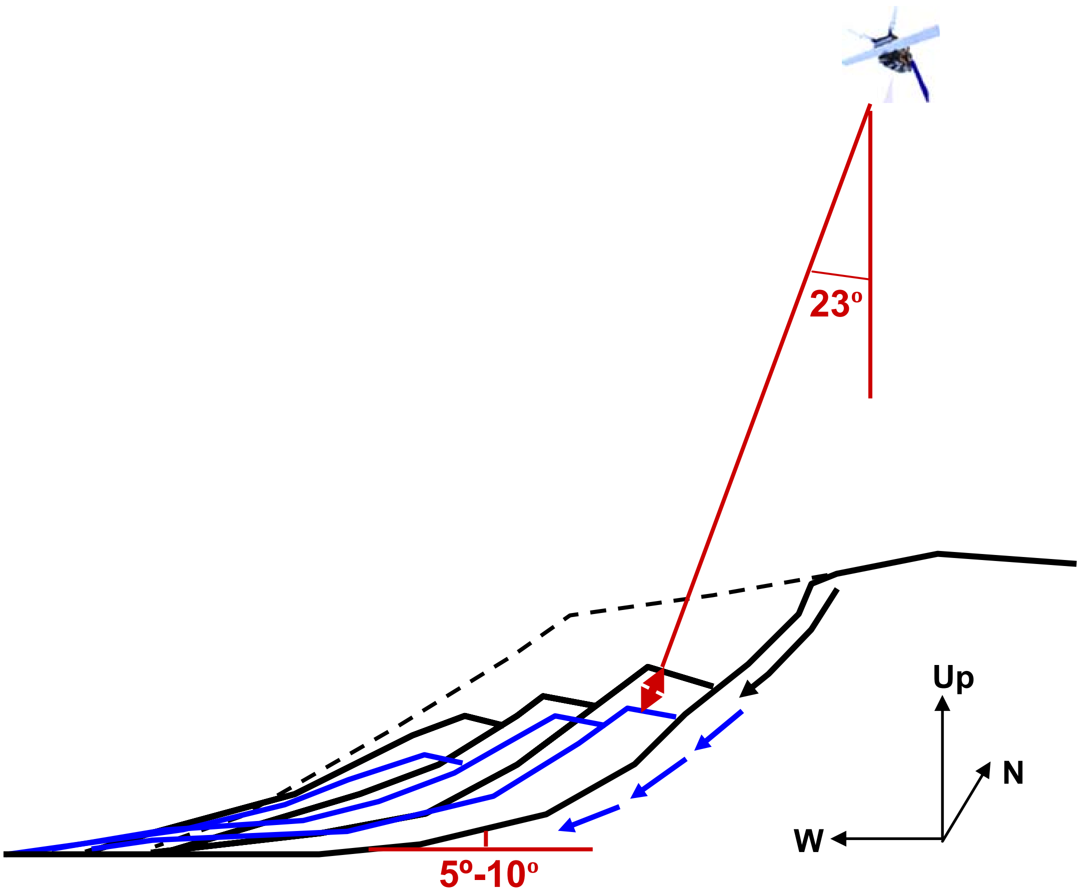

Figure 3.23 : Gradual ground movement (in blue) after a landslide activity (in black) measured by ERS satellite. The sketch represents the soils on the slopes of Harami stream valley gradually moving away from the descending ERS orbit.

Although the constant-rate 3-source Mogi model explains the first-order features of the interferometric data set well in the inactive landslide areas, some second-order features remain to be explained. For example, in one of the interferograms we see a transition in the fringe pattern between red and light blue (the black circle in Figure 3.24), indicating an increase in range of 0.6 cycles in 2.65 years. Assuming purely vertical motion at a constant-rate, we find approximately 6 mm/yr of vertical change, twice the value calculated from the model at that location. A similar fringe pattern appears in three other interferograms (see interferograms 13, 15, and 16 in Appendix B) spanning different time intervals between 1993 and 1995. Therefore a landslide might have occurred in this area, close to Ambarlı town, a district by the Marmara seacoast with a history of landslides, sometime between 1993 and 1995. The common fringe pattern in four of the interferograms suggests a more complicated process than the assumed constant-rate model.

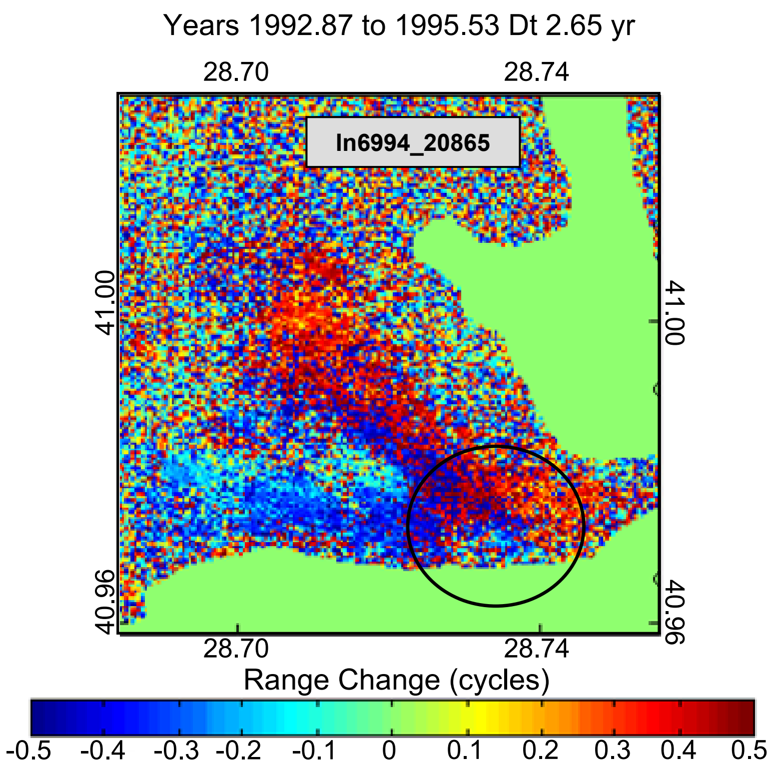

Figure 3.24 : A data pair (pair no 2 in Table 3.3) spanning the time interval between 1992.87 (orbit 6994) and 1995.53 (orbit 20865). See the text for the explanation of the black circle.

3. If the ground deforms more rapidly during the wet season than during the dry season, then the time dependence of the motion might resemble a periodic function. In this case, constant time dependence can be combined with periodic time dependence. However, inversion from such a model will be very difficult to solve because of two reasons. First, the temporal decorrelation during the wet season may decrease the number of observations (i.e., number of point targets and interferometric data pairs). Second, the range change due to periodic displacements

may be very small to distinguish from the range change due to tropospheric contributions during the wet season. In this study, the data set produces a limited amount of observation to model ground deformation with periodic time dependence because only one third of the epochs used in the inversion are from the wet season. Also the examination of the data pairs spanning mixed seasons (10 of 24 data pairs) has revealed no evidence of periodic ground motion.

Although high negative displacement rates are explained with the landslide susceptibility in Avcılar, some areas remain unexplained. We see a pattern of high downward vertical displacement rates on the north side of the map above E5 highway (Frame C in Figure 3.21). This area consisting of mainly Bakırköy formation has not been associated with any landslide activity (according to the geological map of Duman et al. (2004)). Also, the residuals (black circle in Figure 3.25) show that downward vertical displacement rate in this particular area is 2 to 3 mm/yr faster than calculated from the model. It seems that ground motion in this area is poorly described by the simple model for volume change at depth.

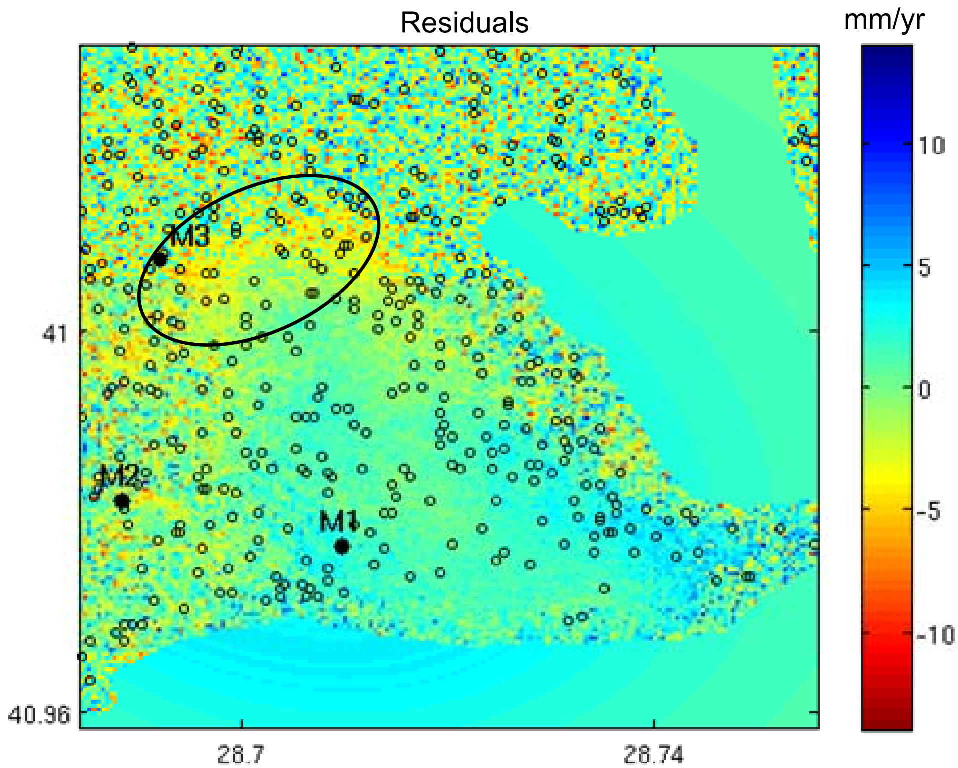

Figure 3.25 : Map of residual fields. The black lines are the contour representation of the final model showing annual rate of vertical displacement in mm/yr. Black circle is to emphasize high residual fields.

In this study, a constant rate 3-source Mogi model is used to explain the common features of the interferometric data set. This model consists of three identical sources located at certain depth changing volume with constant rate. Although this geophysical model fits the interferometric observations well, it explains the landslide process indirectly. There are two reasons. First, the model assumes constant displacement rates which actually explains a steady ground movement in the landslide area. Second, the geometric distribution of the volume decrease is certainly more complicated than the three Mogi sources assumed in this study. Accordingly, the final estimate of the Mogi depth may be too deep. In this case, the estimated reduction in volume may be too large because of the trade-off between these two parameters. Although these features are more appropriate to describe, for example, evolution of a subsidence bowl, we see that this approach can still provide valuable information about the weak ground conditions in Avcılar. Finally, precise ground truth collected from the sites showing high downward displacement rates can be useful to improve the geophysical parameters and the time dependence of the model.

The Çukurçeşme and Gürpınar sediments on the 5^{o}-10^{o} slopes of Harami stream valley are susceptible to landslides. Although Duman et al. (2004) show this area as an inactive landslide area, the vertical displacement rates measured by radar interferometry suggest a continuous downward ground motion (with a max of 7 mm/yr) between 1992 and 1999. If these unconsolidated soils on the Harami Stream slopes are more saturated in the wet season, these soils might also be susceptible to soil liquefaction during an earthquake in a wet season. As described in the introductory chapter, the flow failures, a type of soil liquefaction, is comprised of intact material riding on a layer of liquefied soil. Flow failures develop on slopes greater than 3° and may cause severe damage to constructions by shifting soil masses for long distances during earthquake shaking (Tinsley et al., 1985). Consequently, the soils on the slopes of Harami stream valley showing fast downward ground motion may experience flow failures especially if the earthquake is occurring in a rainy season. Then, the map of vertical ground motion can provide valuable insight into earthquake hazard preparedness in Avcılar county.

4. CONCLUSIONS

This thesis was concerned with mapping ground motion in an urban environment using satellite radar interferometry. Following the objectives of the thesis;

a) New techniques in mapping deformation by InSAR has been mastered. The General Inversion for Phase Technique (GIPhT) developed by Feigl and Thurber (2007) has been practiced to measure ground motion occurring with a constant rate. A large set of interferograms were reduced to a reliable subset of phase observations using the techniques since 2000 (e.g., Ferretti et al., 2000, Ferretti et al., 2001, Lyons et al., 2002, Colesanti et al., 2003).

(b) A strategy for measuring slow and long-term ground motion has been established. ESA's ERS satellites radar data archive was searched for the best interferometric pairs. DIAPASON software (Massonnet et al. , 1994 ; CNES, 1998, CNES, 2006) was used with full capacity to process raw SAR data. New tools were developed for interpreting interferograms.

c) Ground motion in the Avcılar district of İstanbul was measured. Analysis of SAR images acquired by ERS satellites between 1992 and 1999 revealed vertical displacement rate of maximum 7 mm/yr at a point located at latitude 40.98ºN and longitude 28.71ºE (Akarvardar et al., 2007). The ground motion was interpreted as pure vertical because of the steep looking angle of the ERS satellite. No clear evidence of compaction induced subsidence was found to explain the ground motion. Harami Stream valley that has been known as a landslide area showed high downward displacement rates. The pattern of negative vertical displacement rates (< -5 mm/yr) coincided the alluvium and the weak sediments of the Çukurçeşme and Gürpınar formations that are susceptible to landslides.

(d) The physical model of ground motion was described. A simple 4-parameter elastic Mogi model consisting of three infinitesimal spherical sinks at a depth of 2300 ± 1300 m deflating at 78 ± 34 thousand cubic meters per year described interferometric signal to first order. The model also accounted for tropospheric effects for each image acquisition epoch. Although the final depth and the volume change of the model were found to be large in the data inversion, it explained slow and long-term ground motion in the Harami Stream valley well.

(e) The contribution of ground motion to managing seismic risk was evaluated. The fast downward ground motion on the slopes of Harami Stream valley has suggested that this area might be susceptible to soil liquefaction during the wet season and the flow failures were more likely to occur.

Further research should consider the following details:

1. A simple model that generalizes the 3-dimensional components of the line of sight displacement vector was used in this study. This model assumed purely vertical displacement. If the ground motion in Avcılar is associated with landslide processes, the horizontal components of the displacement should be considered. Although ERS cannot provide sufficient number of scenes for the temporal adjustment, conventional INSAR methods based on individual data pairs can be helpful. ENVISAT satellite launched in 2002 provides the continuity of the ERS satellites. Interferometric phase measurements from ENVISAT-ASAR may be integrated to enhance the results obtained in this study. Although ENVISAT-ASAR cannot provide >30 image epochs from the same data frame to obtain reliable phase observations as proposed by Ferretti et al. (2000), again conventional INSAR methods can be applied to individual ENVISAT data pairs. Also, other radar data acquired by the Japanese L-Band ALOS satellite that was launched in 2005, the Canadian C-Band RADARSAT satellite that has been operating since 1995 can be used in further studies.

2. The geophysical model used in this study does not aim to detect and map landslides. Another model is needed to describe the relationship between the vertical ground motion and the landslide occurrences. This model will require a more complex time dependence and source mechanism.

3. Ground truth from the areas showing high vertical displacements is crucial. A collaboration with other organizations investigating the same region (e.g., ELC, 2005; Ergintav, 2007) may lead us to better evaluate the probable hazard risks.

Considerable part of this thesis duration was spent for data selection. As a consequence of the nature of InSAR technique (i.e. decorrelation), it may be very difficult to find and determine high quality interferometric pairs in the ERS data archive for a certain area. In this study, I had to eliminate the SAR image epochs of the co-seismic and post-seismic period of the 1999 Izmit Earthquake from the whole ERS data set (i.e., 48 images, 1128 interferometric pairs (C_2^{48} = 48x47/2)) since the study area, Avcılar district, was severely affected by the earthquake. Finally, 30 image epochs between 1992 and 1999 remained. As described in detail in the previous chapters, 14 high quality interferometric pairs were used in the ground motion analysis. This means that only the 1% of the T336/2783 data set was used for deformation analysis. As a conclusion, data selection is one of the crucial steps in mapping slow motion deformation.

The GIPhT technique (Feigl & Thurber, 2007) used in modeling the phase observations is advantageous from many ways. First, unwrapping the phase observations is not necessary, the technique adjusts the model parameters based on wrapped phase values. Second, it uses a simple method that adjusts the model parameters rather than individual pixel values. However, there are some points to consider while using GIPhT. For example, a PS coverage of 3 PS/km^2 could not provide enough number of phase observations to model the 14 interferograms. I had to increase the density of points to 7 PS/km^2 by neglecting the "amplitude dispersion index" criteria. On the other hand, one has to have some prior knowledge of the deformation to determine the prior model parameters. It may be difficult to observe the deformation signal from the noisy interferograms.

In this study, a strategy to measure ground motion by ERS radar interferometry has been developed. Furthermore, the map of vertical displacement rates in the Avcılar district of İstanbul between 1992 and 1999 has been produced using this strategy. Determining negative vertical displacement rates is crucial for evaluating earthquake damage risk in the landslide areas of Avcılar county. A similar strategy can be applied to İstanbul metropolitan area that is located close to the seismic gap in the Marmara Sea.

REFERENCES

Adam, N., Kampes, B., Eineder, M., Worawattanamateekul, J., Kircher, M., 2003. The development of a scientific permanent scatterer system, *ISPRS Workshop Proceedings*, Hannover 2003.

Akarvardar, S., Feigl, K., Ergintav, S., 2007. Subsidence in the Avcilar district of Istanbul, Turkey measured by satellite radar interferometry1992-1999, *Geophysical Journal International , (submitted in 2007)*

Aktar, M., Browitt, C., 2006. Vulnerability Mapping Istanbul, *GMES Terrafirma Workshop 3*, Conference, Location, 18-19 May 2006

Akyüz, H., S., Hartleb, R., Barka, A., Altunel, E., Sunal, G., Meyer, B., Armijo, R., 2002. Surface Rupture and slip distribution of the 12 November 1999 Düzce Earthquake (M 7.1) North Anatolian Fault, Bolu, Turkey, *Bull. Seism. Soc. Am.*, **92**, pp. 61-66.

Allen, S.A., 1984. Types of land subsidence, in *Guidebook to Studies of Land Subsidence Due to Groundwater Withdrawal*, pp. 133–142, Ed. Poland, J.F. UNESCO, Paris, 1984.

Alparslan, E., Yüce, H., Erkan, B., İnan, S., Ergintav, S., Saatçılar, R. , 2006. Multi-Criteria Analysis of Landslides Susceptibility in the Area between the Buyukcekmece and Kucukcekmece Lakes of Istanbul City Using Remote Sensing and GIS (in Turkish) *The 4th of GIS Days*, Conference, Location, September 13-16

Ambraseys, N., 2002. The Seismic Activity of the Marmara Sea Region over the Last 2000 Years, *Bull. Seismol. Soc. Am.*, **92(1)**, pp. 1-18, 2002.

Amelung, F., Galloway, D.L., Bell, J.W., Zebker, H.A., Laczniak, R.J., 1999. Sensing the ups and downs of Las Vegas: InSAR reveals structural control of land subsidence and aquifer-system deformation, *Geology*, **27**, pp. 483-486.

Ansal, A., Bardet, J.P., Bray, J., Cetin, O., Durgunoğlu, T., Erdik, M., Kaya, A., Ural, D., Yılmaz, T., Youd, L., 1999. Initial Geotechnical Observations of the August 17, 1999, Izmit Earthquake, *A Report of the Turkey-US Geotechnical Reconnaissance Team*, [http://nisee.berkeley.edu/turkey/report.html#], National Information Service for Earthquake Engineering, University of California, Berkeley, September 3, 1999

Armijo, R., Meyer, B., Hubert-Ferrari, A., Barka, A.A. , 1999. Westward propagation of the North Anatolian fault into the northern Aegean: Timing and kinematics, *Geology*, **27**, pp. 267– 270.

Aryal, A., Calais, E., Haase, J, Feigl., K., 2004. Radar Interferometry Reveals Underground Salt Leaching of Anthropogenic Origin in a Saharan Oilfield, *American Geophysical Union Fall Meeting*, Conference, Location, 13-17 December 2004, AGU.

ASAR-SAG, 1998. ENVISAT ASAR Science & Applications, *ESA Publications Division SP-1225*, ASAR Science Advisroy Group, Earth Sciences Division, ESA, Ed. Attema, E.

Attema, E., 1998. Envisat ASAR Science and Applications, ESA SP-1225, ESA Publications Division, the Netherlands, November 1998.

Bamler, R., & Hartl, P., 1998. Synthetic aperture radar interferometry, *Inverse Problems*, **14**, pp. 1–54.

Bardet, J.P., Kapuskar, M., 1993. Liquefaction Sand Boils in San Francisco during 1989 Loma Prieta earthquake, *J. Geotech. Engrg.*, **119 (3)**, pp. 543-562, March, 1993.

Barka, A., Kadinsky-Cade, K., 1988. Strike-slip fault geometry in Turkey and its influence on earthquake activity, *Tectonics*, **7**, pp. 663-684.

Barka, A., 1996. Slip distribution along the North Anatolian fault associated with the large earthquakes of the period 1939-1967, *Bull. Seism. Soc. Am.*, **86**, pp. 1238-1254.

Barka, A., 1999. The 17 August 1999 Izmit earthquake, *Science*, **285**, pp. 1858-1859.

Barka, A., Akyüz, S., H., Altunel, E., Sunal, G., Çakır, Z., Dikbaş, A., Yerli, B., Armijo, R., Meyer, B., de Chabalier, J., B., Rockwell, T., Dolan, J., R., Hartleb, R., Dawson, T., Christofferson, S., Tucker, A., Fumal, T., Langridge, R., Stenner, H., Lettis, W., Bachhuber, J. and Page, W., 2002. The Surface Rupture and Slip Distribution of the 17 August 1999 Izmit Earthquake M=7.4, North Anatolian Fault, *Bull. Seism. Soc. Am.*, **92**, pp. 43-60.

Barka , A.A., 1992. The North Anatolian Fault, *Anneles Tectonicae*, **(6)**, pp. 164-195.

Bawden, G.W., Thatcher, W. , Stein, R.S., Hudnut, K.W., Pletzer, G. , 2001. Tectonic contraction across Los Angeles after removal of groundwater pumping effects, *Nature*, **412**, pp. 812-815, 2001.

Beauducel, F., Briole, P., Froger, J.L., 2000. Volcano wide fringes in ERS SAR interferograms of Etna: Deformation or tropospheric effect?, *Journal of Geophysical Research*, **105(B7)**, pp. 16,391-16,402, July 2000.

Bock, Y., & Williams S., 1997. Integrated Satellite Interferometry in Southern California, *Eos, Trans., AGU*, **78(29)**, pp. 293,299-300.

Bovenga, F., Refice, A., Nutricato, R., Pasquariello, G., De Carolis, G., 2002. Automated calibration of multi-temporal ERS SAR data, *Geoscience and Remote Sensing Symposium, 2002. IEEE International IGARSS*, Vol. 6, pp. 3655 - 3657, Toronto, Canada, 24-28 June 2002.

Burgman, R., Rosen, P.A., & Fielding, E.J., 2000. Synthetic Aperture Radar Interferometry to Measure Earths Surface Topography and Its Deformation, *Annu. Rev. Earth Planet. Sci.*, **28**, pp. 169–209.

Burland, J., Jamiolkowski, M., Viggiani, C. , 2002. Preserving Pisa's Treasure, *Civil Engineering Magazine*, March 2002.

Casu, F., Solaro, G., Pepe, S., Lundgren, P., Manzo, M., Pepe, A., Berardino, P., Sansosti, E., Lanari, R., 2007. Fifteen years of ERS and ENVISAT DINSAR observations at Mt. Etna, Italy, by Using the SBAS Approach, *Advances in SAR Interferometry from ENVISAT and ERS missions, Fringe 2007,* 26-30 November, 2007, ESA-ESRIN, Franscati, Rome, Italy.

Çağatay, I., H., 2005. Experimental evaluation of buildings damaged in recent earthquakes in Turkey, *Engineering Failure Analysis*, **12**, pp. 440–452, 2005.

Çakır, Z., 2003. Analysis of the crustal deformation caused by the 1999 Marmara earthquake sequence using synthetic aperture radar Interferometry, *PhD. Thesis*, Geological Engineering Dep., Institute of Sciences and Technology, Istanbul Technical University, Turkey and Département de Tectonique et Mecanique de la Lithosphere, Institut de Physique du Globe de Paris, France,

Çakır, Z., de Chabalier, J.B., Armijo, R., Meyer, B., Barka, A. and Peltzer, G., 2001. The August 17, 1999 Turkey Earthquake seen with InSAR Imagery and Tectonic Field Observations, *EUG XI Meeting*, Conference, Location, 2001,

Canby, T., 1990. Earthquake: Prelude to the Big One?, *National Geographic*, **177(5)**, May 1990.

Carbognin, L., 2003. Overview of the Activity of the UNESCO-IHP Working Group IV Project M-3.5 (C) On land Subsidence, *International Hydrological Programme, Division of Water Sciences*, UNESCO, 2003.

Carnec, C., Fabriol H., 1999. Monitoring and modeling land subsidence at the Cerro Prieto geothermal field, Baja California, Mexico using SAR interferometry, *Geophysical Research Letters*, **26(9)**, pp. 1121-1214, May 1, 1999

Carnec, C., Massonnet, D., King, C., 1996 Two examples of the use of SAR interferometry on displacement fields of small spatial extent, *Geophysical Research Letters*, **23(24)**, pp. 3579-3582, December 1, 1996.

Cervelli, P., Murray, M.H., Segall, P., Aoki, Y. & Kato, T., 2001. Estimating source parameters from deformation data, with an application to the March 1997 earthquake swarm off the Izu Peninsula, Japan, *Journal of Geophysical Research*, **106**, pp. 11217-11237.

Cetin, K.O., Youd, T.L., Seed, R.B., Bray J.D., Sancio , R., Lettis, W., Yilmaz, M.T., Durgunoglu, H.T., 2002. Liquefaction-induced ground deformations at Hotel Sapanca during Kocaeli (Izmit),Turkey earthquake, *Soil Dynamics and Earthquake Engineering*, **22(2002)**, pp. 1083–1092.

Çetin, K.O., Isik, N., Unutmaz, B., 2004. Seismically induced landslide at Degirmendere Nose, Izmit Bay during Kocaeli (Izmit)-Turkey earthquake, *Soil Dynamics and Earthquake Engineering*, **24(2004)**, pp. 189–197.

Closset, L. and King, C. 2005. ESA GMES TERRAFIRMA U8-Core User group Executive report, version 2, January 27, 2005.

CNES, 1998. Philosophy & Instructions for use of DIAPASON: Interferometry Software System Developed at CNES, 15 December 1998.

CNES, 1998. Philosophy & Instructions for use of the DIAPASON, Interferometry Software System, CNES, January 15,1998.

CNES, 2003. Automated Interferometric Processing Software DIAPASON, User's Guide, Issue 3.1, Toulouse Space Center Sub-Directorate Observation de la Terre, Space Image Quality and Processing Division, Radar Systems Department, French Space Agency (CNES), Distributed by ALTAMIRA INFORMATION, SL, November 2003.

Colesanti, C., Ferretti, A., Prati, C., Rocca, F., 2003. Monitoring Landslides and Tectonic Motions with Permanent Scatterers Technique, *Engineering Geology*, **68**, pp. 3-14, 2003.

Colesanti, C., Ferretti, A., Novali, F., Prati, C., Rocca, F, 2003. SAR monitoring of progressive and seasonal ground deformation using the permanent scatterers technique, *IEEE Transactions on Geoscience and Remote Sensing*, **41 (7)**, pp. 1685 – 1701, 2003.

Corpus, J.A., 1998. TSPIMAN A Symmetric 2D Euclidian Traveling Salesman Problem (TSP): Nearest Neighbor tour construction + 2-Opt local search + Simulated Annealing/Metropolis test, developed using MATLAB v5., Dept. of Mathematics, Graduate Studies, University of the Philippines, Diliman, Manila.

Curlander, J.C., McDonough, R.N. , 1991. Synthetic aperture radar systems and signal processing, John Wiley & Sons, New York.

Dehls, J.F., Basilico, M., Colesanti, C., 2002. Ground deformation monitoring in the Ranafjord area of Norway by means of the Permanent Scatterers technique, *IEEE International Geoscience and Remote Sensing Symposium, IGARSS 2002*, pp. 1, 203-1,207.

Delacourt, C., Briole, P., Achache, J., 1988. Tropospheric corrections of SAR interferograms with strong topography: Application to Etna, *Geophys. Res. Lett.*, **25(15)**, pp. 2849-2852, August 1, 1998.

Duman, T., Y., Can, T., Ulusoy, R., Kecer, M., Emre, O., Ates, S., Gedik, I., 2005a. A Geohazard reconnaissance study based on geosceintific information for development needs of the western region of Istanbul (Turkey), *Environmental Geology*, **48**, pp. 871-888, 2005.

Duman, T., Y., Kecer, M., Ates, S., Emre, O., Gedik, I., Karakaya, F., Durmaz, S., Olgun, S., Sahin, H., Gokmenoglu, O., 2004. Geological Data of Urban Development Areas (Kucukcekmece – Silivri - Catalca

Vicinities) in the western of Istanbul Metropolitan Municipality (in Turkish), *MTA, Special Publication*, 3, 249, MTA, Ankara, Turkey.

Duman, T., Y., Can, T., Gokceoglu, C. and Nefeslioglu, H., A., , 2005b. Landslide susceptibility mapping of Cekmece area (Istanbul, Turkey) by conditional probability, *Hydrology and Earth System Sciences Discussions*, **2**, pp. 155-208, 2005.

EDMRM, 2000. The 1999 Turkey Earthquake Report, Volume 1: Kocaeli, Turkey Earthquake of August 17, 1999, *EDM Technical Report*, No. 6 Earthquake Disaster Mitigation Research Center, The Institute of Physical and Chemical Research (RIKEN), Miki, Hyogo Prefecture, Japan, August 2000.

Elachi, C., 1987. Introduction to the Physics and Techniques of Remote Sensing, pp. 413-415, John Wiley & Sons, New York.

ELC, 2005. Vulnerability assessment to land movements in the south of Ambarli district of Avcilar County of Istanbul (inTurkish), ELC Group Musavirlik ve Muhendislik, Istanbul.

Ergin, M., Özalaybey, S., Aktar, A., Yalcin, M., N., 2004. Site amplification at Avcilar, Istanbul, *Tectonophysics*, **391**, pp. 335–346, 2004.

Ergintav, S., 2006. Personnel communication.

Feigl, K.L., Gasperi, J., Sigmundsson, F., Rigo A.,, 2000. Crustal deformation near Hengill volcano, Iceland, 1993-1998: Coupling between magmatic activity and faulting inferred from elastic modeling of satellite radar interferograms., *J. Geophys. Res.*, **105 (B11)**, pp. 25655-25670.

Feigl, K.L., Sarti, F., Vadon, H., Durand, P., Mclusky, S., Ergintav, S., Burgmann, R., Rigo, A., Massonnet, D., and Reilinger, R., 2002. Estimating slip distribution for the Izmit mainshock from coseismic GPS, ERS-1, RADARSAT and SPOT measurements, *Bull. Seism. Soc. Am.*, **92**, pp. 138-160, 2002.

Feigl, K.L., 2003. Estimating Earthquake Source Parameters from Geodetic Measurements, Chapter 37, in *International Handbook of Earthquake and Engineering Seismology Part A*, Vol. 81A, p. 611, Ed. Lee, W.H.K., Kanamori, H., Jennings, P. and Kisslinger, C., Elsevier, 2003.

Feigl, K.L., & Thurber C.H., 2007. A technique for modeling radar interferograms without phase unwrapping: Application to the M 5 Fawnskin, California earthquake of 4 December 1992, *Geophys. J. Int. (submitted in 2007)*.

Ferretti, A., Prati, C., Rocca, F., 2000. Non-linear Subsidence Rate Estimation Using Permanent Scatterers in Differential SAR Interferometry, *IEEE Trans. on Geoscience and Remote Sensing*, **38(5)**, pp. 2202- 2212, September 2000

Ferretti, A., Prati, C., Rocca, F.,, 2001. Permanent Scatterers in SAR Interferometry,, *IEEE Trans. on Geoscience and Remote Sensing*, **39(1)**, pp. 8-20, January 2001.

Fialko, Y., Simons, M., 2000. Deformation and seismicity in the Coso geothermal area, Inyo County, California: Observations and modeling using satellite radar interferometry, *Journal of Geophysical Research*, **105(B9)**, pp. 21781-21793, September 10, 2000.

Fialko, Y., 2004. Evidence of fluid-filled upper crust from observations of postseismic deformation due to the 1992 Mw 7.3 Landers earthquake, *Journal of Geophysical Research (Solid Earth)*, **109**, p. 08401.

Field, N., Jones, L., Jordan, T., Benthien, M., Wald, L., 2001. Earthquake Shaking: Finding the “Hotspots”, Fact Sheet 001–01, USGS, 2001.

Fielding, E.J., Blom, R.G., Goldstein, R.M. , 1998. Rapid subsidence over oil fields measured by SAR interferometry, *Geophysical Research Letters*, **25(17)**, pp. 3215–3218, 1998.

Gabriel, A.K., & Goldstein, R.M., 1988. Crossed orbit interferometry: Theory and experimental results from SIR-B, *Int. J. Remote Sens.*, **9**, pp. 857–872.

Gabriel, A.K., Goldstein, R.M. and Zebker, H.A., 1989. Mapping small elevation changes over large areas: Differential radar interferometry, *J. Geophys. Res.*, **94**, pp. 9183-9191.

Gabrysch, R.K., 1984. Case History No. 9.12. The Houston-Galveston Region, Texas, U.S.A., in *Guidebook to Studies of Land Subsidence Due to Groundwater Withdrawal*, pp. 253–262, Ed. Poland, J.F. UNESCO, Paris, 1984.

Galloway, D.L., Hudnut, K.W., Ingebritsen, S.E., Phillips, S.P., Peltzer, G., Rogez, F., Rosen, P.A. , 1998. Detection of aquifer system compaction and land subsidence using interferometric synthetic aperture radar, Antelope Valley, Mojave Desert, California, *Water Resources Research*, **34(10)**, pp. 2573–2585, October 1998.

Gambolati, G., Teatini, P., Ferronato, M., 2005. Anthropogenic Land Subsidence, Chapter 158, in *Encyclopedia of Hydrological Sciences*, Vol. 4, pp. 2444-2459, Ed. Anderson, M.G. John Wiley & Sons Ltd, 2005.

Gasperi, J., 1999. Etude de la deformation lithospherique active par interferometrie radar. Application a la region de Hengill, Islande, University Paul Sabatier, Toulouse, France, 1999.

Gens, R., & Van Genderen, J.L., 1996. SAR interferometry : Issues, Techniques, Applications, *Int. J. Remote Sens.*, **17**, pp. 1803–1835.

Goldstein, R., 1995. Atmospheric limitations to repeat-pass interferometry, *Geophys. Res. Lett.*, **22**, pp. 2517–2520, September 1995.

Goldstein, R.M., & H. A. Zebker, 1987. Interferometric radar measurent of ocean surface currents, *Nature*, **328**, pp. 707–709.

Goldstein, R.M., Zebker, H.A., & Werner, C.L., 1988. Satellite Radar Interferometry: Two dimensional Phase Unwrapping, *Radio Science*, **23**, pp. 4, 713-720.

Goldstein, R.M., & Werner, C.L. , 1998. Radar Interferogram Filtering for Geophysical Applications., *Geophysical Research Letters*, **25(21)**, pp. 4035-4038.

Graham, L.C., 1974. Synthetic interferometer radar for topographic mapping, *Proceedings of IEEE*, **62**, pp. 763–768.

Grant, W.P., Perkins, W.J., Youd, T.L., 1992. Evaluation of liquefaction potential, Seattle, Washington, *U. S. Geological Survey Open-File Report*, No 91-441-T, 1992.

Hanssen, R., & Usai, S.,, 1997. Interferometric Phase Analysis for Monitoring Slow Deformation Processes, *The 3rd ERS Symposium: Space at the Service of Our Environment.*, Conference, Location, March 14-21,1997,

Hanssen, R.F., Weckwerth, M., Zebker, H.A., Klees, R., 1999. High resolution water vapor mapping from interferometric radar measurements, *Science*, **283(1)**, pp. 297-1299, February 26, 1999.

Hanssen, R.F., 2001. Radar Interferometry Data Interpretation and Error Analysis, Kluwer Academic Publishers, The Netherlands.

Henderson, F.M., Lewis. A.J., 1998. Manual of Remote Sensing, Third Edition, Volume 2, Ed. Ryerson, R.A., Published in Co-operation with The American Society for Photogrammetry and Remote Sensing and John Wiley & Sons Inc.

Hoffmann, J., Zebker, H.A., Galloway, D.L., Amelung, F., 2001. Seasonal subsidence and rebound in Las Vegas Valley, Nevada, observed by synthetic aperture radar interferometry, *Water Resources Research*, **37(6)**, pp. 1551-1566, June 2001.

Holzer, T.L., Noce T.E., Bennett, J.M., Alessandro, C.D., Boatwright, J., Tinsley, J.C., Sell, R.W., Rosenberg, L. I., 2004. Liquefaction induced lateral spreading in Oceano, California, during the 2003 San Simeon earthquake, *U. S. Geological Survey Open-File Report*, No 2004–1269.

Hooper, A., Zebker, H., Segall, P., Kampes, B. , 2004. A new method for measuring deformation on volcanoes and other natural terrains using InSAR persistent scatterers, *Geophysical Research Letters*, **31 (23)**, pp. 5, doi:10.1029/2004GL021737, 2004.

Hooper, A.J., 2006. Persistent Scatterer Radar Interferometry For Crustal Deformation Studies and Modeling of Volcanic Deformation, Ph.D Thesis, Stanford University, Stanford, CA, 2006.

Hubert-Ferrari, A., Armijo, R., King, G., Meyer, B., Barka, A., 2002. Morphology, displacement, and slip rates along the North Anatolian Fault, Turkey, *J. of Geoph. Res. (Solid Earth)*, **07(B10)**, 2235, doi:10.1029/2001JB000393, 2002.

Hubert-Ferrari, A., Barka, A., Jacques, E., Nalbant, S., Meyer, B., Armijo, R., Tapponnier, P. and King, G.C.P., 2000. Seismic hazard in the Sea of Marmara following the Izmit Earthquake, *Nature*, **404**, pp. 269–273, 2000.

Ishihara, K., Yoshimine, M. , 1992. Evaluation of settlements in sand deposits following liquefaction during earthquakes, *Soils and Foundations*, **32(1)**, pp. 173–188.

JICA-IMM, 2002. The study on a disaster prevention, Mitigation basic plan in Istanbul including microzonation in the Republic of Turkey (In Turkish), *Final Report*, Volume V, Japan International Cooperation Agency (JICA) & Istanbul Metropolitan Municipality (IMM), September 2002.

Jonsson, S., Adam., N., Bjornsson, H., 1998. Effects of subglacial geothermal activity observed by satellite radar Interferometry, *Geophysical Research Letters*, **25(7)**, pp. 1059-1062, April 1, 1998.

JSCE, 2000. The report of the 1999 Kocaeli Earthquake, Turkey, Kocaeli (Turkey) Earthquake, *Japan Society of Civil Engineers Report*, [http://www.jsce-int.org/Report/report/kocaeli_E.htm], Ed. Hamada, M., Tohma, J., Aydan, O, 2000.

Kalkan, Y., Alkan, R., M.O. Baykal, M. Yanalak, T. Erden ve H. Yıldırım, 2003. Monitoring of landslides by geodetic and geotechnical methods: An application at Ambarli Port area (in Turkish), *Proceedings of the 1th National Symposium of Engineering Surveys*, Conference, Location, 2003,

Kirkpatrick, S., Gelatt, C.D., Jr.,Vecchi, M.P., 1983. Optimization by Simulated Annealing, *Science*, **220**, pp. 671-680.

Knudsen, K.L., Sowers, J.M., Witter, R.C., Wentworth, C.M., Helley, E.J. , 2000. Description of mapping of quaternary deposits and liquefaction susceptibility, nine-county San Francisco Bay Region, California, *U.S. Geological Survey Open-File Report* No 00-444 (Part 3).

Laur, H., Bally, P., Meadows, P., Sanchez, J., Schaettler, B. , Lopinto, E., Esteban, D., 1998. Derivation of the backscattering coefficient sigma-nought in ESA ERS SAR PRI, http://earth.esa.int/esc_intro.htm, ESA Document No: ES-TN-RS-PM-HL09, ESA, Ispra, Italy September 1998.

Li, F., & Goldstein, R., 1990. Studies of Multibaseline Spaceborne Interferometric Synthetic Aperture Radars, *IEEE Trans. on Geosci. and Remote Sens., IGARSS '87 - International Geoscience and Remote Sensing Symposium*, Vol. 28, pp. 88-97, May 18-21 1987.

Louet, J., 2001. The Envisat Mission and System, *ESA Bulletin 106*, June 2001.

Lyons, S., & Sandwell, D., 2003. Fault creep along the southern San Andreas from interferometric synthetic aperture radar, permanent scatterers, and stacking, *Journal of Geophysical Research*, **108(B1)**, pp. 2047, doi:10.1029/ 2002JB001831.

Madsen, S.N., & Zebker, H.A., 1988. Chapter 6 Imaging Radar Interferometry, in *Manual of Remote Sensing, Principles and Applications of Radar Imaging, Third Edition*, Vol. 2, pp. 359-380, Ed. Henderson, F.M.L.A.J., Ed.-in-chief, Ryerson, R.A. Published in Co-operation with The American Society for Photogrammetry and Remote Sensing, John Wiley and Sons, Inc., 1988.

Massonnet, D., Rossi, M., Carmona, C., Adragna, F., Peltzer, G., Feigl, K. and Rabaute, T., 1993. The displacement field of the Landers earthquake mapped by radar interferometry, *Nature*, **364**, pp. 138–142, 1993.

Massonnet, D., & Rabaute, T., 1993. Radar interferometry: Limits and Potential, *IEEE Trans. Geosci. Remote Sens.*, **3(2)**, pp. 455-464.

Massonnet, D., Adragna, F., Rossi, M. , 1994. CNES general-purpose SAR correlator *IEEE Transactions on Geoscience and Remote Sensing*, **32(3)**, pp. 636 -643, May 1994.

Massonnet, D., & Feigl, K. L., 1995. Discrimination of geophysical phenomenon in satellite radar interferometry, *Geophys. Res. Lett.*, **22(12)**, pp. 1537-1540, June 15, 1995

Massonnet, D., Holzer, T., Vadon, H., 1997. Land subsidence caused by the East Mesa geothermal field, California, observed using SAR interferometry, *Geophysical Research Letters*, **24**, pp. 901–904, 1997.

Massonnet, D., & Feigl, K.L., 1998. Radar Interferometry and its Application to Changes in the Earth's Surface, *Rev. Geophys.*, **36 (4)**, pp. 441-500.

McClusky, S., Balassanian, S., Barka, A., Demir, C., Ergintav, S., Georgiev, I., Gurkan, O., Hamburger, M., Hurst, K., Kahle, H., Kastens, K., Kekelidze, G., King, R., Kotzev, V., Lenk, O., Mahmoud, S., Mishin, A., Nadariya, M., Ouzounis, A., Paradissis, D., Peter, Y., Prilepin, M., Reilinger, R., Sanli, I., Seeger, H., Tealeb, A., Toksoz, M.N., and Veis, G., 2000. Global Positioning System constraints on plate kinematics and dynamics in the eastern Mediterranean and Caucasus, *J. Geophys. Res.*, **105(3)**, pp. 5695– 5719

Miranda, N., Rosich, B., Santella, C., Grion, M., 2004. Review of the Impact of ERS-2 Piloting Modes on the SAR Doppler Stability, *Envisat & ERS Symposium*, ESA, Salzburg, Austria, 6-10 September 2004.

Mogi, K., 1958. Relations between the eruption of various volcanoes and the deformations of the ground surfaces around them, *Bull. of the Earthquake Research Institute*, **36**, pp. 99-134.

Mollamahmutoglu, M., Kayabali, K., Beyaz, T., Kolay, E., 2003. Liquefaction-related building damage in Adapazari during the Turkey earthquake of August 17, 1999, *Engineering Geology*, **67(2003)**, pp. 297–307.

MTA, 2003. Surface Rupture Associated with the August 17, 1999 Izmit Earthquake, *General Directorate of Mineral Research and Exploration Special Publications*, Ed. Emre, Ö., Awata, Y., Duman, T.Y., Ankara, 2003.

Nalbant, S., S., Hubert, A., and King, G., C., P, 1998. Stress coupling between earthquakes in northwest Turkey and the north Aegean Sea, *Journal of Geophysical Research*, **103(B10)**, pp. 24,469– 24,486.

Örmeci, C., 1972. Study of Mass Movements by photogrammetry (In Turkish), Istanbul Technical University, Faculty of Civil Engineering, Istanbul, Turkey, 1972.

Parker, R.L., McNutt, M.K., 1980. Statistics for the one-norm misfit measure, *Journal of Geophysical Research*, **85**.

Parsons, T., Toda, S., Stein, R.S., Barka, A., Dieterich, J.H., 2000. Heightened odds of large earthquakes near Istanbul: An interaction-based probability calculation, *Science*, **288**, pp. 661-665.

Peltzer, G., Hudnut, K.W., Feigl, K.L., 1994. Analysis of coseismic surface displacement gradients using radar interferometry: New insights into the Landers earthquake, *Journal of Geophysical Research*, **99**, pp. 21,971-21,981.

Perkins, J.B., 2001. The real dirt on liquefaction, A guide to the liquefaction hazard in future earthquakes affecting the San Francisco Bay Area *APAG Publication*, No: P01001EQK, Association of Bay Area Governments, February, 2001.

Poland, J.F., 1984. Mechanics of land subsidence due to fluid withdrawal, in *Guidebook to Studies of Land Subsidence Due to Groundwater Withdrawal*, pp. 37-54, Ed. Poland, J.F. UNESCO, Paris, 1984.

Press, W.H., Flannery, B.P., Teukolsky, S.A., Vetterling, W.T., , 1992. Numerical Recipes: The Art of Scientific Computing, Cambridge University Press, Cambridge.

Press, W.H., Flannery, B.P., Teukolsky, S.A. & Vetterling, W.T., 1992. Numerical Recipes: The Art of Scientific Computing,& 447 963 pp., C.U.P., Cambridge.

Price, E., & Sandwell, D. , 1998 Small-scale deformations associated with the 1992 Landers, California, earthquake mapped by synthetic aperture radar interferometry phase gradients. , *Journal of Geophysical Research*, **103(B11)**, pp. 27,001-27,016.

Rathje, E.M., Karatas, I., Wright, S.G., Bachhuber, J., 2004. Coastal Failures during the 1999 Kocaeli Earthquake in Turkey, *Soil Dynamics and Earthquake Engineering*, **24(9-10)**, pp. 699-712.

Reilinger, R., McClusky, S., Vernant, P., Lawrence, S., Ergintav, S., Cakmak, R., Ozener, H., Kadirov, F., Guliev, I., Stepanyan, R., Nadariya, M., Hahubia, G., Mahmoud, S., Sakr, K., ArRajehi, A., Paradissis, D., Prilepin, M., Guseva, T., Evren, E., Dmitrotsa, A., Filikov, S.,V., Gomez, F., Al-Ghazzi, R. and Karami, G., 2006. GPS constraints on continental deformation in the Africa-Arabia- Eurasia continental collision zone and implications for the dynamics of plate interactions, *J. Geophys Res.*, **111(, B5)**.

Reilinger, R.E., McClusky, S.C., Oral, M.B., King, R.W., Toksoz, M.N., Barka, A.A., Kinik, T., Lenk , O.,and Sanli, I. , 1997. Global Positioning System measurements of the present-day crustal movements in the Arabia-Africa- Eurasia plate collision zone, *J. Geophys. Res.*, **102**, pp. 9983– 9999.

Reilinger, R.E., Ergintav, S., Burgmann, R., McClusky, S., Lenk, O., Barka, A., Gurkan, O., Hearn, L., Feigl, K.L., Cakmak, R., Aktug, B., Ozener, H., Toksoz, M.N. , 2000. Coseismic and Postseismic Fault Slip for the 17 August 1999, M = 7.5, Izmit, Turkey Earthquake, *Science*, **289(5484)**, pp. 1519 - 1524, 1 September 2000.

Rodriguez, E., Morris, C.S., Belz, J.E., Chapin, E.C., Martin, J.M., Daffer, W., Hensley, S, 2005. An assessment of the SRTM topographic products, *Technical Report JPL D-31639*, Jet Propulsion Laboratory, Pasadena, California.

Rosen, P.A., Hensley, S., Joughin, I.R., Li, F.K., Madsen, S.N., Rodriguez, E., & Goldstein R.M., 2000. Synthetic aperture radar interferometry *Proceedings of the IEEE,*, **88(3)**, pp. 333-382.

Scharroo, R., & Visser, P., 1998. Precise Orbit Determination and gravity field improvement for ERS satellites, *Journal of Geophysical Research*, **103(C4)**, pp. 8113-8127, April 15, 1998.

Schmidt, D.A., Burgmann, R., 2003. Time-dependent land uplift and subsidence in the Santa Clara valley, California, from a large interferometric synthetic aperture radar data set, *Journal of Geophysical Research*, **108(B9)**, pp. 2426-2429.

Seed, H.B., Idriss, I. M., 1971. Simplified procedure for evaluating soil liquefaction potential, *ASCE Journal of the Soil Mechanics and Foundations Division*, **97(SM9)**, pp. 1249-1273.

Seed, H.B., 1979. Soil Liquefaction and Cyclic Mobility Evaluation for Level Ground During Earthquake, *ASCE Journal of Geotechnical Engineering Division*, **105(GT2)**, pp. 201-225.

Souyris, J.C., 2003. Focusing radar images from the geometric point of view, *Interferometric Course Notes*, CNES, Toulouse, France, 12 November 2003.

SPO, 1999. Economic and social effects of the earthquake, Probable budget needed, Precautions to be taken in short-medium and long term (in Turkish), State Planning Organization of Turkey, T.R. Prime Ministry State Planning Organization, 7 September 1999.

Stein, R.S., Barka, A. and Dieterich, J.H., 1997. Progressive failure on the North Anatolian Fault since 1939 by earthquake triggering, *Geophys. J. Int.*, **128**, pp. 594–604.

Tarayre, H., & Massonnet, D., 1996. Atmospheric propagation heterogeneities revealed by ERS-1 interferometry, *Geophysical Res. Lett.*, **23**, pp. 989-992.

Tezcan, S., S., Erdem, K., Bal, I., E., Ozdemir, Z., 2002. Seismic amplification at Avcilar, Istanbul, *Engineering Structures*, **24(5)**, pp. 661-667, 2002.

Tinsley, J.C., Youd, T.L., Perkins, D.M., Chen, A.T.F., 1985. Evaluating liquefaction potential, Evaluating earthquake hazards in the Los Angeles region; an earth-science perspective, *U. S. Geological Survey Series Professional Paper*, No 1360, Ed. Ziony, J.I., 1985.

Toksöz, M.N., Shakal, A.F., Micheal, A.J., 1979. Space time migration of earthquakes along the NAF zone and seismic gaps, *Pure Applied Geophysics*, **117**, pp. 1258-1270

TUIK, 2000. Census of Population, State Institute of Statistics Prime Ministry Republic of Turkey, Ankara.

Tüysüz, O., 2007. Personnel communication.

UKNERC, 2004. GMES Case Study 3: Stroke-on-Trent and Istanbul. Providing a ground motion service across Europe, *Press Release*, U. K. Nural Environment Research Council, 22 September 2004.

Usai, S., & Klees, R., , 1999. SAR Interferometry on a Very Long Time Scale: A Study of the Interferometric Characteristics of Man-Made Features, *IEEE Transactions on Geoscience and Remote Sensing*, **37(4)**, pp. 2118-2123, July 1999.

Usai, S., 2000. An analysis of the Interferometric Characteristics of Anthropogenic features, *IEEE Transactions on Geoscience and Remote Sensing*, **38(3)**, pp. 1491-1497, May 2000.

USGS, 2000. Implications for Earthquake Risk Reduction in the United States from the Kocaeli, Turkey, Earthquake of August 17, 1999, *U. S. Geological Survey Circular*, No 1193, 2000.

USNHI, 1998. Training course in Geotechnical and Foundation Engineering, Geotechnical Earthquake Engineering Reference Manual, *U. S. National Highway Institute Publication*, No FHWA HI-99-012, December, 1998.

Waltham, T., 2002. Sinking Cities, *Geology Today*, **18(3)**, pp. 95-100, May-June 2002.

Wegmuller, U., Strozzi, T., Werner, C., Wiesmann, A., Benecke, N., Spreckels, V., 2000. Monitoring of mining-induced surface deformation in the Ruhrgebiet (Germany) with SAR Interferometry, *IGARSS 2000*, IEEE International, Vol. 6, pp. 2771 –2773,

Witter, R.C., Knudsen, K.L., Sowers, J.M., Wentworth, C.M., Koehler, R.D., Randolph, C.E., Brooks, S.K., Gans, K.D., 2006. Maps of quaternary deposits and liquefaction susceptibility in the central San Francisco Bay region, California, *U. S. Geological Survey Open-File Report*, No 2006-1037.

Wright, T.J., 2000. Crustal Deformation in Turkey from Synthetic Aperture Radar Interferometry, *D. Phil*, Faculty of Physical Sciences, University of Oxford, Oxford, 2000.

Wright, T.J., Fielding, E.J., Parsons, B.E., 2001. Triggered slip: observations of the 17 August 1999 Izmit (Turkey) earthquake using radar interferometry, *Geophys. Res. Lett.*, **28(6)**, pp. 1079-1082.

Youd, L., 1999. Updating Assessment Procedures and Developing a Screening Guide for Liquefaction, *Research Progress and Accomplishments 1997-1999*, Multidisciplinary Center for Earthquake Engineering Research University at Buffalo, State University of New York, July 1999.

Youd, T.L., 1973. Liquefaction, flow, and associated ground failure, *U. S. Geological Survey Circular*, No 688.

Youd, T.L., and Perkins, D.M., 1978. Mapping liquefaction-induced ground failure potential, *Proceedings of the American Society of Civil Engineers, Journal of the Geotechnical Engineering Division*, **104(GT4)**, pp. 433-446.

Youd, T.L., 1984. Liquefaction and Associated Ground Failure, *Proceedings of Geologic and Hydrologic Hazards Training Program*, Conference, Location, March 5-30, USGS Open-File Report 84-760.

Zebker, H., & Goldstein, R., 1986. Topographic mapping from interferometric SAR observations, *J. Geophys. Res.*, **91**, pp. 4993–5001.

Zebker, H.A., & Villasenor, J. , 1992. Decorrelation in Interferometric Radar Echoes, *IEEE Trans. on Geosci. and Remote Sens.*, **30(5)**, pp. 950-959.

Zebker, H.A., Rosen, P.A., Goldstein, R.M., Gabriel, A., Werner, C.L. , 1994. On the derivation of coseismic displacement fields using differential radar interferometry: The Landers Earthquake, *J. Geophys. Res.*, **99**, pp. 19,617–19,634.

APPENDIX A

The list of T336 / F2783 interferograms with an altitude of ambiguity (H_{amb}) higher than 100 m is given in the following. The columns represent the dates of the Master and the Slave (Date1 and Date2), the orbit numbers of the Master and the Slave (Orb1 and Orb2), the altitude of ambiguity in meters (H_{amb}), the time difference in days between the acquisitions (Dtday), the decimal years (Dyear1 and Dyear2), the Doppler difference as PRF (Ddop), respectively. At the last column, the codes are used for the following explanations.

Time span according to the 1999 Izmit Earthquake:
I : Interseismic
Q : Co-seismic
P : Post-seismic

Contributions:
t : Atmospheric fringes
r : Orbital fringes
x : No interferogram

Quality:
A : Good
B : Can be useful
C : Useless
a : Accept for temporal adjustment

Table A.1 : T336 / F2783 interferograms

Date1	Date2	Orb1	Orb2	H_{amb} (m)	Dtday (days)	Dyear1	Dyear2	Ddop (PRF)	Remarks
1992APR20	1995OCT25	3988	22368	-11880	1283	1992.301	1995.814	0.050	I A
1992APR20	1995OCT26	3988	2695	-105	1284	1992.301	1995.816	0.182	I B
1992MAY25	2002JAN17	4489	35260	742	3524	1992.396	2002.044	0.349	Qr B
1992MAY25	2002JUL11	4489	37765	-348	3699	1992.396	2002.523	0.553	Q C
1992NOV16	1993AUG23	6994	11002	101	280	1992.874	1993.641	0.012	It B a
1992NOV16	1993JUN14	6994	10000	-217	210	1992.874	1993.449	-0.012	It A a
1992NOV16	1995JUL12	6994	20865	-2446	968	1992.874	1995.526	-0.019	I A a
1992NOV16	1995JUL13	6994	1192	-216	969	1992.874	1995.529	0.145	It A a
1992NOV16	1996SEP05	6994	7204	-305	1389	1992.874	1996.678	0.143	I A a
1992NOV16	2000DEC28	6994	29749	-198	2964	1992.874	2000.989	0.239	Q C
1992NOV16	2001DEC13	6994	34759	82	3314	1992.874	2001.948	-0.034	Q C
1993JAN25	1995SEP21	7996	2194	-128	969	1993.066	1995.721	0.257	Ir A
1993JAN25	1997MAY08	7996	10711	-2252	1564	1993.066	1997.348	0.161	I A
1993JAN25	1998DEC24	7996	19228	436	2159	1993.066	1998.978	0.140	I B
1993JAN25	1998OCT15	7996	18226	-105	2089	1993.066	1998.786	0.162	I B
1993JAN25	1999AUG25	7996	42408	1306	2403	1993.066	1999.647	0.014	Q A
1993JAN25	1999NOV04	7996	23737	-103	2474	1993.066	1999.841	0.213	Q B
1993JAN25	2000JUL06	7996	27244	311	2719	1993.066	2000.511	0.536	Q C
1993JAN25	2000SEP14	7996	28246	182	2789	1993.066	2000.702	0.303	Q C
1993APR05	1993NOV01	8998	12004	100	210	1993.257	1993.833	0.016	Irt B
1993APR05	1999SEP29	8998	42909	-512	2368	1993.257	1999.743	-0.001	Qr A
1993APR05	2000APR27	8998	26242	-258	2579	1993.257	2000.320	0.322	Q C
1993JUN14	1995JUL12	10000	20865	238	758	1993.449	1995.526	-0.007	It A a
1993JUN14	1995JUL13	10000	1192	-44724	759	1993.449	1995.529	0.158	It A a
1993JUN14	1995SEP20	10000	21867	-201	828	1993.449	1995.718	0.013	It A a
1993JUN14	1996SEP05	10000	7204	750	1179	1993.449	1996.678	0.156	It A a
1993JUN14	2000DEC28	10000	29749	-2326	2754	1993.449	2000.989	0.251	Q C
1993AUG23	2001DEC13	11002	34759	418	3034	1993.641	2001.948	-0.046	Q C
1993NOV01	2002OCT24	12004	39268	319	3279	1993.833	2002.811	0.272	Q C
1995MAY03	1999AUG26	19863	22735	-1323	1576	1995.334	1999.649	0.148	Q B
1995MAY03	2001MAY17	19863	31753	-227	2206	1995.334	2001.373	0.335	Q C
1995MAY03	2002JUL11	19863	37765	116	2626	1995.334	2002.523	0.544	Q C
1995JUN07	1995SEP21	20364	2194	121	106	1995.430	1995.721	0.246	It A a
1995JUN07	1996MAY22	20364	25374	-186	350	1995.430	1996.388	0.015	It A a
1995JUN07	1998OCT15	20364	18226	153	1226	1995.430	1998.786	0.151	I B a
1995JUN07	1999NOV04	20364	23737	157	1611	1995.430	1999.841	0.202	Q B
1995JUN07	2000JUN01	20364	26743	163	1821	1995.430	2000.415	0.444	Q C
1995JUL12	1995JUL13	20865	1192	-236	1	1995.526	1995.529	0.164	It C
1995JUL12	1995SEP20	20865	21867	-109	70	1995.526	1995.718	0.019	It B a
1995JUL12	1996SEP05	20865	7204	-348	421	1995.526	1996.678	0.162	I B a
1995JUL12	2000DEC28	20865	29749	-216	1996	1995.526	2000.989	0.258	Q B
1995JUL13	1995SEP20	1192	21867	-202	69	1995.529	1995.718	-0.145	It B a
1995JUL13	1996SEP05	1192	7204	737	420	1995.529	1996.678	-0.002	It B a
1995JUL13	2000DEC28	1192	29749	-2543	1995	1995.529	2000.989	0.093	Q B
1995AUG16	1995AUG17	21366	1693	130	1	1995.622	1995.625	0.177	Itr C
1995AUG16	1996AUG01	21366	6703	156	351	1995.622	1996.582	0.206	It B
1995AUG16	1996JAN03	21366	23370	-119	140	1995.622	1996.005	0.018	It B
1995AUG16	1999NOV03	21366	43410	-726	1540	1995.622	1999.838	-0.001	Q A
1995AUG16	2000OCT19	21366	28747	-177	1891	1995.622	2000.798	0.242	Q B
1995AUG17	1996AUG01	1693	6703	-766	350	1995.625	1996.582	0.030	It B

1995AUG17	1996JAN04	1693	3697	379	140	1995.625	1996.008	-0.011	It	B	a
1995AUG17	1996MAY22	1693	25374	117	279	1995.625	1996.388	-0.147	It	B	a
1995AUG17	1999NOV03	1693	43410	-110	1539	1995.625	1999.838	-0.178	Qr	B	
1995SEP20	1996SEP05	21867	7204	159	351	1995.718	1996.678	0.143	It	B	a
1995SEP20	1998DEC24	21867	19228	-114	1191	1995.718	1998.978	0.115	I	B	a
1995SEP20	2000DEC28	21867	29749	220	1926	1995.718	2000.989	0.238	Q	B	
1995SEP20	2000JUL06	21867	27244	-128	1751	1995.718	2000.511	0.511	Q	C	
1995SEP20	2000SEP14	21867	28246	-180	1821	1995.718	2000.702	0.278	Q	B	
1995SEP21	1997MAY08	2194	10711	135	595	1995.721	1997.348	0.103	I	B	a
1995SEP21	1998OCT15	2194	18226	-582	1120	1995.721	1998.786	0.095	It	A	a
1995SEP21	1999AUG25	2194	42408	117	1434	1995.721	1999.647	0.000	I	C	
1995SEP21	1999NOV04	2194	23737	-534	1505	1995.721	1999.841	0.044	Q	A	
1995SEP21	2000JUN01	2194	26743	-474	1715	1995.721	2000.415	-0.198	Q	C	
1995OCT25	1995OCT26	22368	2695	-106	1	1995.814	1995.816	0.132	Itr	C	
1995OCT26	2000NOV23	2695	29248	-203	1855	1995.816	2000.893	0.049	Q	A	
1996JAN03	1996MAR14	23370	4699	-136	71	1996.005	1996.199	0.164	Itr	C	
1996JAN03	1999NOV03	23370	43410	143	1400	1996.005	1999.838	-0.018	Qr	A	
1996JAN03	2000OCT19	23370	28747	362	1751	1996.005	2000.798	0.225	Q	B	
1996JAN04	1996AUG01	3697	6703	-254	210	1996.008	1996.582	0.041	It	A	a
1996JAN04	1996MAY22	3697	25374	170	139	1996.008	1996.388	-0.136	It	A	a
1996MAY22	1996AUG01	25374	6703	-102	71	1996.388	1996.582	0.177	It	B	
1996AUG01	1999NOV03	6703	43410	-128	1189	1996.582	1999.838	-0.207	Qr	B	
1996SEP05	2000DEC28	7204	29749	-567	1575	1996.678	2000.989	0.095	Q	A	
1997MAY08	1998DEC24	10711	19228	376	595	1997.348	1998.978	-0.015	I	C	
1997MAY08	1998OCT15	10711	18226	-107	525	1997.348	1998.786	0.008	It	A	a
1997MAY08	1999AUG25	10711	42408	850	839	1997.348	1999.647	-0.141	Q	A	
1997MAY08	1999NOV04	10711	23737	-108	910	1997.348	1999.841	0.059	Q	A	
1997MAY08	2000JUL06	10711	27244	261	1155	1997.348	2000.511	0.384	Qr	A	
1997MAY08	2000SEP14	10711	28246	177	1225	1997.348	2000.702	0.148	Qt	A	
1998OCT15	1999AUG25	18226	42408	97	314	1998.786	1999.647	-0.148	Q	A	
1998OCT15	1999NOV04	18226	23737	-6346	385	1998.786	1999.841	0.051	Q	A	
1998OCT15	2000JUN01	18226	26743	-2545	595	1998.786	2000.415	0.293	Q	B	
1998DEC24	1999AUG25	19228	42408	-642	244	1998.978	1999.647	-0.126	C	A	
1998DEC24	2000JUL06	19228	27244	1082	560	1998.978	2000.511	0.399	Q	B	
1998DEC24	2000SEP14	19228	28246	311	630	1998.978	2000.702	0.163	Q	B	
1999AUG25	1999NOV04	42408	23737	-96	71	1999.647	1999.841	0.200	Pt	B	
1999AUG25	2000JUL06	42408	27244	405	316	1999.647	2000.511	0.525	P	C	
1999AUG25	2000SEP14	42408	28246	209	386	1999.647	2000.702	0.289	Pt	B	
1999AUG26	2001MAY17	22735	31753	-274	630	1999.649	2001.373	0.188	P	A	
1999AUG26	2002JUL11	22735	37765	106	1050	1999.649	2002.523	0.397	P	C	
1999SEP29	2000APR27	42909	26242	-494	211	1999.743	2000.320	0.323	P	B	
1999SEP30	2002OCT24	23236	39268	-131	1120	1999.745	2002.811	0.138	P	C	
1999NOV03	2000OCT19	43410	28747	-234	351	1999.838	2000.798	0.243	P	X	
1999NOV04	2000JUN01	23737	26743	-4249	210	1999.841	2000.415	0.242	Pt	A	
2000JUL06	2000SEP14	27244	28246	436	70	2000.511	2000.702	-0.233	Pt	A	
2000SEP14	2000DEC28	28246	29749	99	105	2000.702	2000.989	-0.040	Pt	A	
2002JAN17	2002JUL11	35260	37765	-241	175	2002.044	2002.523	0.199	Ptr	A	

APPENDIX B

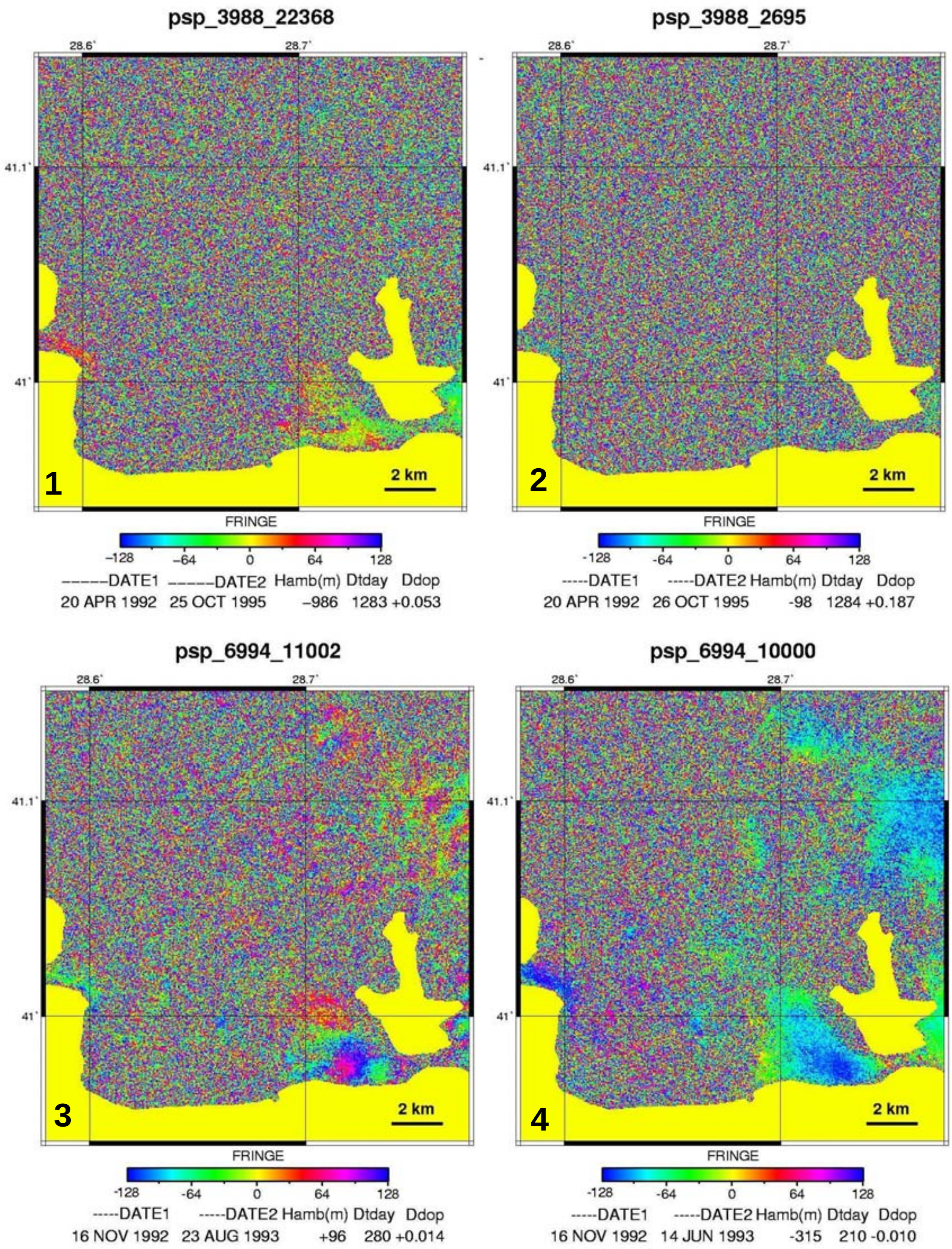

Figure B.1 : Interferograms 1-4

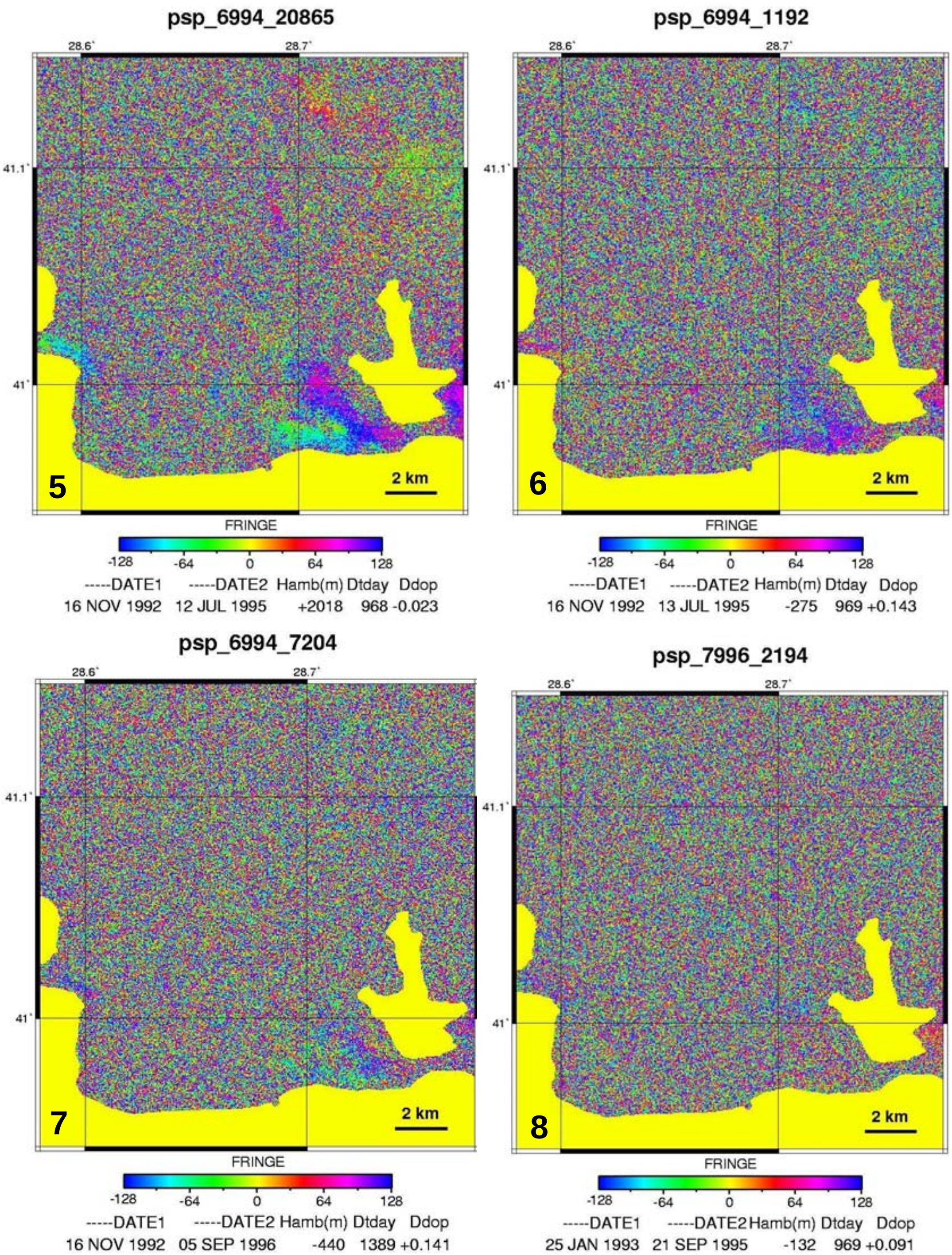

Figure B.2 : Interferograms 5-8

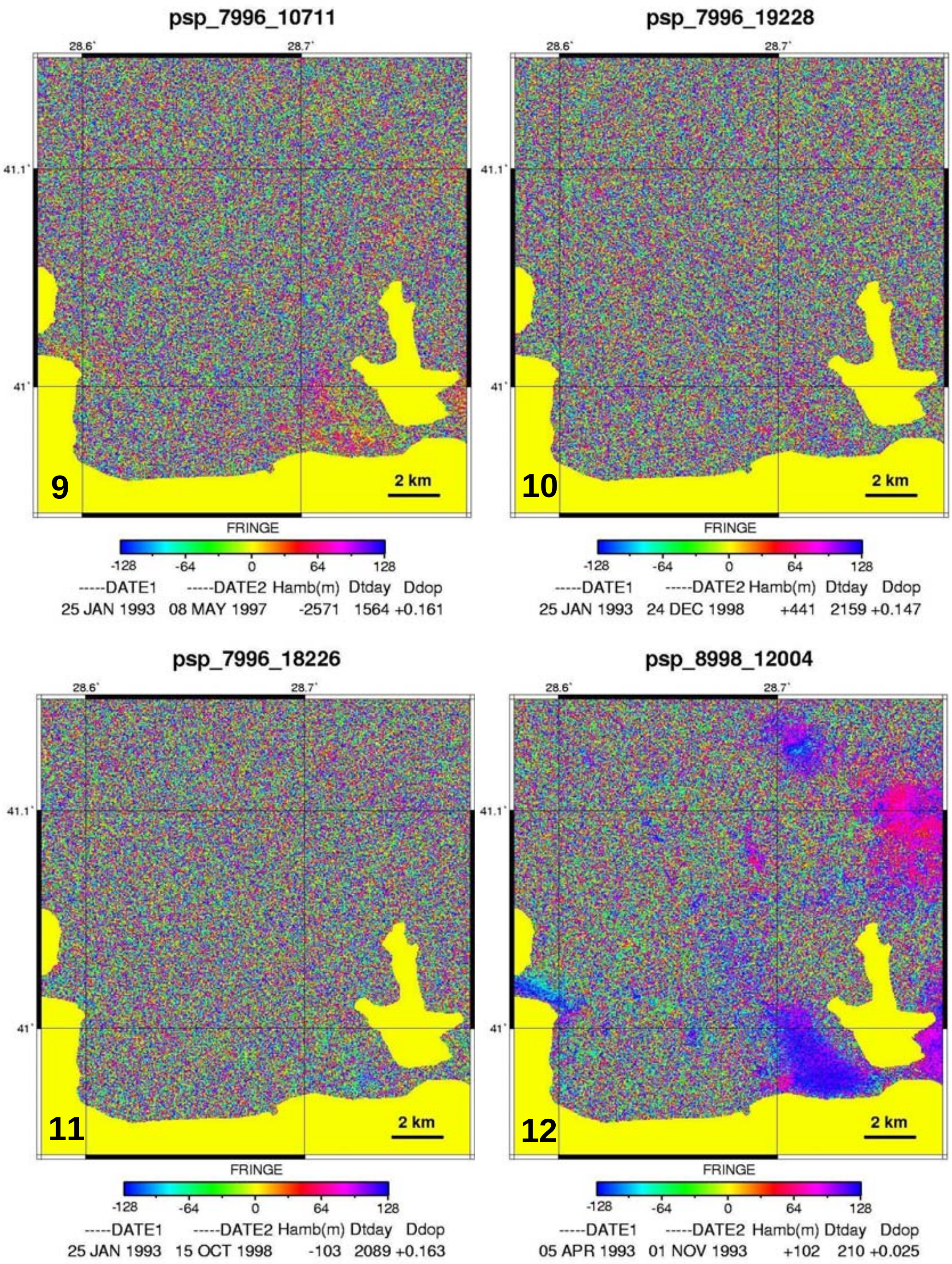

Figure B.3 : Interferograms 9-12

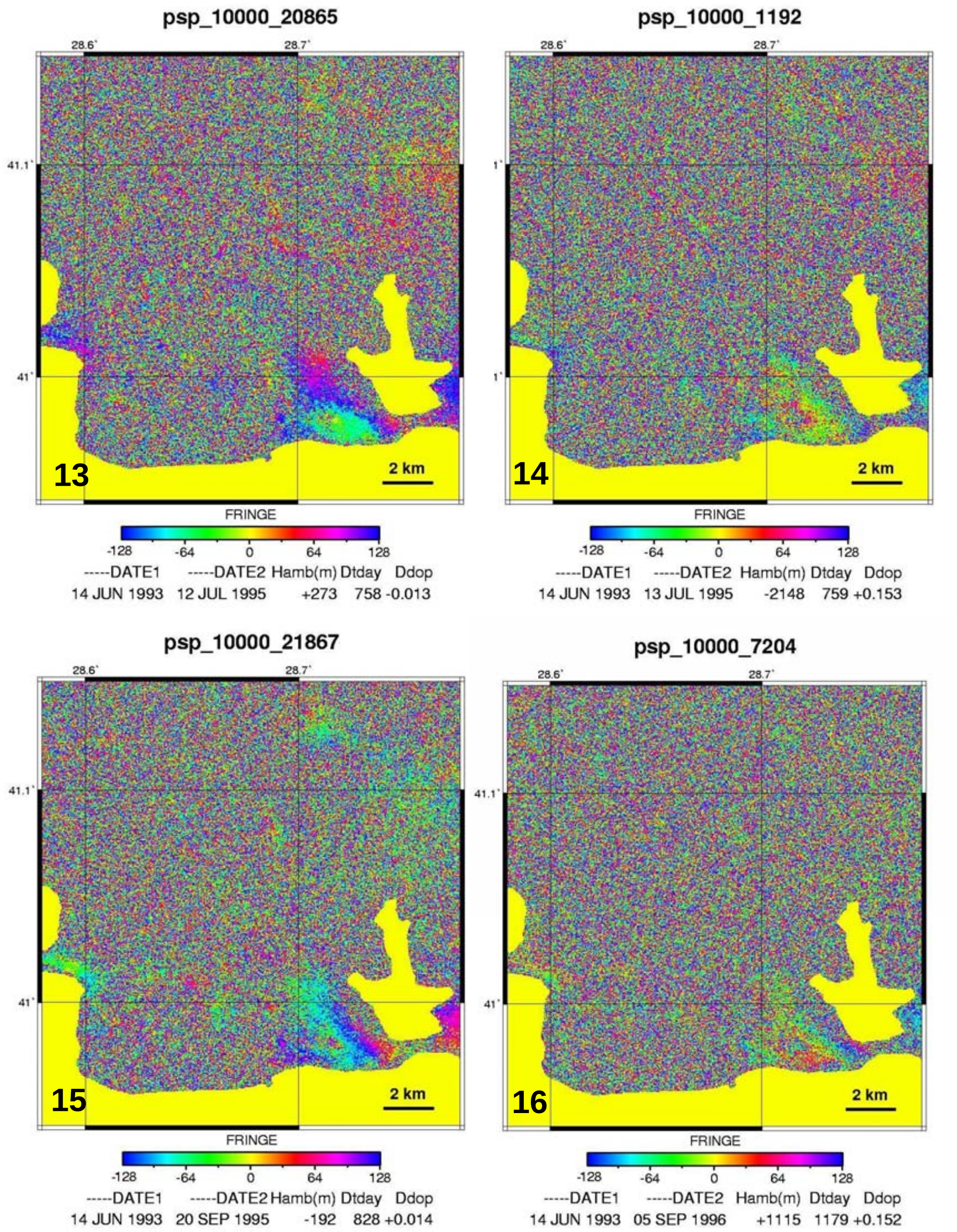

Figure B.4 : Interferograms 13-16

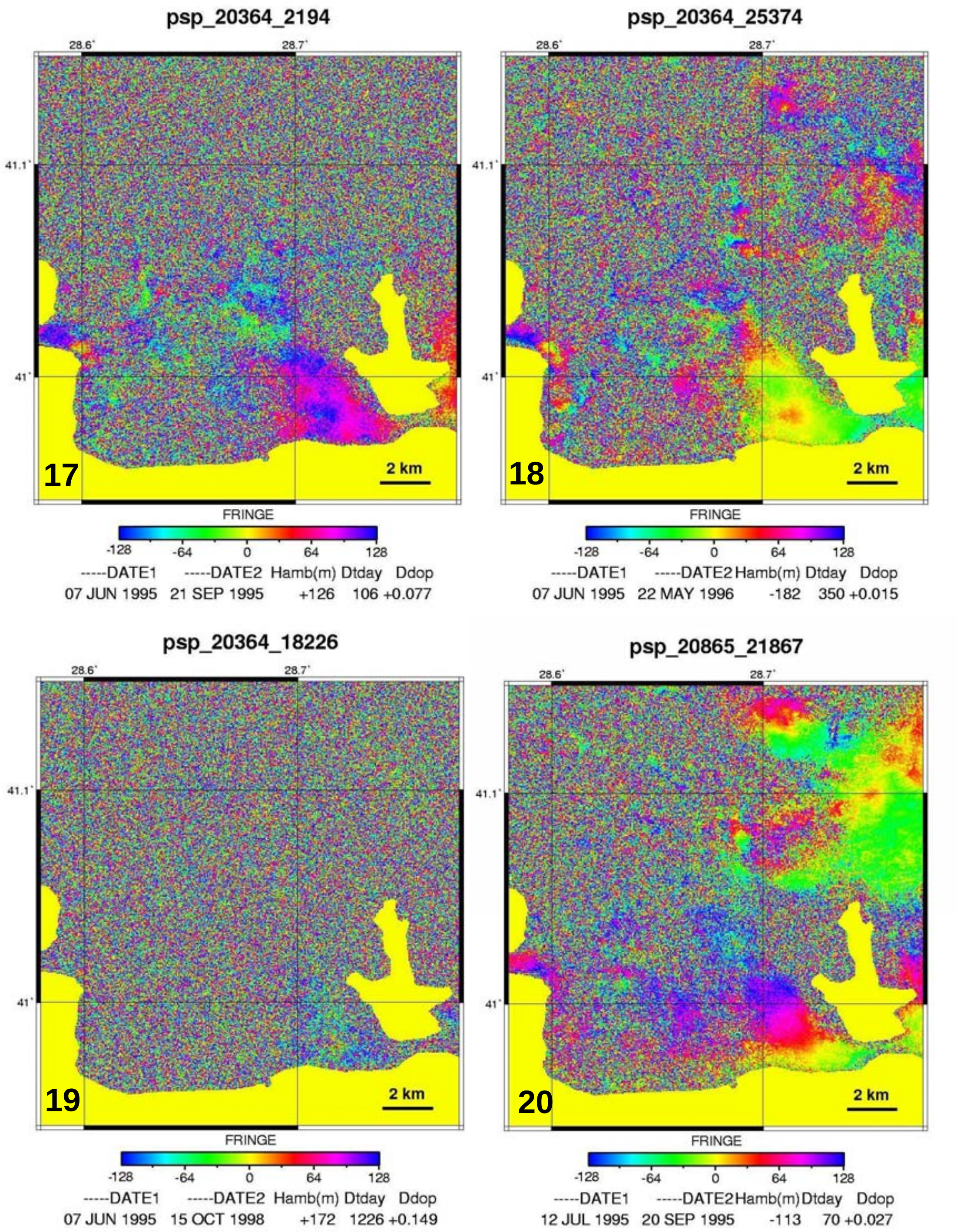

Figure B.5 : Interferograms 17-20

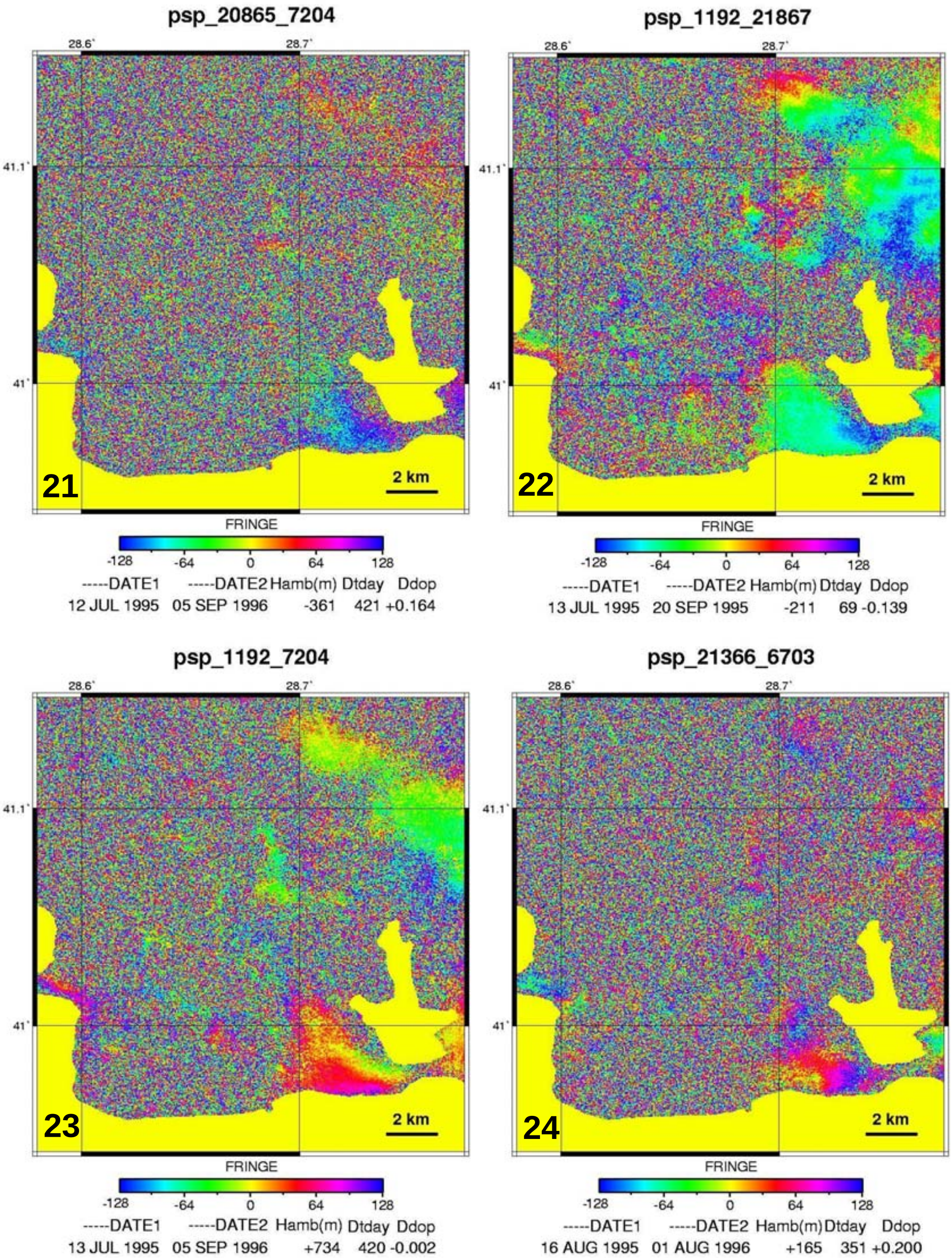

Figure B.6 : Interferograms 21-24

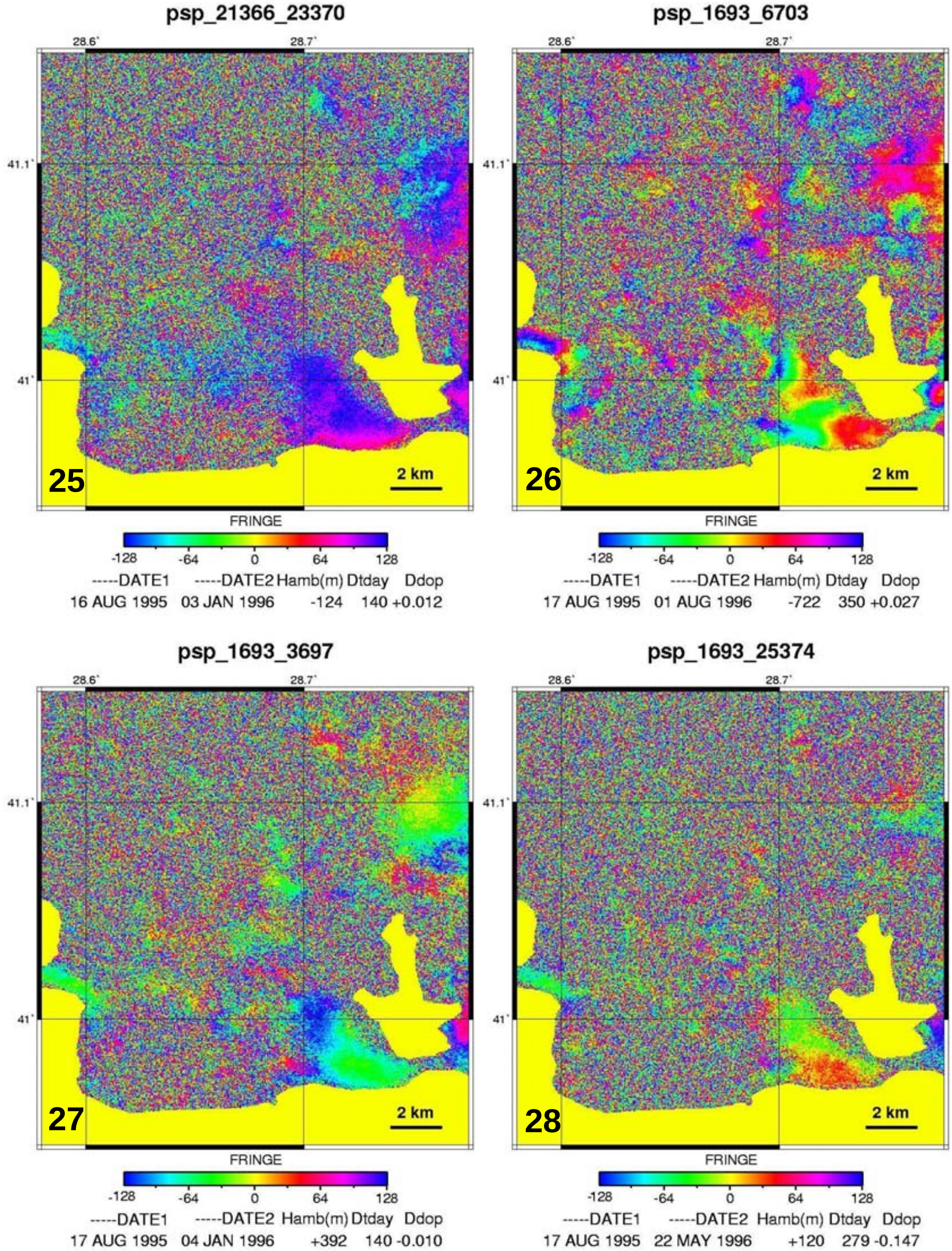

Figure B.7 : Interferograms 25-28

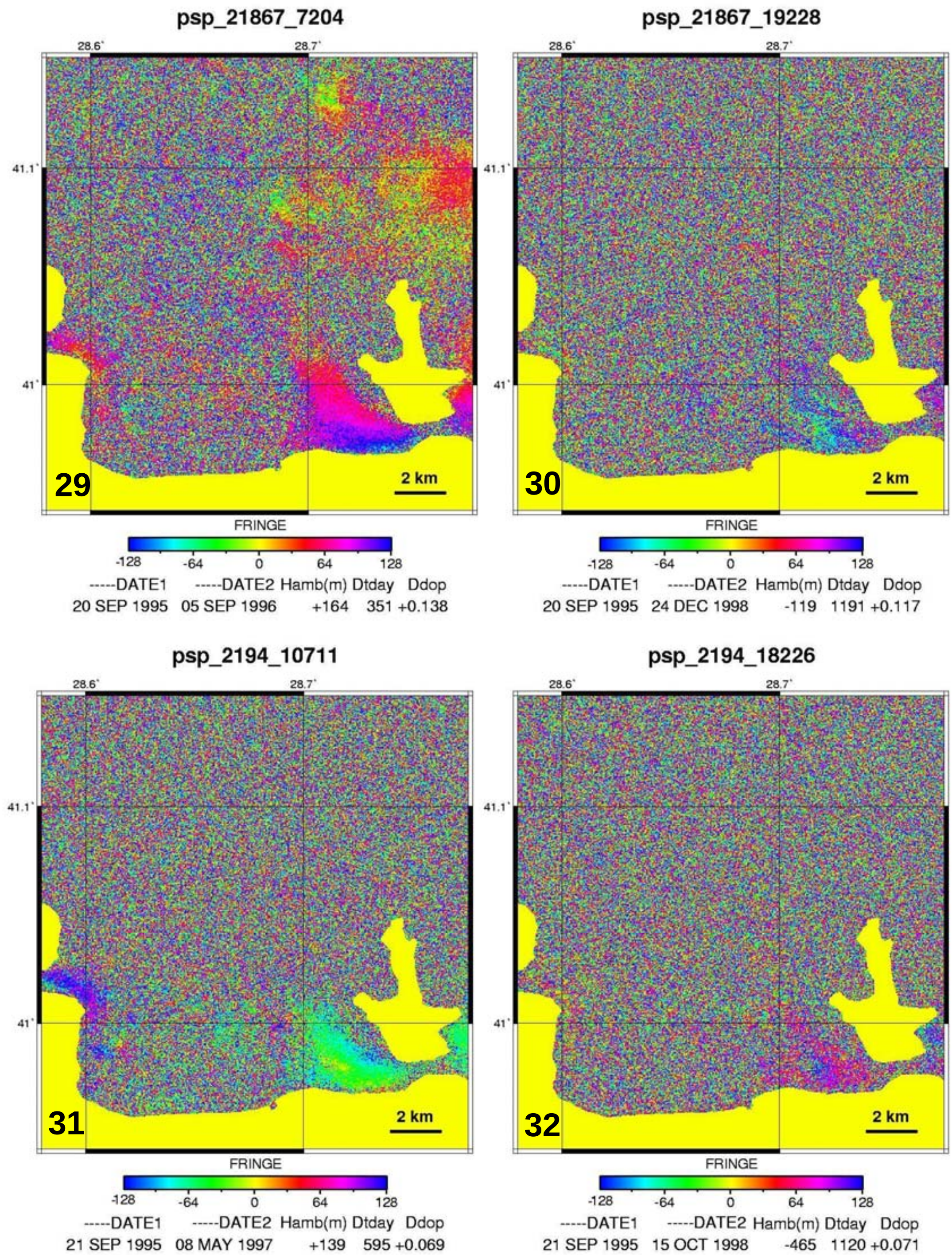

Figure B.8 : Interferograms 29-32

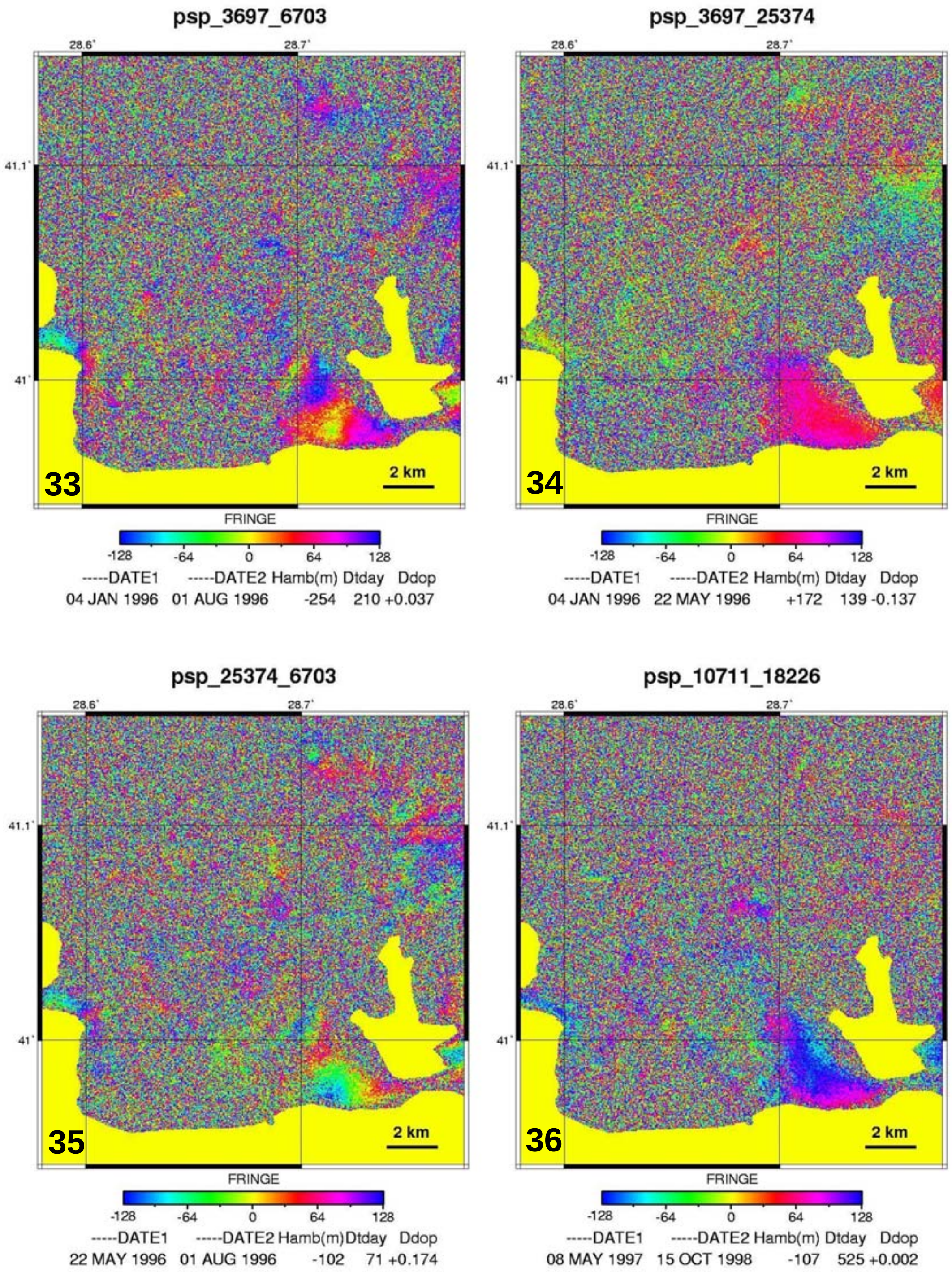

Figure B.9 : Interferograms 33-36

CURRICULUM VITAE

Samuray Elitaş Akarvardar was born in Istanbul, Turkey in 1972. She obtained her engineering diploma and M.Sc. degree from Geodesy and Photogrammetry Engineering Department of İstanbul Technical University (İTÜ) in 1994 and 1997, respectively. She had her Ph.D. sufficiency from Remote Sensing Division of İTÜ in 2000. Five years later, she started a joint Ph.D. thesis between Istanbul Technical University (İstanbul, Turkey) and Paul Sabatier University (Toulouse, France).

She has worked as a researcher in the Geographic Information Systems and Remote Sensing Group of TUBITAK MRC (The Scientific and Technological Researc Counsil of Turkey, Marmara Research Center) for eight years between 1995 and 2003. During this time she has been a researcher at two different institutes of TUBITAK MRC; the Information Technologies Institute and the Earth and Marine Sciences Institute.

She has been working at the Planetary and Terrestrial Dynamics Laboratory of Midi–Pyrénées Observatory (Toulouse, France) as an engineer since 2005.